UNIVERSITY OF OKLAHOMA

GRADUATE COLLEGE

PASSIVE RF CIRCUITS FOR SIMULTANEOUS TRANSMIT AND RECEIVE AND IMPACT ANALYSIS OF RECONFIGURABLE WIDEBAND RF ELECTRONICS ON COMMUNICATIONS SYSTEM OPERATIONS

A THESIS

SUBMITTED TO THE GRADUATE FACULTY

in partial fulfillment of the requirements for the

Degree of

MASTER OF SCIENCE

By

C. JUSTIN R. SMITH
Norman, Oklahoma
2016

PASSIVE RF CIRCUITS FOR SIMULTANEOUS TRANSMIT AND RECEIVE AND IMPACT ANALYSIS OF RECONFIGURABLE WIDEBAND RF ELECTRONICS ON COMMUNICATIONS SYSTEM OPERATIONS

A THESIS APPROVED FOR THE
SCHOOL OF ELECTRICAL AND COMPUTER ENGINEERING

BY

Dr. Hjalti Sigmarsson, Chair

Dr. Caleb Fulton

Dr. Jessica Ruyle

This work is dedicated to my daughter Gabriele, without her my life would be incomplete, and to the memory of my father, David.

Acknowledgments

I would like to express my gratitude to the members of my committee for their participation in this thesis and their contribution to my academic success. I am especially grateful to Dr. Hjalti Sigmarsson and Dr. Caleb Fulton for their mentorship and their continued encouragement throughout my academic studies.

I would also like to thank Zachary Potts for his assistance in fabricating some of the devices used in this work and to Adam Horton for his assistance in printing the lithographic masks used.

Finally, I would like to thank my wife Rachael for her patience and her steadfast support, without her this work would not have been possible.

Table of Contents

List of Tables

List of Figures

Abstract

Consumer based wireless systems currently operate with a split spectrum approach. However, in order to accommodate the increased demand for high datarate services within fixed spectrum allocations a new architecture will be required. The ability to simultaneously transmit and receive data within the full spectrum allocation can alleviate this problem. Simultaneous transmission and reception within current spectrum limits could effectively double data rates. However, physical limitations on radio frequency circuits including reflections and mutual coupling currently limit the capability of systems to operate in this mode. Therefore, radio frequency circuits that cancel this self-interference must be introduced.

This thesis describes the development of a self-interference cancellation circuit for simultaneous transmit and receive. The design operates by combining an out of phase signal of equal magnitude with the original self-interference signal. Design methodology for the required radio frequency circuitry, including antenna elements, directional couplers, and hairpin resonators is provided. A characterization method for determining the antenna mutual coupling and phase characteristics is implemented in commercial computer aided design software. Both a hairpin resonator and a delay line are used to match the phase and magnitude characteristics of the antenna mutual coupling. Directional couplers are designed to provide the required anti-phasing of the signal and couple the required power level from the transmit path, through the phasing element, to the receive path. The devices are fabricated on high frequency printed circuit board materials and measured. The theory of operation for a T-junction exponential power divider used in an early version of the circuit is also presented. Measured results of the self-interference cancellation circuit agree well with simulation.

Future RF systems are being designed with a desire for both simultaneous trans-

mit and receive capability and wideband operation. However, due to the nature of wideband devices, they are susceptible to out-of-band interference degrading system-level performance. With this in mind, a system level analysis of a wideband low noise amplifier with both adaptive and controllable biasing current is performed. Based on a quadrature phase shift keyed communications system, simulation and measurements fundamental to the operation of such wideband devices are conducted. This analysis shows the dependence of in-band performance on power received from out-of-band interfering signals. It is shown that the out-of-band noise sources contribute to increased error vector magnitude in the receiver due to gain compression.

1 Introduction

In the current era of widespread adoption and use of wireless technology, spectrum management and efficient spectrum utilization are critical challenges that must be addressed. With the increasing consumptive demand for services such as data, audio, and video over wireless, within essentially fixed communications channels, new techniques for enabling high-bandwidth data transmission must be adopted. Due to limitations caused in part by self-interference, the current GSM spectrum is split into two separate channels for uplink and downlink. This split spectrum approach effectively limits the bandwidth available to users by reducing the available GSM spectrum by 64%, when the guard band between uplink and downlink is included. However, if the full bandwidth of the spectrum could be utilized for both uplink and downlink current data rates could be approximately doubled [1]. A similar self-interference problem plagues large phased array antennas. Due to transmit power coupling back into adjacent antenna elements, large arrays must operate by dividing time between transmitting and receiving [2]. This "silent" time is possibly more inefficient than the split spectrum approach taken by the wireless industry.

In addition to the bandwidth and time limitations imposed by self-interference, new technologies and platforms are being designed to have wideband spectral responses. However, this subjects them to outside interference and noise, in addition to the original self-interference. Therefore, methods must be developed to suppress the inherent self-interference and the effects of outside interference must be studied for wideband devices. The goal of this thesis is to address both of these topics.

1.1 Simultaneous Transmit and Receive

The idea that a radio frequency (RF) system should be capable of both transmitting and receiving analog or digital information simultaneously is a straightforward

concept. From the perspective of human communication, however, it is analogous to speaking, listening, and most importantly, comprehending information at the same time. Typically in human communications an entirely different process takes place. Participants automatically perform a form of time division multiplexing (TDM), where while one person is speaking, all other participants listen. This communication protocol limits the "interference" that would occur if the other participants were also speaking in the same "time slot". In wireless communications an analogous TDM architecture is often also used [3].

In systems where prior information is not required for future transmissions, simultaneous transmit and receive (STAR) architectures may be utilized. An example of one such architecture is frequency division multiplexing (FDM) [3]. In FDM, signals are separated by frequency, and different frequency bands are allocated for the transmission of data (uplink channel) and the reception of data (downlink channel). A well known example of such a system is the GSM cellular telephone system [4]. Fig. 1.1 displays the frequency bands used for uplink and downlink on the GSM-850 band used in North America and Canada [5]. Such systems are typically realized through both the use of antenna diversity at the transmitter [6] and through the use of RF diplexer circuits [7]. The main disadvantage of this type of system is that it utilizes the RF spectrum inefficiently, utilizing approximately twice the necessary frequency domain space compared to a perfect STAR system [1].

An important system that neither requires information from previous transmissions and would benefit largely from STAR is radar. Current pulse-doppler (PD) radars operate using a TDM architecture [2]. The primary reason for operating as a TDM system is self-interference, or leakage of energy from the system transmit path to the system receive path. By not transmitting during specified time windows, or by using a switching transmitter, the receiver can be made more sensitive to low-power

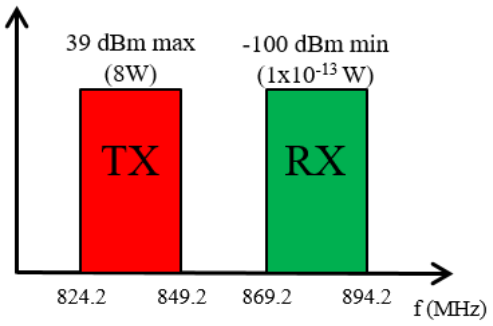

Figure 1.1: Example of FDM in GSM cellular uplink and downlink channels.

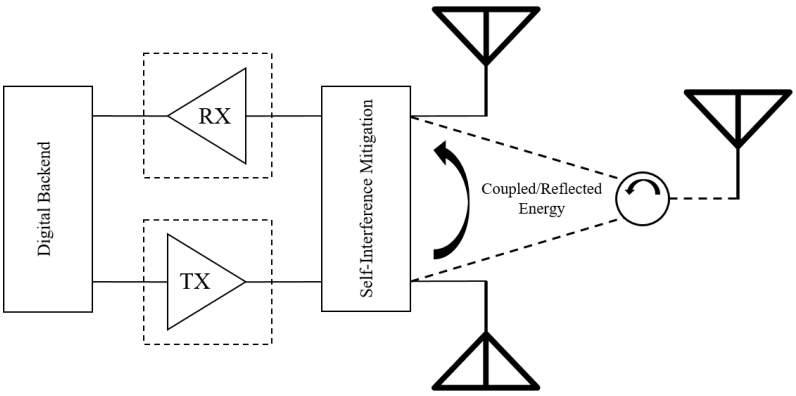

Figure 1.2: Basic STAR block diagram.

receive signals [2].

Providing a high degree of isolation between the transmit and receive sections through RF circuit design is quite challenging. This is due to both reflected energy from imperfect loads and from energy coupling between closely spaced transmit and receive antennas. Therefore, in order to achieve a transceiver capable of STAR this undesirable returned energy must be addressed. As shown in Fig. 1.2, implementing STAR requires additional self-interference mitigation to occur between the transmitter and receiver in the analog domain.

	Different Frequency	Same Frequency
TX/RX Different Antenna	Case 1	Case 2
TX/RX Same Antenna	Case 3	Case 4

Figure 1.3: The four main STAR frequency and antenna configurations.

1.1.1 STAR Considerations

There are two system level design constraints that have the greatest impact on the type of techniques and technologies required for implementing STAR [8]. The first of these constraints is whether the design requires transmission and reception on a single frequency or if multiple frequencies can be utilized. The second constraint, largely be dictated by other system requirements, is whether the transmit and receive channels will be on the same, or different antennas. These four cases are shown in Fig. 1.3. Each case presents its own specific design challenges, however in each case the primary design requirement is to provide sufficient isolation between the transmit (Tx) and receive (Rx) paths. Tx-Rx isolation in some cases, such as communication systems, must be sufficiently large so that the interfering signal is attenuated to a level below the noise-floor of the receiver [9].

In order to achieve sufficient self-interference mitigation three design areas must be addressed [10]. In general, the total isolation will need to be on the order of 100 dB [1]. Unfortunately, this level of self-interference mitigation cannot be obtained through a single approach. Since the interfering signal originates from reflections or energy coupled back into the receive path from the antenna this is one design area that has been studied [8], [9], [11]–[17]. Another area where work has occurred is in circuit level analog isolation. For single antenna systems, ferrite

circulators have been used [18], which provide isolation on the order of 25–40 dB. Recently, active, quasi-active, and photonic "circulators" have been shown with similar performance [19]–[22].

In recent work on multi-antenna systems it has been shown that a high degree of isolation can be achieved between adjacent elements through the use of spatial filters and spatial phase cancellation [14], [16], [17]. The achievable cancellation through the use of spatial filters called baffles presented in [14] is 50 dB over 420 kHz of bandwidth. In [16] a 5-element monopole antenna array was designed to provide spatial phase cancellation. The two outer elements of the array are used as Tx elements, and the three inner elements are used as Rx elements. A destructive interference zone is created around three central elements through anti-phasing of the Tx elements, achieving 40–55 dB of additional Tx-Rx isolation over 5 MHz of bandwidth. The antenna presented in [17] uses a similar methodology, achieving Tx-Rx isolation of 55 dB over 100 MHz of bandwidth. Finally, digital cancellation schemes have been demonstrated to provide additional self-interference mitigation of up to 25 dB [10].

1.1.2 STAR Circuit Configurations

The importance of both antenna design and back-end digital self-interference mitigation techniques cannot be neglected in a complete STAR system. However, the main focus of this work will be on analog circuit configurations. In the realm of continuous wave (CW) radar, several methods have been presented that utilize feedback to achieve self-interference suppression in the receive path [23]–[30]. The above methodologies have been applied to single antenna systems. The common feature of these approaches is that an active electronics layer is used to modify the amplitude and phase of the self-interference signal before being recombined out of phase in the

receive path. In general, all approaches for STAR using phase cancellation can be summarized as attempts to implement the following equation:

$$\text{Interference Signal} + \text{Cancellation Signal} = 0. \tag{1.1}$$

The approach taken in [23] is slightly different from the others, so it will be discussed first. This approach utilizes a balanced oscillator which is fed into two 3 dB Lange couplers: the "positive" balanced signal is coupled into the Tx/Rx antenna while the "negative" balanced signal is routed to a second Lange coupler which is terminated on the coupled port with a $50\ \Omega$ load. The through ports on the Lange couplers are fed back and combined using a Wilkinson combiner. The recombined signals are 180° out of phase and cancel each other. The Rx signal is routed through the coupled port on the same Lange coupler used for the outgoing Tx signal and therefore follows the same signal path through the Wilkinson combiner. This work reports Tx-Rx isolation of 40.5 dB, of which, 21.5 dB is attributed to the circuit topology for single-tone signals in K-band.

In [24] and [25] similar circuit topologies using quadrature couplers are presented for vehicular radar applications. In both papers an arrangement of four quadrature (Lange or hybrid) couplers are used to provide both the Tx signal and and the inputs to in-phase (I) and quadrature (Q) mixers at the down-conversion stage. The Rx signal is also routed through the couplers and combined in-phase prior to a low-noise amplifier (LNA) and then split again to be mixed with the I and Q reference signals. The additional isolation provided in [24] and [25] between Tx and Rx are 13 dB and 13.77 dB, respectively. One disadvantage of the approach presented in both papers and the circuit presented in [23] is that there is – in an ideal case – minimum Rx signal path loss of 6 dB prior to the LNA. A second disadvantage is that the Tx power level is limited because the Tx signal is split four ways. The signal is

evenly distributed between the I and Q mixers, the transmit antenna, and -6 dB that is dissipated in the load of one coupler.

The theory of operation of a circuit called a reflected power canceler (RPC) is first shown in [27], and is further developed in [28]. A modified version of the same device appears in [29] along with additional linear control theory analysis. The system consists of a single antenna radiator with Tx and Rx portions of the system isolated using a typical ferrite circulator. In this scheme, the control loop is formed by splitting a portion of the Rx I and Q baseband signals into a vector control modulator. The resulting signal is then re-phased and modulated by a coupled portion of the Tx signal. The resulting signal is coupled into the Rx chain before the LNA. A block diagram of the RPC is shown in Fig. 1.4. The resulting additional isolation in [27] was 40 dB over 1.2 GHz of bandwidth in X-band in an ideal laboratory test and 20 dB over 250 MHz when attached to a prototype antenna. The results demonstrated in [29] are similar, however their laboratory performance was worse than in [27], with cancellation of 32 dB over 800 MHz of bandwidth.

In addition to the progress made in CW radar, other researchers have been working on approaches to STAR for wireless communications. In [1] and [31]–[34] the challenges and opportunities for wireless networks are presented. The circuit-level design utilized in the authors' research is based on using delay lines with phase and amplitude control to cancel self-interference signals. The magnitude and phase characteristics of the delay lines are electronically controlled, and the resulting signal is recombined with the Rx signal. All of the antenna configurations in these papers consist of separate Tx and Rx antennas, which will apply directly to the subsequent work presented in this thesis.

The approach taken in [31] is somewhat similar to the approach used for CW radar. A portion of the Tx signal is tapped off and is routed through active circuitry

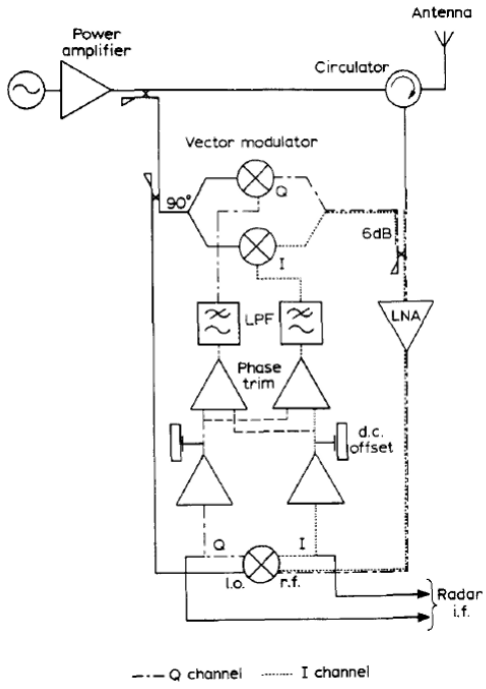

Figure 1.4: Block diagram of the reflected power canceler circuit from [27].

consisting of a phase aligner and a variable gain amplifier (VGA), and is subsequently filtered and recombined with the Rx signal. A power detector on the Rx portion of the circuit provides feedback to a digital to analog converter (DAC) that adjusts the gain and phase characteristics to minimize the self-interference signal. The authors report a maximum self-interference cancellation of 30 dB over a bandwidth of 83.5 MHz centered at 2.45 GHz. Quite similar architectures are utilized in [33] and [34], however these implementations use an increased number of Tx signal taps to improve isolation bandwidth. In addition, [33] provides a detailed analysis of the algorithm used to find optimum weighting coefficients and phases for the cancellation signal. The self-interference cancellation is shown to be a minimum of 30.6 dB in [34] over a 30 MHz bandwidth centered at 2.45 GHz. The figures of merit of the cancellation schemes referenced above can be found in table 1.1.

Table 1.1: Summary of the achieved cancellation levels and bandwidth of the STAR schemes.

Interference Cancellation Summary								
	[23]	[24]	[25]	[27]	[29]	[31]	[33]	[34]
Scheme	Quadrature Couplers	Quadrature Couplers	Quadrature Couplers	RPC	RPC	Tapped Delay-Line	Tapped Delay-Line	Tapped Delay-Line
Max Cancellation (dB)	21.5	15.1/15.1	13.8	35	35	30	40	30.6
Tx – Rx Isolation (dB)	40.5	25/25	35.3	55	N/A	48	75	90
BW	320 MHz	5/6.6 GHz	2 GHz	1 GHz	400 MHz	83.5 MHz	100 MHz	30 MHz
Tx – Antenna / Rx – Antenna Loss (dB)	>6/>6	>6/>6	>6/>6	N/A	N/A	N/A	N/A	N/A
f_c (GHz)	25.45	24/77	24	9.375	8.5	2.4	2.45	2.45

1.2 Reconfigurable and Wideband RF Electronics

In recent years many advances have been made in reconfigurable, multi-band, and wideband RF and microwave circuits [35], [36]. The integration of such components into a complete RF system is in the early phases of academic study [36]. In the development of a fully reconfigurable or wideband system the entire transceiver is subject to the performance of the lowest performing reconfigurable element [36]. These systems present an opportunity for high-level functional integration, but this utility is achieved at the expense of other performance characteristics. Sacrifices in metrics like noise figure (NF), insertion loss, phase noise, and gain may be required when compared to fixed elements [37], [38]. However, the ability to integrate multiple functions such as communications, radar, and electronic warfare through a single system interface provides opportunities for size, weight, and cost reduction [35]. In addition to the desire for wideband operation, ideally these systems will also incorporate tunable or reconfigurable self-interference cancellation. Many of the same trade-offs required for tunability and reconfigurability will be necessary to add the additional functionality enabled by STAR.

In general, the tuning mechanisms used in reconfigurable components tend

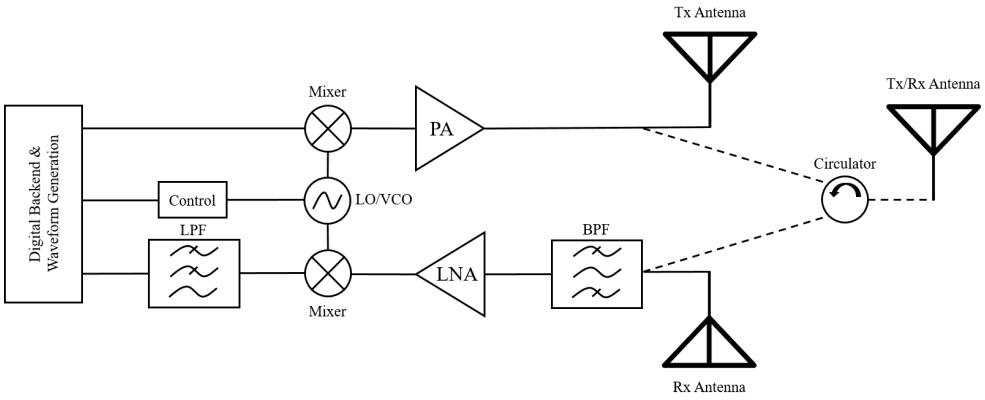

Figure 1.5: Essential superheterodyne transceiver components.

to be expensive yttrium iron garnet (YIG) [39] or slow such as mechanical or microelectromechanical structures (MEMS) [40]. Varactor diodes address both of these problems, but become lossy at higher frequencies due to both low self resonant frequencies and low quality factors [41]. Wideband devices offer a significant increase in flexibility, yet are also subject to potential out-of-band interference sources and increased noise. This is especially true for LNAs. Used to amplify low-power signals, while injecting a minimum amount of noise, wideband LNAs may be driven into non-linear modes of operation from out-of-band signals. The result is distortion of the desired Rx signal. In chapter 5 this effect is quantified using a wideband LNA and an out of band interfering signal. Therefore, the main focus of this literature review will be on state of the art LNAs, the other main transceiver components are also included.

There have been many recent developments in reconfigurable and wideband LNAs [42]–[47]. A system level analysis, found in [42], shows the benefits of reconfigurable LNAs in terms of power savings in low power Bluetooth applications. The power saving is accomplished by reconfiguring the LNA for different NFs, gain, and input-referred third-order intercept point (IIP3), based on the input power level. The analysis shows, that relative to an optimal automatic gain control algorithm, an

Table 1.2: Performance summary of wideband LNAs.

LNA Performance Summary					
	[43]	[44]	[45]	[46]	[47]
Process	CMOS	CMOS	CMOS	SiGe HBT	GaN FET
Tech. (μm)	0.13	0.18	0.13	0.18	0.15
S_{11} (dB)	< -10	< -12.8	< -8	< - 10	< - 10
G_{max} (dB)	9.5	10.2	13	21.3	14.5
BW (GHz)	2 – 4.6	3.1 – 10.6	3.1 – 4.8	5 – 20	4 – 16
NF_{min}	3.5	3.4	3.5	4.2	1.5
IIP3 (dBm)	-0.8	1	-6.1	-6.5	18
IP1dB (dBm)	-6	-10	-15.4	N/A	N/A
P_{diss} (mW)	16.5	6.36	3.4	116	150

additional 5–8 dB of relative power savings can be achieved. A similar result will be shown later in this thesis for the LNA of an integrated receiver module.

The LNA in [44] is comparable to the LNA tested in chapter 5. It is implemented in an 0.18 μm CMOS process. The bandwidth of this LNA is significantly increased compared to [43], with an operating range of 3.1–10.6 GHz. The gain bandwidth is actually significantly wider, from 2.5–13.2 GHz, but the input matching suffers on the high end of the band. The maximum gain of this amplifier measured to be 10.2 dB. The minimum noise figure of the LNA is 3.4 dB and a maximum of 4.47 dB across the band. The IIP3 of the device is stated to be 1 dBm and the DC power consumption is only 6.3 mW. The figures of merit for the other previously listed LNAs are summarized in table 1.2.

A number of reconfigurable [48] and wideband [49]–[51] power amplifiers (PAs) have recently been developed. The PA is typically the final system component before the signal is transmitted by the antenna. It plays the role of amplifying the desired Tx signal to the required power level to meet transmission requirements [18]. Typically, PAs are also responsible for consuming the most DC power in a transceiver [52]. Therefore, some current PA designs use reconfigurable gain cell configurations that effectively increase power added efficiency (PAE) [53].

Another important component in RF transceivers is the voltage controlled oscillator (VCO). The oscillator is responsible for providing a stable source for the RF carrier frequency. Since the carrier frequency defines the center of any signal the VCO is critical [3]. The main limitations of VCOs are in the phase noise that they add to the transmit signal. In addition, if a VCO is required in the STAR system circuitry, these phase noise sources will be uncorrelated. In [54] and [55] two tunable oscillators are presented utilizing capacitive varactor diode tuning. The oscillator presented in [54] shows an ultrawideband tuning range, from 5.6 to 16.8 GHz with phase noise less than -112 dBc/Hz at a 1 MHz offset.

Mixers are components used in RF the transceiver to perform multiplication of the RF signal with a locally generated oscillator. Although passive mixers are still widely used, there has been recent interest in wideband, active mixer topologies with conversion gain (CG) [56], [57]. Both passive and active mixer stages are typically high NF devices. Fortunately they do not appear until later in the receiver chain so their impact on overall system NF is minimized by the gain of the LNA [3]. However, mixers are also responsible for the overall linearity of the receiver because in addition to the desired signal, intermodulation product signals are also generated.

The mixer architecture presented in [56] is a an unbalanced input mixer with integrated active baluns on an 0.18 μm CMOS process. The device operates from 2–11 GHz with CG of 6.9 $\pm$ 1.5 dB and an IIP3 of 6.5 dBm, with P1dB of -3.5 dBm. The mixer operates with a supply bias of 1.8 V and consumes 25.7 mW of DC power. There is a maximum gain imbalance within the balun structure of approximately 2 dB. The maximum NF of the structure is 15.5 dB.

The technology shown in [57] is a differential Gilbert-cell type mixer with buffered inputs. The mixer operates from 1–10.5 GHz and the conversion gain is higher for this design at 14.5 dB. The P1dB and the IIP3 for the device are lower at

-10.4 dB and -10 dBm respectively. The high conversion gain of the device however, allows for the use of a lower gain, lower NF LNA stage, which is a typical trade-off scenario. The device operates with a supply voltage of 1.2 V with a DC power consumption of 14.4 mW.

The function performed by filters in an RF receiver is critical to the operation of the overall device. Without filtering the receiver subsystem is subject to any frequency the antenna element is capable of receiving. Filter responses are generally categorized into four categories, low-pass, high-pass, band-pass, and band-stop [58]. In addition to the response type, different filter shapes such as Butterworth, Chebyshev, and elliptic responses can be designed. Butterworth filters have an ideally flat phase response, while Chebyshev and elliptic filter designs are used to maximize the slope of the filter magnitude response [58].

The most important filter in the receiver is in the Rx path between the Rx antenna and the LNA. In order to pass the desired signal and attenuate other out-of-band signals a band-pass type filter response is desirable. For STAR operations, matching the group delay of this filter stage will be necessary to maintain interference cancellation. Reconfigurable and tunable filters have been developed using different tuning mechanisms [59]. Many of the tuning methods involve the use of varactor diodes, which are typically limited to low-frequency applications due to their low self-resonant frequency. Varactors are also limiting due to loss as a result of their low quality factor. However, recent developments in RF microelectromechanical (MEMS) show a capability for operation at higher frequencies, with greater tuning ranges [60]. Other low-loss structures that include piezoelectric actuators have also been demonstrated [61], [62], although the tuning range achieved is less than what is achievable using RF MEMS.

Tunable filter structures can also be made using magnetically biased materials

such as doped and undoped YIG [39], [63]. These early YIG filters demonstrated wide tuning ranges, for example 0.5–4 GHz is reported in [63]. Recently, YIG films have been developed for use in planar microwave filters [64], [65]. Unfortunately, in these works the tuning range is reduced to 50% and 8.15%, respectively. Traditional YIG structures also have other disadvantages: the requirement for external magnetic field biasing, the DC power consumed to create the magnetic field, and poor integration with printed circuit board (PCB) and integrated circuits.

The final element included in this literature review of tunable and reconfigurable devices is the antenna. Many tunable, frequency reconfigurable, and pattern reconfigurable antennas have been designed [66]–[70]. As detailed in [71] and [72], there are many challenges for designers of such antennas including maintaining radiation efficiency and input matching. There has also been research conducted on reconfigurable polarization [69], beamwidth reconfiguration [70], element beamsteering [73], and frequency tuning [66], [67], [74]. Several ultra-wideband antennas dish and horn type antennas are discussed in [75] and many planar ultra-wideband antennas are discussed [76].

This section has covered the characteristics of many state of the art devices that, if assembled, constitute a complete wideband receiver. There are many tradeoffs involved in the selection of individual components. The main trade-offs that must be considered are heavily dependent on input and output power levels of the system design. Systems that require components capable of high power handling are generally less efficient. This is because components using materials capable of handling the high power levels often introduce additional intrinsic losses. In addition to the trade-offs required for high power handling, the wideband nature of the devices also subjects them to out-of-band interference. Therefore, tunable or reconfigurable filtering is also necessary for the Rx front end. Many of the

same limitations will apply to STAR as components for STAR are developed for reconfigurable and wideband operation. These components and systems will likely require trading cancellation magnitude or bandwidth for requirements such as power handling.

1.3 Organization of Work

This thesis is divided into several parts. The second chapter develops a mathematical framework for analyzing phase cancellation. In chapter 3, a methodology is developed for implementing passive self-interference cancellation networks for dual-antenna STAR. Two such passive networks are designed using directional couplers to provide anti-phasing and to combine the cancellation signal with the interference signal at the Rx port. In the first device, a delay-line based circuit is used for comparison to the new method presented. In the second, a new hairpin resonator based circuit is utilized to more accurately match the phase characteristics of the antenna mutual coupling. The theory of operation for each device used in the final designs is provided individually, and an analysis of the overall device is given. The design goals of this portion of the work are two-fold: to maximize the -40 dB coupling bandwidth between the two antennas and to minimize the power loss to the self-interference cancellation device. The complete devices are simulated and fabricated on high frequency PCB material. Finally, the measured results are discussed. An earlier version of the passive STAR network utilized an exponentially tapered T-junction power divider, a new theory of operation for this device is developed in chapter 4.

Afterwards, an analysis of the system level performance effects of wideband LNAs is performed. In chapter 5, a simulated quadrature phase-shift keyed (QPSK) communications system is set up utilizing the parameters of a proprietary receiver module. This is done in order to test the effects of out-of-band interference on

in-band system performance. Interference measurements are also conducted on the LNA to verify the simulated results. The proprietary LNA's bias current can also be reconfigured or set into an adaptive biasing mode in response to the input RF power stimulus. This adaptive biasing feature is investigated for its benefits in a QPSK receiver system subjected to an out-of-band interference signal. In addition, an analysis for power savings in a large array with the adaptive biasing feature enabled is performed. Finally, chapter 6 concludes the thesis and makes recommendations for future work on this topic.

2 Phase Cancellation

This chapter serves as a mathematical introduction to the phase cancellation scheme that will be utilized in this work. As the basis of several of the other schemes described in the introduction it is important to develop an understanding of the phasing of signals in microwave devices. This section represents a small slice of complex analysis, for a more complete treatment of complex variables see [77].

2.1 Mathematical Representation

Since nearly all transmitted RF signals are sinusoidal in nature it then makes sense to begin with such a signal as the basis for this analysis. For a single tone sinusoidal transmit signal,

$$a(t) = A\cos\left(2\pi ft + \phi\right) = \Re\{Ae^{j(2\pi ft+\phi)}\}, \tag{2.1}$$

where A is the amplitude of the signal, f is frequency of the tone, and ϕ is the phase. Such a signal can also be represented as a phasor of the form,

$$\mathbf{A} = Ae^{j\phi} \tag{2.2}$$

$$a(t) = \Re\{\mathbf{A}e^{j2\pi ft}\} = \Re\{Ae^{j(2\pi ft+\phi)}\}. \tag{2.3}$$

It is customary in AC circuit analysis, since for a fixed frequency the response of the circuit is also fixed, to use the phasor form $Ae^{j\phi}$ [78]. In order to return to the time domain representation, in the end the resultant phasor is multiplied by $e^{j2\pi ft}$ before taking the real part of the expression. The mathematical convenience of phasors for the analysis of phase cancellation comes from the fact that, using Euler's

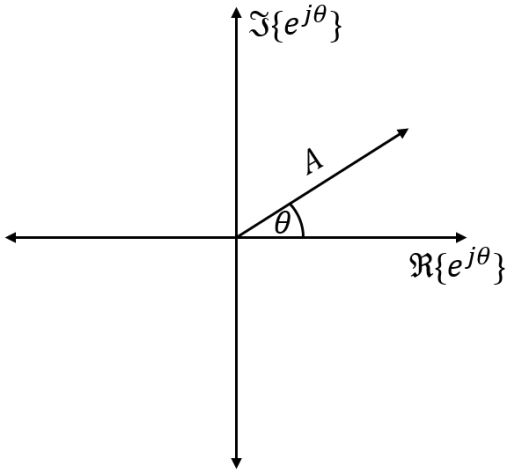

Figure 2.1: Vector representation of a phasor.

formula (2.4), they can be represented as vectors in the complex plane, Fig. 2.1.

$$e^{j\theta} = \cos(\theta) + j\sin(\theta) \tag{2.4}$$

Canceling the phasor **A** can be accomplished by summing **A** with a phasor $\mathbf{A}'$ of equal magnitude and opposite direction.

The self-interference signal of interest is modified in magnitude and phase by the coupling path from the Tx antenna to the Rx antenna. Shown in Fig. 2.2, the self-interference signal **B** can be found by multiplying **A** by the transfer function between the two antennas,

$$\mathbf{B} = \mathbf{A}|S_{a21}|e^{j\theta_1} = A|S_{a21}|e^{j(\theta_1+\phi)}. \tag{2.5}$$

The cancellation signal **C** is also a modified version of the original Tx signal **A**,

$$\mathbf{C} = \mathbf{A}|S_{c21}|e^{j\theta_2} = A|S_{c21}|e^{j(\theta_2+\phi)}. \tag{2.6}$$

In the ideal case the sum of signals **B** and **C** is zero.

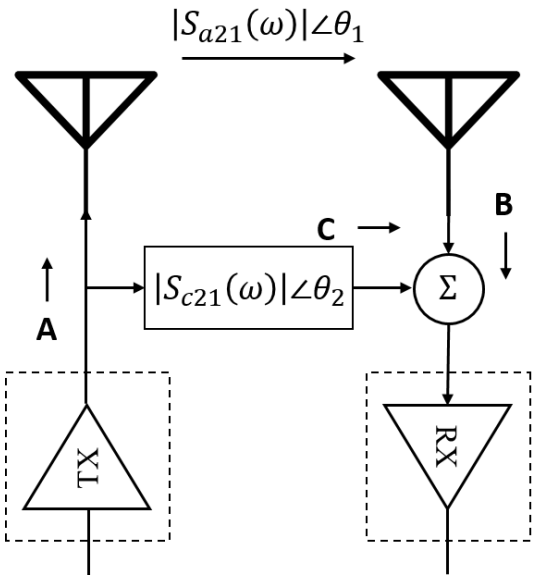

Figure 2.2: Block diagram showing the transfer function between Tx and Rx along with the desired transfer function of the cancellation circuit.

$$\begin{aligned} \mathbf{B} + \mathbf{C} = A|S_{a21}|e^{j(\theta_1+\phi)} + A|S_{c21}|e^{j(\theta_2+\phi)} = 0 \\ A|S_{a21}|e^{j(\theta_1+\phi)} = -A|S_{c21}|e^{j(\theta_2+\phi)} \end{aligned} \tag{2.7}$$

After some manipulation, and using the fact that $e^{j\pi(2n+1)} = -1$ where n is an integer, the following identifications can be made:

$$\begin{aligned} |S_{a21}| = |S_{c21}|, \\ \theta_2 = \theta_1 - \pi\left(2n+1\right). \end{aligned} \tag{2.8}$$

Therefore, in order for phase cancellation to occur the magnitude response of the cancellation circuit must be equal to that of the coupling path. Additionally, the phase response of the self-interference cancellation circuit must equal the phase response of the interference plus an odd integer multiple of 180°. This analysis does neglect potential noise that may be added through the cancellation circuit. For instance, if active devices are used in the cancellation circuit $1/f$ noise will be

introduced, which will be uncorrelated to the noise from the transmitter. However, the devices used to implement the cancellation circuit in this thesis are passive so noise is not included in this analysis.

2.1.1 Small Phase Variations

For a practical device small variations in manufacturing and other imperfections in design and modeling will lead to small variations in the phase matching, $|\Delta\phi|$. It is therefore important to understand what this small variation implies in terms of maximum achievable cancellation. Assuming that the magnitude transfer function is perfectly matched, for the normalized power signal $\mathbf{A}$, and cancellation signal $\mathbf{A}_c$, which is 180° out of phase with $\mathbf{A}$ plus a small phase variation $|\Delta\phi|$,

$$\begin{aligned}
\mathbf{A} + \mathbf{A}_c &= e^{j\phi} + e^{j(\phi+\pi+|\Delta\phi|)} \\
&= e^{j\phi} - e^{j(\phi+|\Delta\phi|)} \\
&= e^{j\phi}\left[1 - e^{j|\Delta\phi|}\right] \\
&= e^{j\left(\phi+\frac{|\Delta\phi|}{2}\right)}\left[e^{-j\frac{|\Delta\phi|}{2}} - e^{j\frac{|\Delta\phi|}{2}}\right] \\
&= -2je^{j\left(\phi+\frac{|\Delta\phi|}{2}\right)}\sin\left(\frac{|\Delta\phi|}{2}\right) \\
&\approx -j|\Delta\phi|e^{j\left(\phi+\frac{|\Delta\phi|}{2}\right)}
\end{aligned} \tag{2.9}$$

where the final approximation is for small angles of $\sin(|\Delta\phi|/2)$. By taking the negative logarithm of the magnitude of this expression we now have the maximum phase cancellation achievable for a given phase difference $|\Delta\phi|$ between the interference and cancellation signals,

$$\mathbf{PC}_{max} = -10\log\left(|\Delta\phi|\right). \tag{2.10}$$

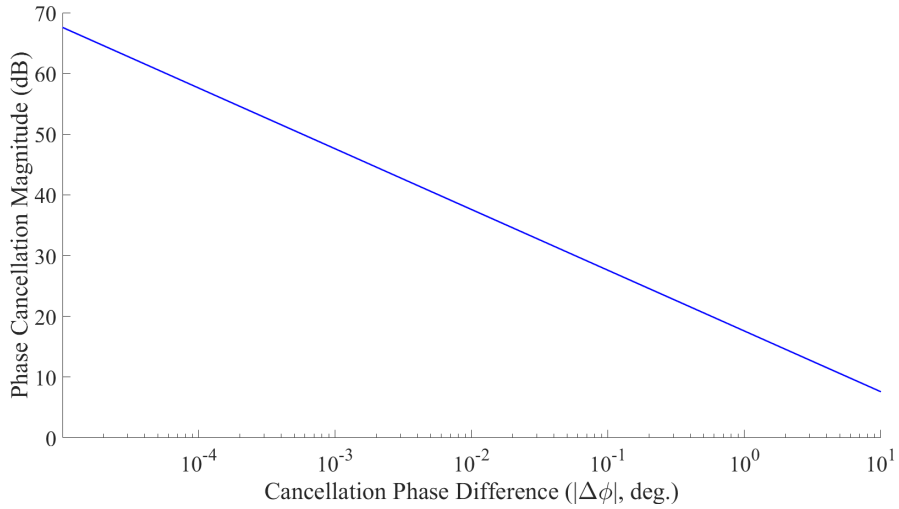

Figure 2.3: Maximum achievable phase cancellation for small phase variations.

Although this analysis is conducted at a single frequency, it applies for all frequencies at which phase cancellation occurs. For a practical system it is necessary for there to be a small bandwidth where this condition applies. In order to achieve phase cancellation of 20 dB, $|\Delta\phi| \leq 0.573°$. This analysis is directly applicable to the phase matching in subsequent chapters. A logarithmic plot showing the maximum achievable phase cancellation for small $|\Delta\phi|$ is shown in Fig. 2.3.

2.1.2 Small Magnitude and Phase Variations

In addition to the analysis conducted above for small phase variations, a more general analysis can be conducted that takes into account both magnitude and phase variations in the cancellation signal. In terms of small variations in magnitude $|\Delta M|$ (%) and phase $|\Delta\phi|$ of the cancellation signal,

$$\begin{aligned}
\mathbf{A}+\mathbf{A}_c &= e^{j\phi} + (1+|\Delta M|)\, e^{j(\phi+\pi+|\Delta\phi|)} \\
&= e^{j\phi} - (1+|\Delta M|)\, e^{j(\phi+|\Delta\phi|)} \\
&\vdots \\
&= e^{j\left(\phi+\frac{|\Delta\phi|}{2}\right)} \left[-2j\sin\left(\frac{|\Delta\phi|}{2}\right) - |\Delta M| e^{j\frac{|\Delta\phi|}{2}}\right]
\end{aligned} \tag{2.11}$$

Taking the magnitude of (2.11), and again using the approximation that, $\sin(x) \approx x$, gives the following result,

$$\begin{aligned}
|\mathbf{A}+\mathbf{A}_c| &= \sqrt{4\sin^2\left(\frac{|\Delta\phi|}{2}\right) + 4|\Delta M|\sin^2\left(\frac{|\Delta\phi|}{2}\right) + |\Delta M|^2} \\
&\approx \sqrt{|\Delta\phi|^2 + |\Delta M|^2}
\end{aligned} \tag{2.12}$$

The function surface that results from taking the negative logarithm of (2.12) consists of concentric ellipses going to infinity as $|\Delta\phi|$ and $|\Delta M|$ tend towards zero. The "height" of the ellipse represents the maximum achievable cancellation for a the combinations magnitude and phase variation that lie on it. A plot of the curves with $|\Delta\phi|$ and $|\Delta M|$ plotted in logarithmic format is shown in Fig. 2.4.

Now that the relationship between the variation in magnitude and phase and the achievable cancellation is established, the microwave devices that can achieve such performance will be shown. The implementation of two circuit networks for phase cancellation will be discussed in the next chapter. It will be shown that the magnitude and phase characteristics of the circuit can be designed to match the mutual coupling between two closely spaced antennas. The two devices are designed using a commercial simulator, and are subsequently fabricated and measured.

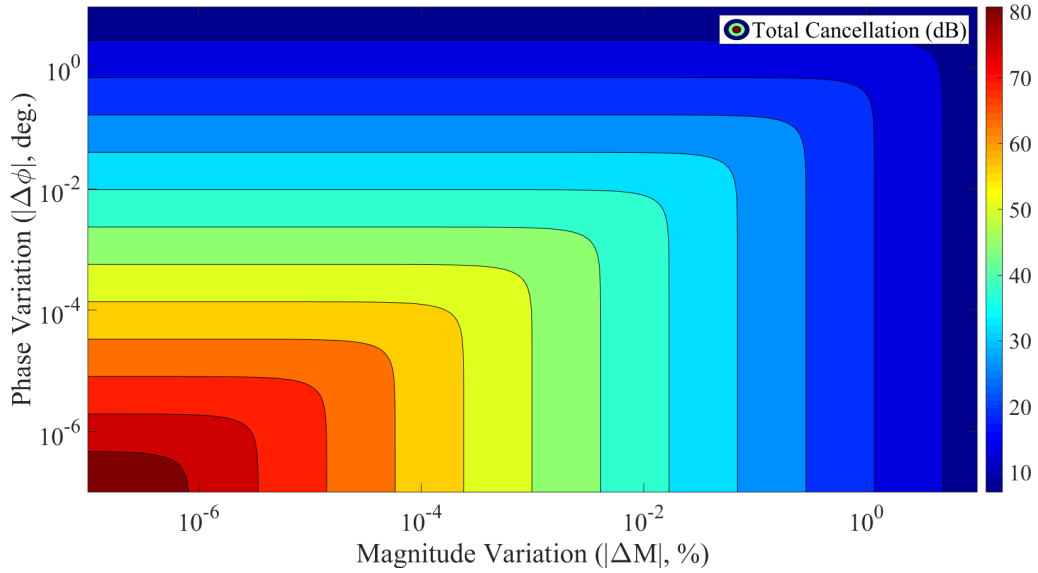

Figure 2.4: Maximum phase cancellation achievable for variations in both magnitude and phase of the cancellation signal.

3 Devices and Theory

The mathematics developed in the previous chapter show that it is possible to perfectly cancel self-interference signals, for at least single tone sinusoids. However, for any practical radar or communications system a non-zero bandwidth transmission occurs. In communications systems, in order for information transmission to occur the fundamental carrier or center frequency is modulated by a waveform that represents the data [3]. In radar, although a CW radar can be utilized in order to perform moving target indication (MTI) and velocity estimation, a frequency modulated carrier is utilized to perform ranging [2]. For a practical self-interference cancellation circuit we must utilize devices that provide the required odd multiple of 180° for a band of frequencies.

The first portion of this chapter will develop the theory of the microwave devices utilized in this work. A microstrip patch antenna will be designed and then an arrangement of two such antennas will be characterized for mutual coupling. Next, the properties of the non-radiating microwave devices that will achieve the phase and magnitude criteria required are shown. A directional coupler will be used as a tap/phase-shifter in order to obtain the required magnitude and phase characteristics. The second element, which will be utilized to match the phase characteristics of the antenna element, is a microstrip hairpin resonator, which could also be regarded as a one-pole filter. A second implementation using only a delay-line for phase matching is also implemented for comparison.

Subsequent to the development of the device theory mentioned above, simulated results of the planar device layouts will be shown and discussed. The phase and amplitude characteristics of the developed self-interference cancellation devices will be shown to match the coupling characteristics of the patch antennas over a non-zero bandwidth. Finally, a circuit combining the antenna elements and the phase

cancellation circuit will be presented.

For the PCB design Rogers RO4350B high-frequency dielectric substrate with $\epsilon_r = 3.66$, $h = 60$ mil $= 1.524$ mm, and loss tangent of $\tan(\delta) = 0.0037$ was chosen. These values are required for several of the subsequent calculations shown.

3.1 Microstrip Patch Antenna

Microstrip patch antennas are widely utilized in PCB design [79]. The antenna consists of a rectangular patch of copper on the top layer of the circuit board, above a ground plane. The radiation pattern is normal to the patch with typical achieved gains of 5-8 dBi. The electric field polarization radiated from the patch is in the $\hat{y}$ direction, with reference to the coordinate system in Fig. 3.1. The patch itself can be modeled as a cavity resonator with radiating slots that extend beyond each end of the resonator [80]. From this general model a design procedure for determining the physical parameters of the patch, as presented in [79] is used. The important physical parameters of the patch are the relative permittivity (ϵ_r) of the PCB material, the substrate height (h), and the length (L) and width (W) of the patch. In addition, in order for the patch to be matched to the characteristic impedance of the transmission line, an inset feed is used, the inset length is denoted y_0. These physical parameters are shown in Fig. 3.1.

Design formulas provided in [79] for a resonant frequency of $f_r = 3.3$ GHz for the patch antenna were used. From [79], the width that maximizes the radiation efficiency of the patch, W is,

$$W = \frac{v_0}{2f_r}\sqrt{\frac{2}{\epsilon_r + 1}}, \tag{3.1}$$

where v_0 is the speed of light in a vacuum. The next calculated parameter is the effective dielectric constant of the microstrip substrate, which takes into account

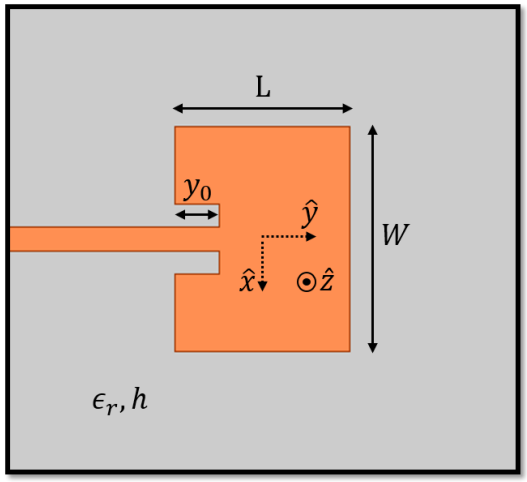

Figure 3.1: Design parameters for a microstrip patch antenna.

fringing fields at the edge of the microstrip line and fields in the air above the substrate [79].

$$\epsilon_{r,eff} = \frac{\epsilon_r + 1}{2} + \frac{\epsilon_r - 1}{2}\left[1 + 12\frac{h}{W}\right]^{-\frac{1}{2}} \tag{3.2}$$

The determination of the patch length, L, is complicated by the fact that the overall length of the patch must be decreased in order to compensate for the length (ΔL) occupied by the equivalent radiating slots [79].

$$\begin{aligned} \Delta L &= 0.412h\frac{(\epsilon_{reff} + 0.3)\left(\frac{W}{h} + 0.264\right)}{(\epsilon_{reff} - 0.258)\left(\frac{W}{h} + 0.8\right)} \\ L &= \frac{\lambda}{2} - 2\Delta L = \frac{v_0}{2f_r\sqrt{\epsilon_{reff}}} - 2\Delta L \end{aligned} \tag{3.3}$$

The calculated length and width from (3.3) and (3.1) are 23.3 mm and 29.8 mm respectively. The resulting patch antenna has a high input resistance at resonance relative to the 50 Ω transmission line feed used. Either a quarter-wave transformer or an inset feedline can be used to match the proposed antenna [18], [79]. The method chosen for this design was to use an inset feed of length y_0. In order to calculate the length of the inset the input resistance (conductance) of the antenna is calculated at

resonance [79].

$$R_{in} = \frac{1}{2\left(G_1 + G_{12}\right)} \tag{3.4}$$

Where G_1 is the antenna input conductance of one radiating slot, and G_{12} is the mutual conductance between the two (upper and lower) radiating slots. Integral formulas are given for these values in [79],

$$\begin{aligned} G_1 &= \frac{1}{120\pi^2}\int_0^{\pi}\left[\frac{\sin\left(\frac{k_0 W}{2}\cos\theta\right)}{\cos\theta}\right]^2 \sin^3\theta d\theta, \\ G_{12} &= \frac{1}{120\pi^2}\int_0^{\pi}\left[\frac{\sin\left(\frac{k_0 W}{2}\cos\theta\right)}{\cos\theta}\right]^2 J_0\left(k_0 L\sin\theta\right)\sin^3\theta d\theta, \end{aligned} \tag{3.5}$$

where J_0 is the Bessel function of first kind, zeroth order and k_0 is the freespace wave number at the resonant frequency, $k_0 = \frac{2\pi}{\lambda_0}$. The inset length, y_0, required to achieve desired input resistance is calculated using the formula [79],

$$R_{in}(y = y_0) = \frac{1}{2\left(G_1 + G_{12}\right)}\cos^2\left(\frac{\pi}{L}y_0\right). \tag{3.6}$$

The resulting calculation shows that $R_{in} \approx 210\ \Omega$ and that the required inset length y_0 is 6.8 mm. The design is then physically laid out in ANSYS Electronics and simulated. The results from the simulation show a peak antenna gain of 7.42 dBi at 3.31 GHz and an input reflection coefficient of -31 dB at 3.31 GHz. The -10 dB bandwidth of the antenna is 52 MHz which is equivalent to a fractional bandwidth of 1.57 %. The simulated radiation efficiency of the patch antenna is 84%. The input reflection coefficient is shown in Fig. 3.2 and the normalized E-plane and H-plane gain patterns, including cross-polarization, are shown in Fig. 3.3.

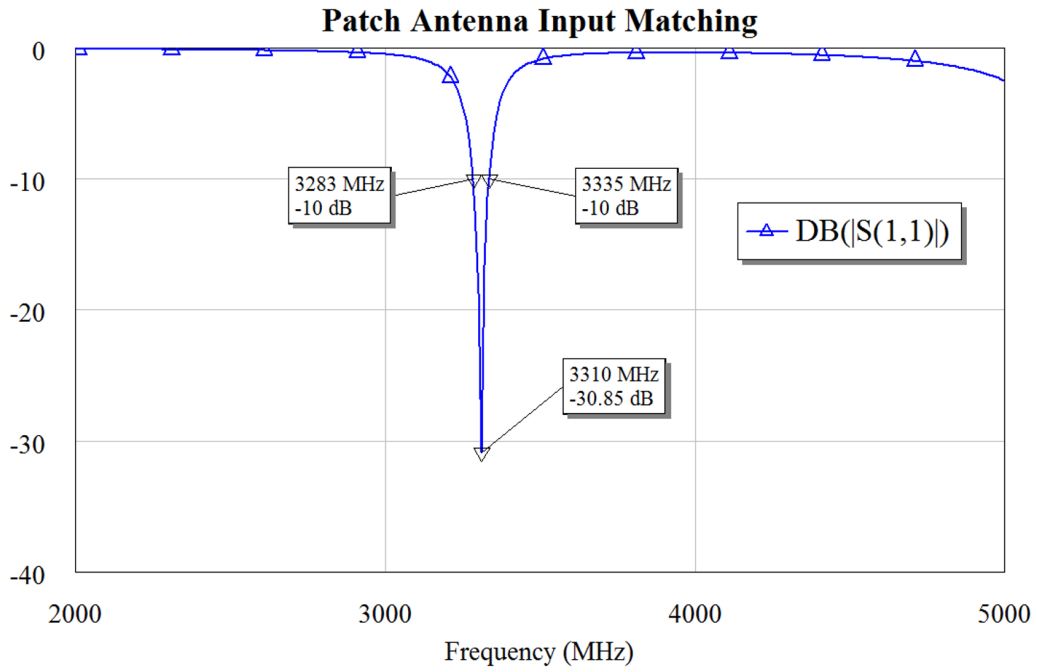

Figure 3.2: Simulated input reflection coefficient of the microstrip patch antenna.

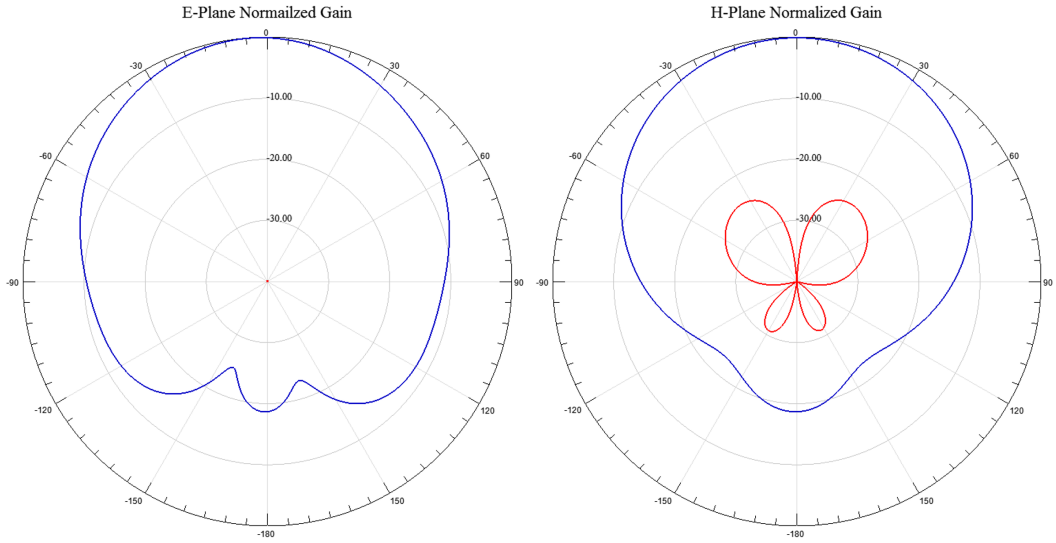

Figure 3.3: Normalized simulated antenna patterns for the microstrip patch antenna, co-pol is blue and cross-pol is red.

3.2 Patch Antenna Mutual Coupling Characterization

In order to address the problem of mutual coupling between closely spaced antennas described, the coupled energy must be accurately characterized. Using ANSYS Electronics a second antenna was added to the original design. The antenna separation used was $\lambda_0/2 = 45.5$ mm, this spacing was chosen because it is typical of the spacing used in arrays [79]. From the simulated results the de-embedded S-parameter magnitude and phase characteristics for the mutual coupling were extracted. The wave-port excitations in ANSYS Electronics were de-embedded by a distance of 38.35 mm as shown in Fig. 3.4. This distance places the phase reference of the antenna mutual coupling at the location where the feedline would connect to the patch if there were no inset. This is done so that when the feed structure is designed in NI AWR Microwave Office no compensation for the phase of the antenna feedlines used in ANSYS Electronics is necessary.

The simulation shows that the maximum of the coupling between the antennas

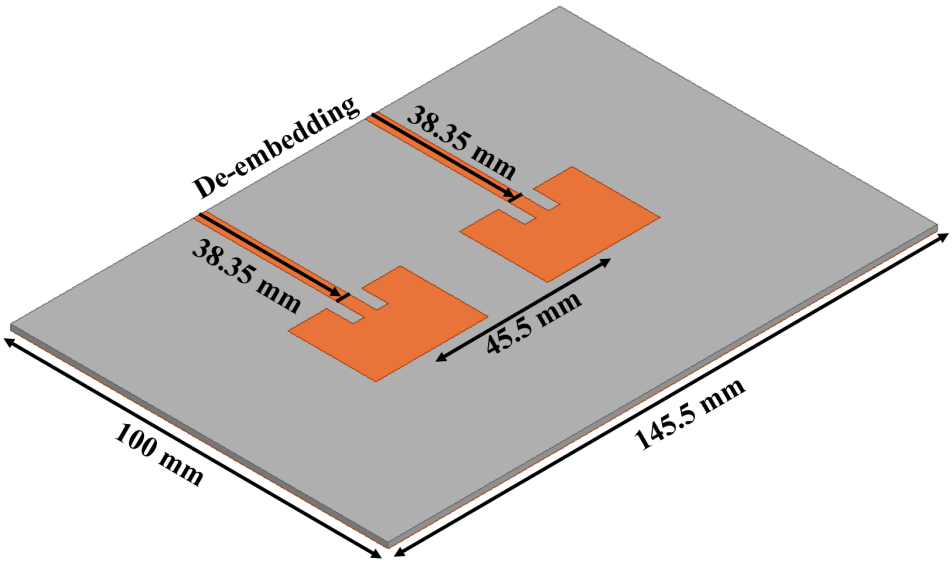

Figure 3.4: Isometric view of the simulated two-antenna configuration for characterizing mutual coupling.

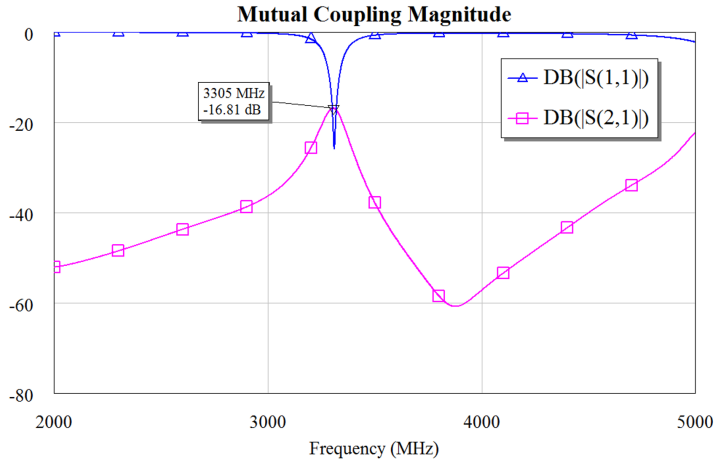

(a)

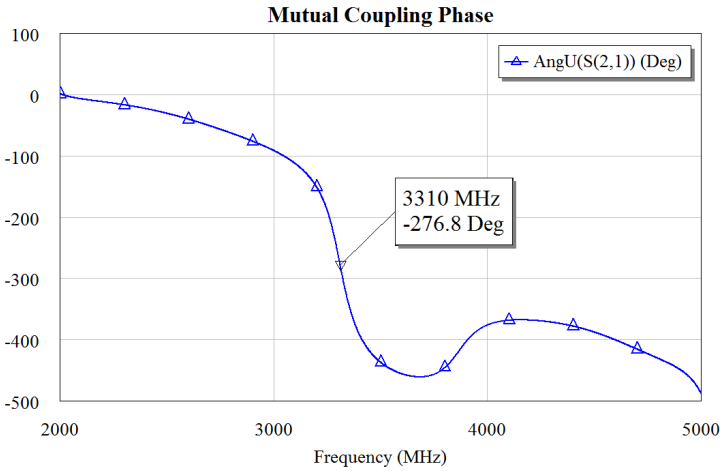

(b)

Figure 3.5: (a) Magnitude and (b) phase response of the two-antenna configuration.

occurs at 3.31 GHz and is approximately -16.8 dB. The magnitude and phase characteristics of the mutual coupling are shown in Fig. 3.5. For the two-antenna configuration it was found that there is also a reduction in the simulated radiation efficiency of the patch antenna from 84% to 81.2%. Now that the mutual coupling has been characterized the other required devices for the self-interference cancellation circuit can be designed.

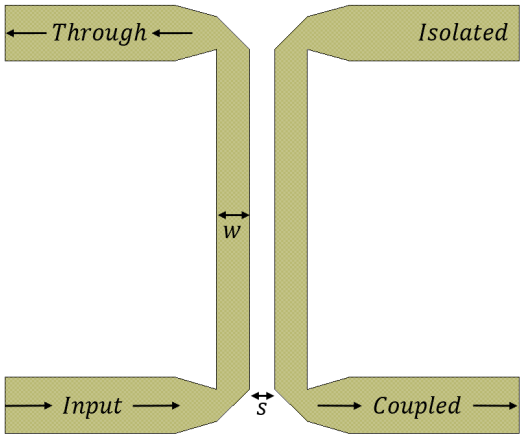

Figure 3.6: Depiction of a microstrip-line directional coupler.

3.3 Directional Coupler

The first device that is critical to the function of the self-interference cancellation circuit is the directional coupler. The device consists of two parallel transmission line sections that are placed in close proximity. This enables some power to be coupled from one transmission line section to the other [18]. The device has four ports, labeled: input, through, isolated, and coupled. For reference, a standalone directional coupler is shown in Fig. 3.6. One of the primary reasons for utilizing directional couplers in this work is that the differential phase between the through and coupled ports is 90°. Since two of these devices will be used in the self-interference mitigation circuit, a total phasing of 180° will be added to the signal. The primary utility of the directional couplers is the ability to design for the desired coupling magnitude. The differential phasing is also used later during the final PCB design to determine the required length of the antenna feed lines.

The methodology used to analyze and describe the coupling phenomenon for this and many other microwave devices is called even-odd mode analysis. In the even mode, two neighboring ports are excited with equal amplitude voltages, creating

an open circuit (magnetic wall) between the two strips. In the odd mode the ports are excited with equal magnitude, opposite sign excitations, creating a short circuit condition (electric wall) at the symmetry plane between the strips. From these excitation configurations, even mode and odd mode characteristic impedances, Z_{0e} and Z_{0o} can be calculated for the overall structure. The coupling coefficient, C, between the two strips is defined as,

$$C = \frac{Z_{0e} - Z_{0o}}{Z_{0e} + Z_{0o}}. \tag{3.7}$$

However, the required coupling coefficient is normally known prior to designing the directional coupler. Then for the choice of coupling coefficient C expressions for Z_{0e} and Z_{0o} are given by,

$$\begin{aligned} Z_{0e} &= Z_0 \sqrt{\frac{1+C}{1-C}}, \\ Z_{0o} &= Z_0 \sqrt{\frac{1-C}{1+C}}. \end{aligned} \tag{3.8}$$

For a well matched device it is also required that $\sqrt{Z_{0e} Z_{0o}} = Z_0$.

For this work a coupling coefficient C of -8.5 dB is required. The calculated even and odd mode impedances required are 74.2 Ω and 33.7 Ω, respectively. Although there are numerical methods available for calculating these impedances for microstrip lines [81], it is much more expedient to utilize commercial software to calculate the required physical parameters for the coupling gap (s) and transmission line widths (w). The coupled line sections are $\lambda/4$ at the center frequency of operation, which is 13.3 mm at 3.3 GHz in Rogers RO4350B substrate.

A software tool embedded in NI AWR Design Environment called TXLine is used to calculate the line parameters that meet the even/odd-mode impedance requirements. The required spacing for the coupling gap is 0.2 mm and the transmission

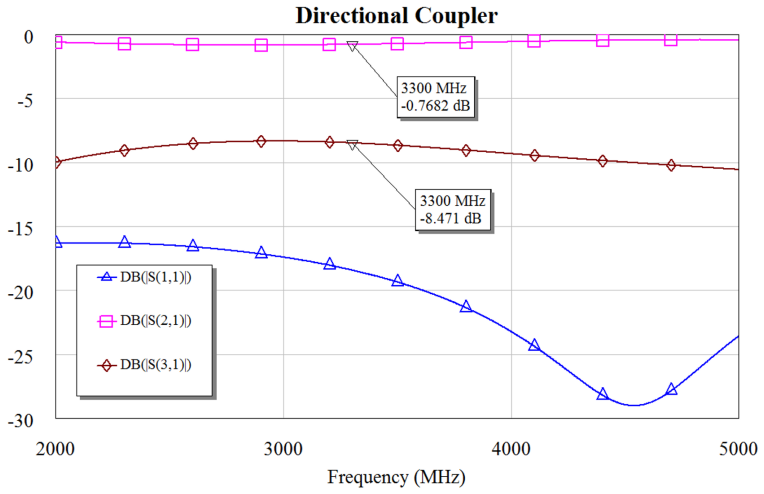

(a)

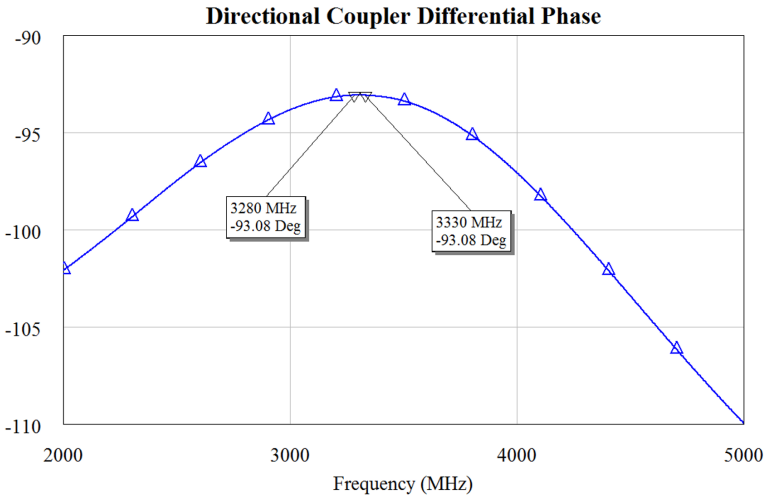

(b)

Figure 3.7: Directional coupler S-parameters (a) magnitude and (b) differential phase response.

line width is 1.9 mm. The device is then constructed and simulated using NI AWR Microwave Office. The magnitude of the device S-parameters and differential phase between the through and coupled ports of the simulated coupler are shown in Fig. 3.7. At 3.3 GHz the insertion loss of the directional coupler is 0.77 dB and the required -8.5 dB coupling is achieved. The return loss is below 15 dB from 2–5 GHz and the

transmission to the isolated port is less than -20 dB across the same band.

One of the limitations in using basic directional couplers in work requiring a more broadband differential phase response is the unequal phase velocity of the even- and odd-mode waves [18]. The cause of the different phase velocities between the even and odd modes is due to the use of an inhomogeneous transmission line configuration (microstrip line) [82]. In the even propagation mode the fields are distributed both in the air and in the material substrate, leading to a decreased effective dielectric constant. In the odd mode, the fields are primarily concentrated in the substrate medium and the phase velocity is increased.

Two main methods exist for compensating the different phase velocities for directional couplers, the goal of each is to increase the effective phase length of the device in the odd-mode. The first method uses capacitive loading. By capacitively loading the directional coupler the even mode is unaffected due to the open circuit condition [82], [83]. However, the odd-mode wave "sees" these additional capacitors and its phase length is increased accordingly. The capacitors used can either be lumped or interdigital [82]. The second method is to use a geometric configuration of the transmission lines that increases the distance traveled by the odd-mode wave [84]. The cancellation circuits developed in this thesis are narrowband, so no compensation in the directional couplers was utilized.

3.4 Delay-Line

From basic transmission line theory it is well known that a transmission line of length L has an associated phase delay [18]. In the theory of lossless transmission lines this phase delay, θ, is equal to,

$$\theta = -\beta L, \tag{3.9}$$

where β is the the propagation constant in the medium. This propagation constant is related to the wave velocity, v_p, and the wavelength in the medium, λ, by,

$$\beta = \frac{2\pi f}{v_p} = \frac{2\pi}{\lambda}. \tag{3.10}$$

Since v_p is not a function of frequency in the region where our device operates there is a linear relationship between the phase delay, $\theta = -\beta L$, and the operating frequency. Therefore, once the phase delay of the antenna has been determined at the operational frequency, the overall phase delay of the transmission line placed between the two directional couplers can be computed. Since the directional couplers contribute the required 180° to achieve phase cancellation, the length of transmission line will be equal to the phase-length of the mutual coupling response,

$$L = -\frac{\theta_{MC}}{\beta} = -\frac{\theta_{MC} v_p}{2\pi f_0}. \tag{3.11}$$

Using (3.2) in the equation, $v_p = v_0/\sqrt{\epsilon_{r,eff}}$, the velocity of propagation on the microstrip line is computed. The resulting phase constant from (3.10) for transmission lines at 3.3 GHz is -6.75°/mm.

3.4.1 Delay Line Phase Matching

Due to the linear nature of the phase characteristics of the delay-line it can only be used to match the phase of the antenna mutual coupling at one frequency. This is why multiple delay-line taps were utilized in [34] and [33]. However, for narrowband operation, such as in CW or narrowband FMCW radar, a single delay-line may prove to be sufficient. Since the delay-line is placed between two 90° phase shifts, the phase of the delay-line must match the antenna mutual coupling phase at 3.31 GHz. The phase of the mutual coupling at 3.31 GHz is -276.8°, therefore a delay line of

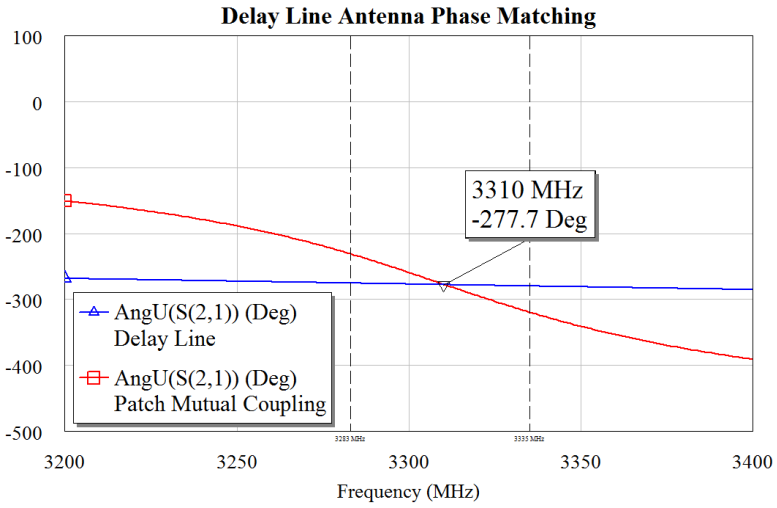

Figure 3.8: Phase matching between the delay-line and the antenna mutual coupling. Vertical bars depict 10 dB antenna bandwidth.

length, $L = 41.0$ mm would be required to match the antenna unwrapped phase. This length will change later however, due to the length of the antenna feeds. The phase matching between the antenna and the delay line is shown in Fig. 3.8.

3.5 Hairpin Filter

The second implementation used in an attempt to match the phase characteristics of the antenna mutual coupling was a hairpin type resonator [58], [85]. Since both are single resonant structures, it was hypothesized that the phase characteristics of a $\lambda/2$ length hairpin resonator would closely match the phase characteristics of the antenna. In order to provide phase cancellation over a wider bandwidth, it is necessary to add an element between the directional couplers that matches the phase characteristics of the antenna mutual coupling with more accuracy than a simple delay line. Because the resonator behaves like a single-pole filter [58], it can be designed in such a way that it approximates the magnitude and phase response of the antenna coupling.

The single-pole filter is designed using the methodology outlined in [86] and is

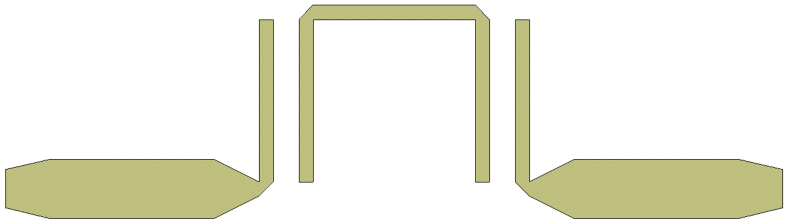

Figure 3.9: Layout of the hairpin filter used for phase matching.

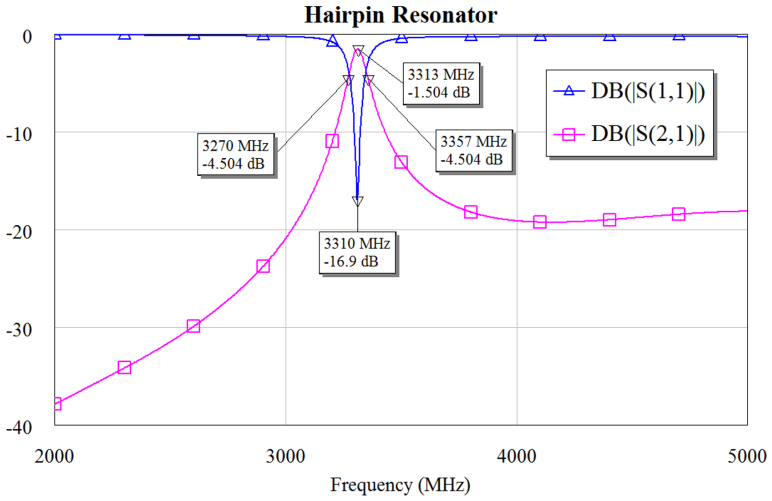

Figure 3.10: Response of the designed hairpin filter element.

shown in Fig. 3.9. The antenna mutual coupling is used to determine the resonator center frequency and 3 dB bandwidth. The 3 dB bandwidth of the coupling response is 89 MHz, with a center frequency of 3.31 GHz, which results in a fractional bandwidth (FBW) of 2.69%. The only filter parameter we must acquire for this design is the external quality factor,

$$Q_{ext} = \frac{g_0 g_1}{\text{FBW}}, \tag{3.12}$$

where $g_0 = 1$ and $g_1 = 2$ are the generalized filter coefficients for a first order Butterworth filter. The required Q_{ext} for this design is 74.4.

If an antenna with multiple resonances, such as a stacked patch antenna [87], were utilized it is hypothesized that a multi-pole filter may be used. The filter element is implemented in NI AWR Microwave Office using the same procedure outlined in the section on directional couplers, and the resulting filter response is shown in Fig. 3.10. The response matches the mutual coupling bandwidth within 2 MHz in bandwidth, with an insertion loss of 1.5 dB and a return loss of 16.9 dB at 3.31 GHz.

3.5.1 Hairpin Filter Phase Matching

Now that the hairpin filter is implemented, some additional work is required to match the phase characteristics of this element to the antenna. This is accomplished through the use of two short delay-lines placed at the input and output of the filter. The resultant phase is matched within 0.5° to that of the antenna mutual coupling over a bandwidth of approximately 6 MHz, the result is shown in Fig. 3.11.

The phase of the filter can be matched more closely to that of the antenna mutual coupling. However, this requires an increase in the external quality factor of the filter.

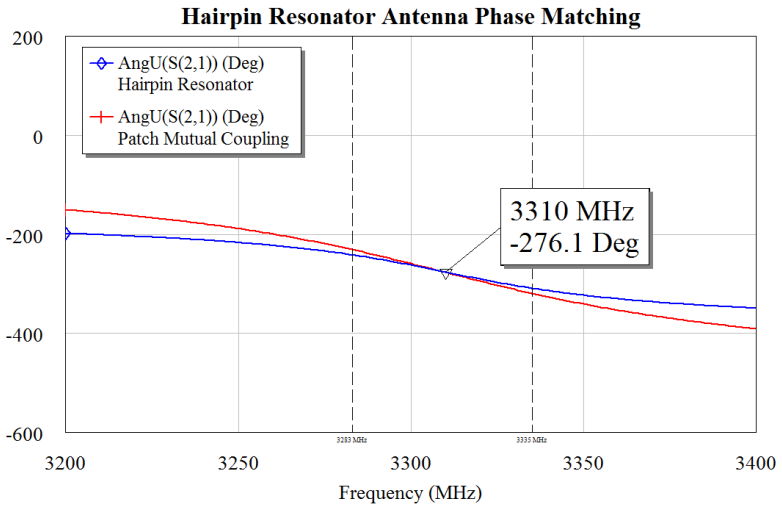

Figure 3.11: Phase matching between the hairpin resonator and the antenna mutual coupling. Vertical bars depict 10 dB antenna bandwidth.

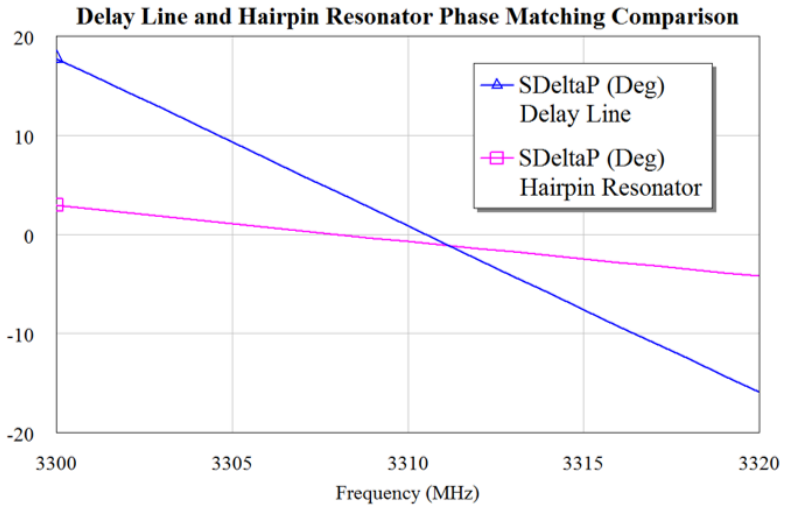

Figure 3.12: Phase differences between the antenna mutual coupling and the delay-line and hairpin filter phase cancellation structures.

The result is a scenario in which the filter bandwidth is decreased, degrading the magnitude response matching. Additionally, requiring a higher external quality factor increases the overall loss of the filter [86], requiring a higher coupling coefficient from the directional couplers. The overall result is a situation in which one must trade bandwidth response and Tx power output due to the increased coupling required in the directional couplers. For the substrate material chosen the line impedance must be increased and the coupling gap must be decreased to achieve higher coupling while simultaneously maintaining input matching. However, to ensure that the device could be fabricated the lower limit on the gap size was set at 200 μm. Therefore, a compromise solution was implemented resulting in the maximum achievable cancellation bandwidth for the choice of PCB material.

The simulated difference between the antenna mutual coupling phase and the phase matching of the delay-line circuit and the hairpin filter circuit is shown in Fig. 3.12. The differential phase between the hairpin filter and the mutual coupling response is within 3° over the 20 MHz bandwidth shown. The differential phase

between the delay-line and the mutual coupling is within 18° over the same bandwidth. Another advantage of the filter element over the delay-line is that the phase matching circuit can be compact. This is due to high group delay the filter element imposes at the resonant frequency of the antenna mutual coupling [58]. These effects demonstrate that phase matching using a filter element is superior to the delay-line implementation.

3.6 Circuit Implementation

The final circuit layout of the self-interference cancellation circuit is shown in this section. The final challenge in the implementation of the self-interference canceler lies in the layout of the PCB. Unfortunately, using the ideal dimensions of the proposed canceler, the antenna elements cannot be directly fed from the ports of the directional couplers. This is due to the $\lambda_0/2$ element spacing of the antenna elements, separated by a distance of 45.5 mm. Therefore, feedline sections must be incorporated which add additional phase delay to the mutual coupling signal.

In order to maintain the 180° phase difference between the cancellation signal and the self interference signal there are two signal paths to consider. Relative to their respective outputs from the first directional coupler and their recombination at the output of the second directional coupler we have for paths P_1 and P_2,

$$\begin{aligned} P_1 &= 2\theta_{feed} + \theta_{MC}, \\ P_2 &= 180^\circ + \theta_{CN} + 2\Delta\theta_{CN}. \end{aligned} \tag{3.13}$$

where θ_{feed}, θ_{MC}, θ_{CN}, and $\Delta\theta_{CN}$, are phase delays associated with the feedlines, mutual coupling, cancellation network, and an additional delay that can be added to the cancellation network. Since the desired phase difference between the final

(a) (b)

Figure 3.13: Final layout of the proposed antenna and self-interference cancellation circuits. (a) Delay-line circuit. (b) Hairpin filter circuit.

cancellation signals is odd multiples of 180°,

$$P_2 = P_1 - (2N + 1)180^\circ \tag{3.14}$$

for integer values of N. Because the phase cancellation structure has been designed so that $\theta_{MC} = \theta_{CN}$ it is found that:

$$\Delta\theta_{CN} = -(N + 1)180^\circ + \theta_{feed}. \tag{3.15}$$

Therefore, for a required length of antenna feed, the cancellation structure must be compensated with an additional delay line at the input and output of electrical length $\Delta\theta_{CN}$.

Two different configurations of the final cancellation circuitry were chosen for fabrication: the delay-line circuit and the hairpin filter circuit. These devices are shown in Fig. 3.13. The PCB layout of both devices is carried out using NI AWR Microwave Office. In order to accurately match the antenna characteristics calculated using ANSYS Electronics, the mutual coupling was extracted in Touchstone format to for allow co-simulation with the PCB design. Previous work has demonstrated that NI AWR Microwave office's AXIEM simulator is very accurate for the design

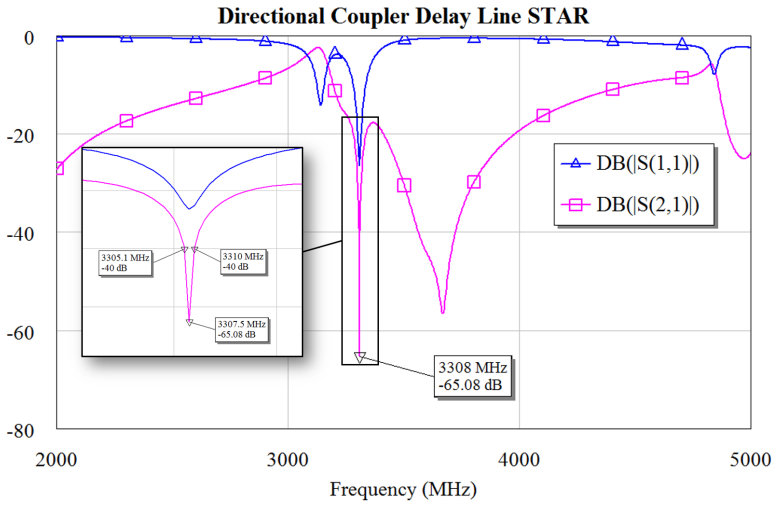

Figure 3.14: S-parameters of the resulting delay-line self interference cancellation circuit.

of planar circuits and filters [88].

The layout of the device is again carried out in the NI AWR Microwave Office circuit simulator, which allows the user to input microstrip lines as circuit elements. The circuit level devices are then simulated for the desired phase cancellation response. Finally, an extraction element is added to the circuit level simulation. The extraction element serves to link the circuit to the 3D planar EM simulator AXIEM, where the device is fully characterized. Any final adjustments that need to be made to the circuit are tuned using swept variables and the best resulting circuit is selected.

The S-parameters of the resulting configurations are shown in Figs. 3.14 and 3.15. The -40 dB mutual coupling bandwidth for the delay line and hairpin filters cancellation circuits are 4.9 MHz and 10 MHz, respectively. As predicted by the earlier work on phase matching, the bandwidth of the phase cancellation of the hairpin filter device is increased by over 100% compared to the delay-line implementation. For both circuits the input reflection coefficient is well below 20 dB and the center frequency remains at 3.31 GHz.

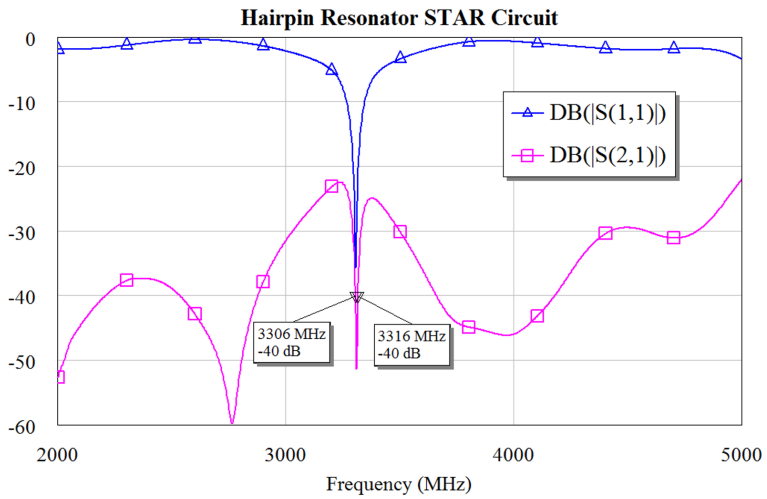

Figure 3.15: S-parameters of the resulting hairpin filter self interference cancellation circuit.

3.7 Fabrication and Measured Results

The devices from the previous section are fabricated on Rogers RO4350B using a multi-stage process. From the final design layout, DXF prototype layout files are generated. These files are then imported into Altium Designer, and the circuit-board layout, including the required grounding vias, are implemented. Gerber and NC Drill files are then exported from the resulting board layout. The Gerber files are imported into Pentalogix ViewMate software, and a lithographic mask for the top-copper layer is generated in portable document file format.

The physical processing begins by drilling the required vias using a T-TECH Quick Circuit QCJ5 circuit board plotter. Electroless and electro-plating processes are then used to deposit 17.5 μm of copper inside the vias between the top and bottom layers. A lithographic mask is then printed using an EPSON Artisan 1430 printer. A negative photoresist, Riston® TentMaster TM213i, from DuPont is used in the lithography process. After exposure to UV light the undesired copper is etched away, and the remaining photoresist is chemically removed. The resulting PCBs

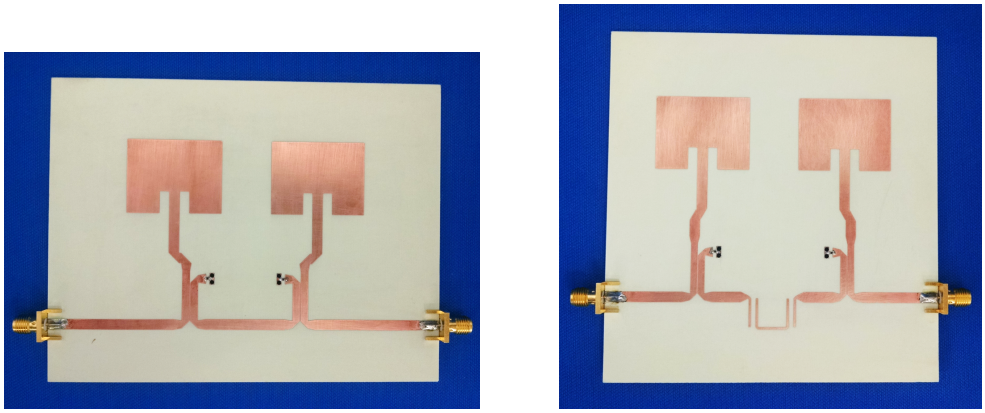

(a) (b)

Figure 3.16: Photographs of the two self-interference cancellation circuits. (a) Delay-line circuit. (b) Hairpin filter circuit.

are then cut out and edge mount connectors from Cinch Connectivity Solutions and 50 Ω surface-mount load resistors are soldered. Photographs of the resulting devices are shown in Fig. 3.16. The fabricated self-interference cancellation circuits were measured using a calibrated Agilent N5242A PNA-X network analyzer. The results are shown in Fig. 3.17.

The measured results for both fabricated devices agree well with simulated results. The cancellation bandwidth of both circuits is slightly shifted in frequency, +2 MHz for the delay-line implementation, and +22 MHz for the hairpin design. The hairpin resonator circuit was measured using a Nikon SMZ800 digital microscope. It was found that the coupling gap was over-etched by 70 μm and the resonator length was also decreased by 70 μm. These lengths were incorporated into the AWR design and simulated to determine the effect on the resonant frequency of the filter. The resulting simulation showed that the resonant frequency of the filter element was increased to 3.34 GHz. Therefore, over-etching during the lithography process is responsible for the shift in frequency of the hairpin filter STAR circuit.

The cancellation bandwidth of the fabricated devices also matches the simulated designs closely. The fabricated delay-line circuit has a -40 dB coupling bandwidth

of 4.2 MHz, compared to 4.9 MHz simulated. The hairpin filter self-interference cancellation circuit has 11.2 MHz of -40 dB bandwidth compared to the 10 MHz of simulated bandwidth. The 20 dB cancellation bandwidth relative to the original antenna mutual coupling for the delay line and hairpin filter implementations are 5 MHz and 14 MHz, respectively. The differences between the simulated and

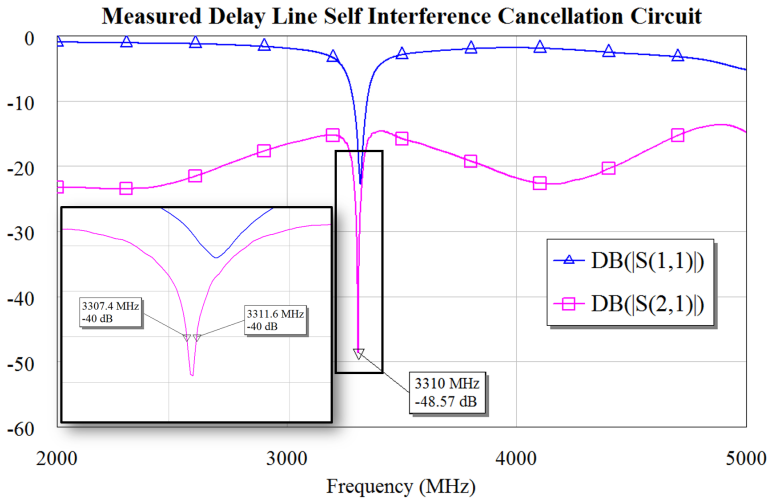

(a)

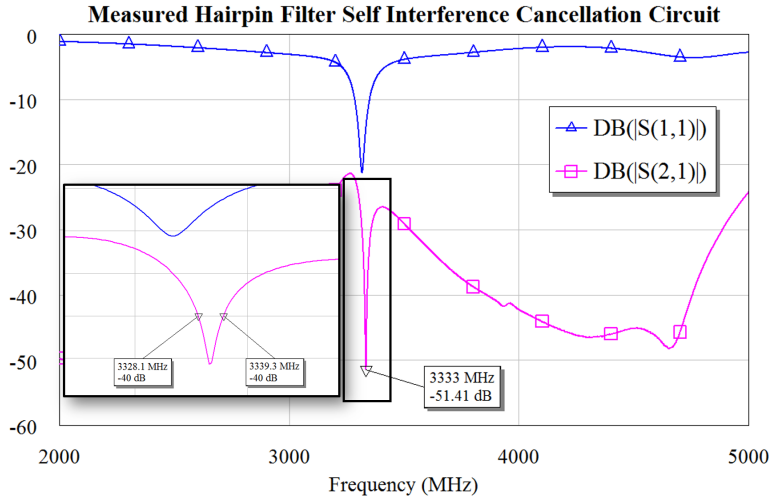

(b)

Figure 3.17: Measured S-parameters for the (a) delay-line and (b) hairpin filter self-interference cancellation circuits.

measured results are due to fabrication tolerances and the over-etching that was discussed previously.

By utilizing directional couplers to match the magnitude response of the mutual coupling the power loss between the Tx port and the antenna is minimized at -0.77 dB. In comparison to the delay-line circuit, the use of the hairpin resonator increases the -40 dB coupling bandwidth by 267%.

3.8 Alternative Configurations

Several alternative configurations that were later determined to be non-ideal for the implementation of the self-interference cancellation circuit were initially designed. These alternative implementations were based upon the assumption that the mutual coupling effect could be well characterized by a "lossy" transmission line model. The configuration of this circuit, and its response are shown in Figs. 3.18 and 3.19. The device shows a promising -50 dB bandwidth of 1.5 GHz, however, this is due to the linear phase response of the model. A second reason for the large cancellation bandwidth is the uniform magnitude response of the transmission line model used

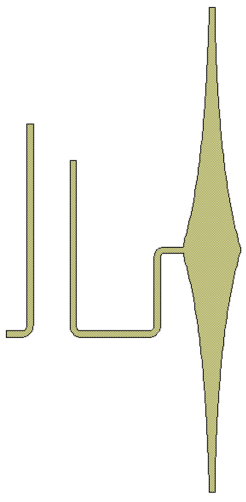

Figure 3.18: Layout of the alternative STAR structure.

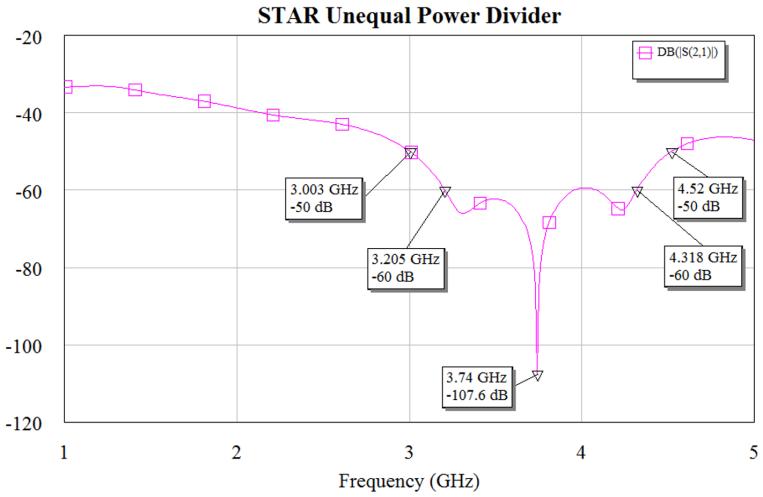

Figure 3.19: Tx to Rx isolation and input reflection coefficient of the circuit shown in Fig. 3.18.

for the antenna mutual coupling. The reason for its inclusion in this thesis, is that during the design of this cancellation circuit a new type of power dividing structure was implemented and utilized. The theory of this power dividing structure was developed, and will be shown in the following chapter of this thesis.

4 Exponential Power Divider

In microwave systems power dividers are one of the most common and important system elements. A typical way to realize such devices in planar form is through a microstrip T-junction. Although T-junctions are frequently utilized as equal power dividers, especially in antenna array design, they have also been investigated as unequal power dividers [89]. Different geometrical configurations of T-junctions been analyzed, such as T-junctions with asymmetrical transmission line impedances, and other stepped and tapered impedance configurations at the junction plane [89]. These structures have been analyzed utilizing various methods, like full-wave spectral domain analysis [90], waveguide models [91], equivalent circuit models [92], and through other computer modeling techniques [93], [94].

Previous work on asymmetrical power dividers with linearly tapered and stepped impedance lines relied on empirical models for their design procedure [89]. For instance, in [89], the power dividing ratio k is substituted into empirical expressions to solve for the other device parameters. Although this approach results in a working device, it does not give any physical insight into the device's operation. Purely computational methods have the same drawback.

In this thesis, using exponentially tapered line sections, an analytic approach for determining the device port parameters is developed. Exponentially tapered lines were chosen for their superior matching characteristics compared to linearly tapered lines [18]. By utilizing the impedance transformation in [95], a conventional design procedure for microwave circuits can be followed. It is shown that this method can be utilized to design asymmetrical T-junction power dividers with exponentially tapered lines with values of the power dividing ratio from 2 to 10 dB. Previous work has demonstrated power dividing ratios of up to 6 dB with this type of divider using linearly tapered line sections [89]. Devices with power dividing ratios of 7.6 dB and

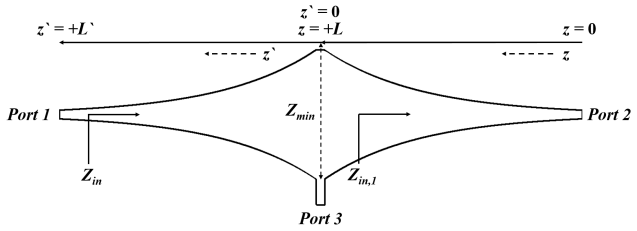

(a)

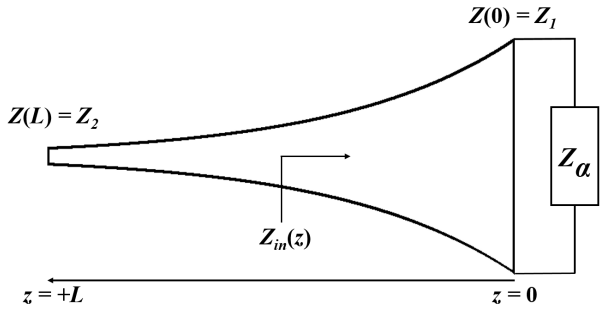

(b)

Figure 4.1: (a) Device layout of a planar exponential power divider. (b) Input impedance for exponentially tapered line.

9.3 dB are fabricated. These devices were fabricated and tested as elements in an early version of the STAR circuits shown in the previous chapter of this thesis. In addition, to the author's best knowledge, this device is the first power divider of this type capable of providing power dividing ratios of up to 10 dB.

4.1 Theory

The structure used in this work consists of two exponentially tapered transmission lines, shown in Fig. 4.1(a). The tapered sections are joined at the point where the characteristic impedance is the lowest, Z_{min}. All ports are terminated by the system characteristic impedance Z_0.

The device theory for the exponential power divider consists of two parts. First, the general impedance formulas for the line sections are given. Next, the input

reflection coefficients at all ports will be shown. The S-parameters of the device will then be derived from normal S-parameter relationships for symmetric, reciprocal devices. Finally, an analytic formula is provided for the power dividing ratio k.

4.1.1 Line Impedance Formulas

Since the lines for this power divider are exponentially tapered we can represent the impedance continuously along the section of line from 0 to L as shown in Fig. 4.1(a),

$$Z(z) = Z_0 e^{\alpha z}, \;\; \alpha = \frac{1}{L} \ln \left(\frac{Z_{min}}{Z_0} \right). \tag{4.1}$$

In addition, for the calculation of the input impedance we need an expression for the impedance from the symmetry plane to port 1, shown in Fig. 1(a). The impedance along the z' axis from 0 to L' is given by,

$$Z(z') = Z_{min} e^{\xi z'}, \;\; \xi = \frac{1}{L'} \ln \left(\frac{Z_0}{Z_{min}} \right). \tag{4.2}$$

4.1.2 Input Reflection Coefficient

From the impedance formulas given (4.1) and (4.2) the input reflection coefficients for each port of the exponential power divider can be derived. The input impedance looking into an exponentially tapered line is given by the solution to the nonlinear ordinary differential equation know as the Riccati equation [95]. The resulting expression for the input impedance for an exponential taper, Z_{in}, is [95]:

$$\frac{Z_{in}}{Z(L)} = \frac{Z_\alpha \left[\frac{1}{\lambda_g} - \frac{1}{\lambda_c} \tan\left(\frac{2\pi L}{\lambda_g} \right) \right] + j \frac{Z_1}{\lambda} \tan\left(\frac{2\pi L}{\lambda_g} \right)}{Z_1 \left[\frac{1}{\lambda_g} + \frac{1}{\lambda_c} \tan\left(\frac{2\pi L}{\lambda_g} \right) \right] + j \frac{Z_\alpha}{\lambda} \tan\left(\frac{2\pi L}{\lambda_g} \right)}. \tag{4.3}$$

$$\lambda_c = 4\pi L \ln\left(\frac{Z_1}{Z_2}\right), \quad \lambda_g = \frac{\lambda}{\sqrt{1-\left(\frac{\lambda}{\lambda_c}\right)^2}}$$

From Fig. 4.1(b) the parameter Z_α is the terminating impedance, Z_1 is the impedance of the exponential taper at $z = 0$, and Z_2 is the impedance of the taper at $z = L$. The procedure to calculate the input impedance of the device requires two consecutive impedance transformations using (4.3). First, the equivalent input impedance looking from the symmetry plane towards port 2 is calculated. From (4.1) it is found that $Z_\alpha = Z_1 = Z_0$ and $Z_2 = Z(L) = Z_{min}$. Substituting these values into (4.3) the first required input impedance $Z_{in,1}$ is known. Since this is the impedance seen from the symmetry plane the input reflection coefficient for port 3 can be calculated. The input impedance seen by port 3 is $Z_{in,1}||Z_{in,1} = Z_{in,1}/2$.

$$\Gamma_3(\lambda) = S_{33}(\lambda) = \frac{Z_{in,1} - 2Z_0}{Z_{in,1} + 2Z_0} \tag{4.4}$$

This impedance appears in parallel with the terminating impedance Z_0 at port 3, so the terminating impedance for the second transformation is $Z_\alpha = Z_0||Z_{in,1}$.

In order to calculate the overall input impedance seen by port 1 the transform given by (4.3) is used a second time. This time, however, (4.2) is used to calculate Z_{in}, λ_c, and λ_g. The values substituted into (4.3) for this transformation are, $Z_1 = Z_{min}$ and $Z_2 = Z(L) = Z_0$. Now that the structure's overall input impedance has been determined the input reflection coefficient is given by:

$$\Gamma_1(\lambda) = S_{11}(\lambda) = S_{22}(\lambda) = \frac{Z_{in} - Z_0}{Z_{in} + Z_0} \tag{4.5}$$

Finally, the remaining relevant port parameters are calculated. From symmetry, S_{11} = S_{22} and $S_{31} = S_{32}$. And from reciprocity, $S_{ij} = S_{ji}$ for $i \neq j$. From these

properties the following relationships are derived:

$$|S_{31}|^2 = \frac{1 - |S_{33}|^2}{2} \tag{4.6}$$

$$|S_{21}|^2 = \frac{1 + |S_{33}|^2}{2} - |S_{11}|^2 \tag{4.7}$$

Following the convention used in [89], k is defined as the power dividing ratio $|S_{21}|^2/|S_{31}|^2$.

$$k = \frac{|Z_{in} + Z_0|^2 \left[|Z_{in,1} + 2Z_0|^2 + |Z_{in,1} - 2Z_0|^2\right] - 2|Z_{in} - Z_0|^2 |Z_{in,1} + 2Z_0|^2}{|Z_{in} + Z_0|^2 \left[|Z_{in,1} + 2Z_0|^2 - |Z_{in,1} - 2Z_0|^2\right]} \tag{4.8}$$

A plot of computed values of k in dB for Z_{min} in the range of 5 to 40 Ω is shown in Fig. 4.2. This range of Z_{min} results in power dividing ratios between 2 and 10 dB.

In order to find the length L for the first minimum in $|S_{11}|$ L is set to be equal to $\lambda_g/2$. By choosing this value for L (4.3) becomes constant. Since the input impedance is constant, the derivative of S_{11} is zero and must be checked for whether it is maximal or minimal. It is found that,

$$S_{11}|_{L=\lambda_g/2} = -\frac{1}{1 + \frac{2Z_0}{Z_{min}}}, \tag{4.9}$$

is a minimum of S_{11}. Using (4.3) when $L = \lambda_g/2$ it is found that the first minimum in S_{11} occurs when,

$$L = \frac{\lambda_{min}}{2} \sqrt{1 + \left(\frac{1}{2\pi \ln\left(Z_0/Z_{min}\right)}\right)^2}. \tag{4.10}$$

This equation can be used to determine the minimum length of the exponentially tapered transmission lines for practical designs.

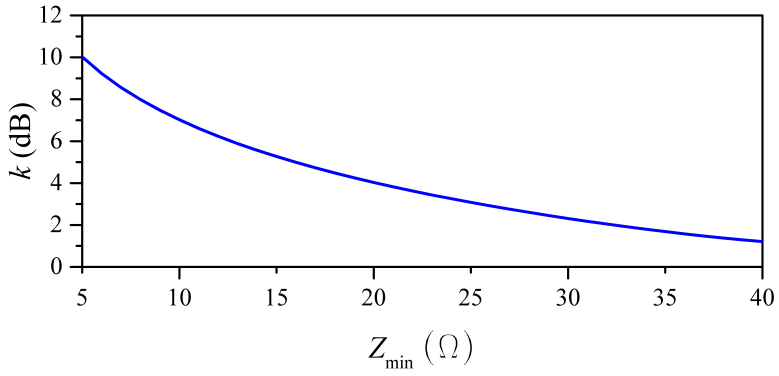

Figure 4.2: Power split value k versus the minimum impedance at the symmetry plane $Z_{min} \epsilon [5, 40]$ Ω.

4.2 Simulation and Measured Results

Two prototype devices, with power dividing ratios of 7.6 and 9.3 dB, were designed using the method presented. They were designed with these power dividing ratios for an early version of the STAR circuits shown in chapter 3. Both devices were fabricated on Rogers RO4350B substrate, with $h = 0.762$ mm, $\epsilon_r = 3.66$, and $\tan(\delta) = 0.0037$. Simulation was done using NI AWR Microwave Office's planar AXIEM simulator. Measurements of the fabricated devices were taken using a calibrated Agilent N5242A PNA-X network analyzer in a 3-port configuration.

The first prototype is designed to have the first $|S_{11}|$ minimum at 1.5 GHz. Using (4.8) and (4.10) the minimum impedance is 9 Ω and $L = 60$ mm. The second prototype is designed to have the first $|S_{11}|$ minimum at 1.7 GHz. This requires $Z_{min} = 5.65$ Ω and $L = 50$ mm. In Figs. 4.3 and 4.4 the theory, simulated, and measured S-parameters are shown. A photograph of the second prototype is shown in Fig. 4.5.

The results show that the designed power dividing ratios of 7.6 dB and 9.3 dB are obtained from 1.5 to 5 GHz and 1.75 to 3.5 GHz for the first and second prototype, respectively. In both cases the response in $|S_{21}|$ and $|S_{31}|$ match the

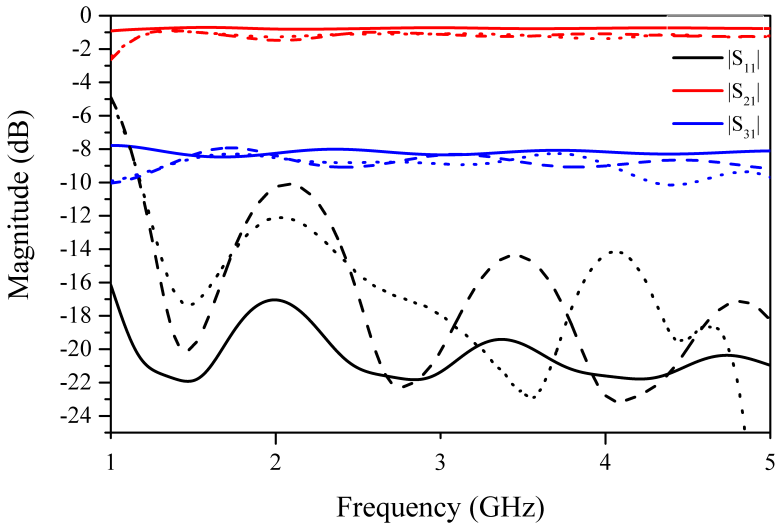

Figure 4.3: Theory, simulated, and measured S-parameters of the first prototype. Theoretical values shown are solid, simulated are dashed, measured are dotted.

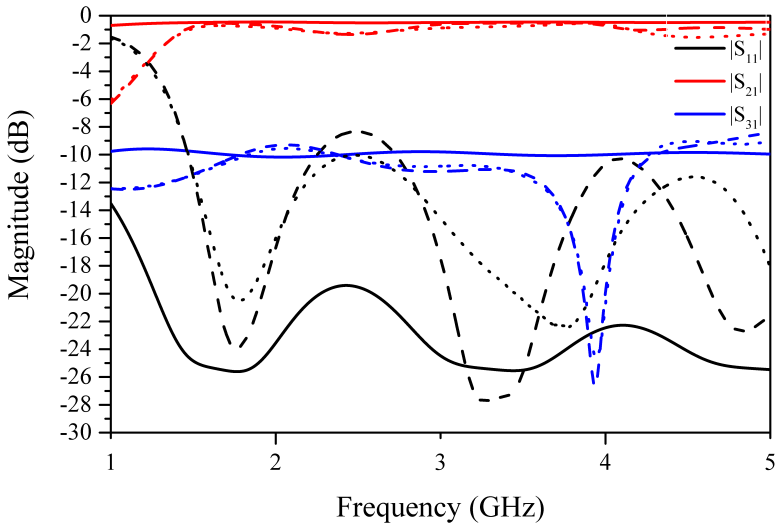

Figure 4.4: Theory, simulated, and measured S-parameters of the second prototype. Theoretical values are solid, simulated are dashed, measured are dotted.

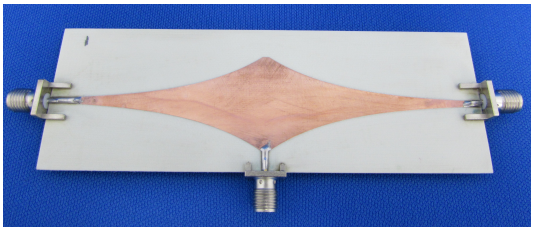

Figure 4.5: Photograph of the second prototype.

response predicted by theory. The RMS error in the power dividing ratio k for the first prototype is 0.62 dB between simulated and measured results. It is 0.63 dB between the theory and measurement. The second prototype has an RMS error in k between simulation and measurement of 0.32 dB. Between theory and measurement it is 0.83 dB. This prototype has a resonance in both the simulated and measured responses predicted by simulation at 3.9 GHz. The difference between the theory and measurement in $|S_{11}|$ is due to non-TEM modes propagating in the structure, and their reflections. This can be seen in full-wave simulation performed using ANSYS Electronics Desktop. Overall, these results demonstrate the validity of the mathematical model presented.

4.3 Summary

A mathematical formulation for calculating the S-parameters of an exponential power divider has been shown. From the general input impedance formula for an exponential taper an analytic expression for the power dividing ratio k is derived. Based on the presented method two devices were fabricated, with measured S-parameter values that are in good agreement with the power dividing ratios predicted. Both devices demonstrate power dividing ratios larger than what has previously been shown for this type of device.

This chapter concludes the discussion of passive microwave devices in this thesis. In chapter 3 passive microwave devices developed for phase cancellation

are developed. A result of earlier work on STAR resulted in the theory presented in this chapter. In the following chapter the the focus of this work turns to an adaptive receiver module. The LNA from this device is simulated and tested as part of a QPSK receiver system. The LNA is capable of both adaptive, and reconfigurable biasing modes of operation. It is shown how both of these modes of operation are beneficial in the QPSK system and the benefit they provide for DC power savings in large arrays.

5 Reconfigurable RF

Future systems are being developed for both wideband and multifunction capabilities. These systems will potentially be subjected to interference from multiple sources in a crowded electromagnetic spectrum. It is therefore necessary to determine the effects that out of band interference will have on systems designed for narrowband, wideband, and pulsed operation when wideband devices are used. This chapter details measurements taken on the dynamic adaptive receiver (DARE) [96]. The DARE performs as a wideband RF receiver element, with adaptive LNA biasing and gain capabilities. The testing conducted on this device is designed to measure the effect of adaptive LNA biasing in the presence of an out-of-band interfering signal.

The adaptive LNA biasing is controlled by an RF power detector based feedback control circuit. The bias current is adjusted so that the LNA remains in a linear mode of operation. Alternatively, this feature can be used to minimize the DC power consumed by the LNA, resulting in an overall reduction in DC power consumption. The overall reduction in power consumption depends on the power level of the RF signal received. For large arrays the integration of such a device would make a substantial impact on power supply requirements.

Due to the wideband operation of the DARE the possibility exists for out-of-band interference to limit the range of dynamic LNA biasing. The potential also exists that such interference could place the LNA into a nonlinear mode of operation, corrupting received signals. Therefore it is necessary to measure the device in a realistic mode of operation to determine how out-of-band interference will effect the overall system performance.

5.1 Dynamic Adaptive Receiver

The DARE is a differential device containing all of the required system components required for a receiver module [96]. This includes an LNA, mixer, and a variable gain amplifier (VGA) for the intermediate frequency stage. One signal that must be supplied off-chip is the local oscillator for the mixer. RF filtering of the Rx signal is also performed separately. The LNA and VGA respond adaptively to a varying power level stimulus or can be programmed directly through a digital interface. The LNA and mixer stages are wideband, with a frequency range of operation of 0.1–10 GHz. The intermediate frequency (IF) VGA operates with a flat frequency response over a bandwidth of 0 –2 GHz. The VGA gain can be set or can be allowed to run in an adaptive mode with set-points in 6 dB increments from 10 to 40 dB. The bias on the DARE LNA can also be reconfigured, or set to operate in an adaptive mode. The range of the LNA's gain is between 9 and 13 dB, depending on the bias setting. The fixed biases of the LNA range from 10 mA to 80 mA in nominal steps of 10 mA. The actual bias points for all of the nominal settings were measured and are shown in table 5.1. The LNA's noise figure is approximately 2.5 dB from 3–5 GHz according to DARE datasheet. More information about the DARE can be found in [96].

5.2 System Level Simulations

System simulations are carried out in NI AWR Microwave Office in order to anticipate the performance of the DARE LNA subject to out-of-band signals. QPSK transmitter and receiver subsystems were implemented, and both wideband out of band and single tone signals were delivered to an LNA modeled using performance metrics of the DARE at its highest bias point. The gain of the LNA model is set to 13 dB and the P1dB is set at 5 dBm. The noise figure for the LNA model is set at

Table 5.1: Nominal and measured values for DARE LNA current bias setpoints.

Nominal v. Acutal LNA Bias	
Nominal Current (mA)	**Measured Current (mA)**
10.00	9.97
20.00	19.58
30.00	29.24
40.00	38.50
50.00	56.83
60.00	65.55
70.00	74.50
80.00	82.71
Baseline	43.70

2.5 dB. This model is limited in that it doesn't capture the dynamic biasing capability of the DARE. However, it provides the opportunity to model the response of the LNA to higher power levels than would be desirable in a physical test. The test is designed to determine the error vector magnitude (EVM) characteristics of the LNA when average power levels exceed the LNA's P1dB.

QPSK communications systems transmit a signal in which combinations of the I and Q signals are assigned to one symbol. In the configuration used, each symbol contains two binary bits of information. This is best visualized by using a tool called a constellation diagram, shown in Fig. 5.1. The I and Q received signals are mapped to the complex plane as $I + jQ$, and the corresponding location is assigned to two bits. In the diagram shown the bits are gray coded, meaning only one bit changes when traveling 90°. From Fig. 5.1 the EVM (%) can be defined as,

$$\text{EVM}(\%) = \frac{|P_{Rx} - P_{Ref}|}{|P_{Ref}|} = \frac{\sqrt{(I_{Rx} - I_{Ref})^2 + (Q_{Rx} - Q_{Ref})^2}}{\sqrt{I_{Ref}^2 + Q_{Ref}^2}}, \tag{5.1}$$

where, I_{Ref}, I_{Rx}, Q_{Ref}, and Q_{Rx} are the in phase and quadrature components of the received power signals.

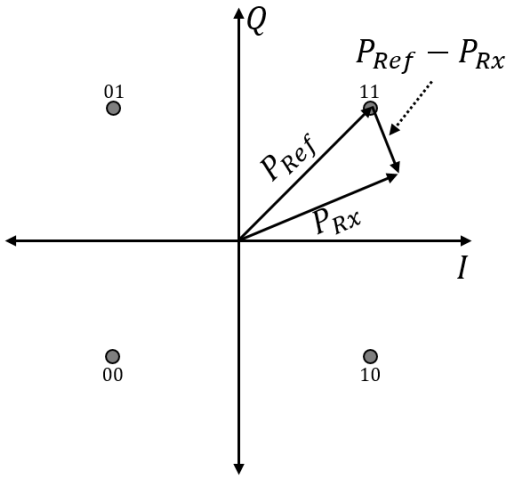

Figure 5.1: QPSK constellation diagram.

Since the EVM is subject to fluctuations in the receiver noise floor, it is more informative to look at an average of the EVM over N receive constellations.

$$\text{EVM}(\%) = \frac{\sqrt{\frac{1}{N}\sum_{n=1}^{N}(I_{Rx}[n] - I_{Ref})^2 + (Q_{Rx}[n] - Q_{Ref})^2}}{\sqrt{I_{Ref}^2 + Q_{Ref}^2}} \tag{5.2}$$

In this work the EVM is averaged over 1000 symbols.

The QPSK transmitter is set to transmit 0 dBm average power centered at 3.3 GHz with 20 MHz of bandwidth. An average Gaussian white noise system block is used to model the communications channel with 60 dB of channel loss and an average noise floor power level of approximately -85 dBm. A single-tone signal at 3.4 GHz, which will not mix with the desired QPSK baseband receive signal, is combined with the desired signal at the LNA. The spectrum of the single-tone signal and the QPSK modulated carrier at 3.4 GHz and the resulting average EVM for swept power levels of the single-tone signal are shown in Fig. 5.2.

The simulated result shows an EVM that exponentially increases with the input power of the interfering signal. This is verified using the MATLAB curve fitting tool.

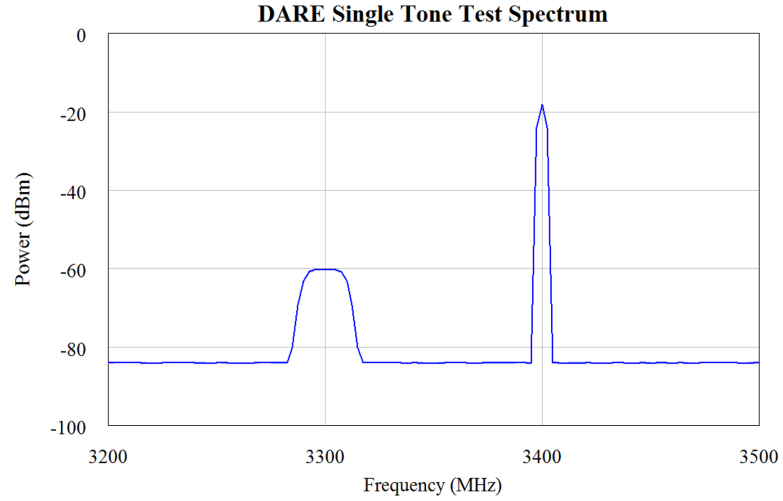

(a)

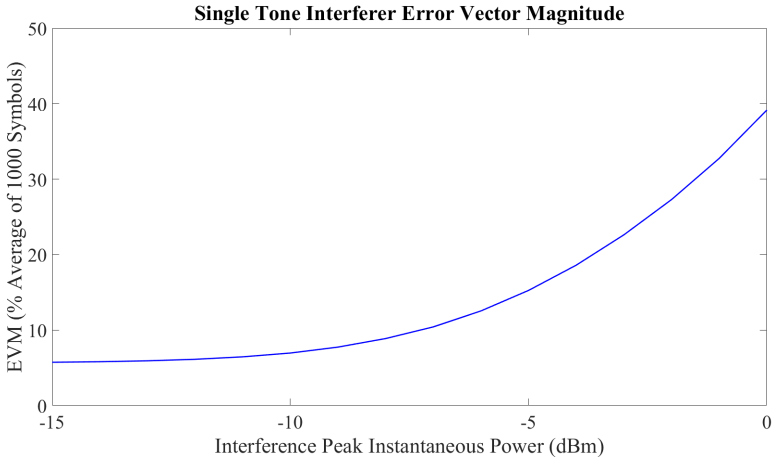

(b)

Figure 5.2: (a) Simulated power spectrum of the QPSK signal and the single-tone interferer. (b) EVM of the QPSK receiver v. instantaneous power level of the single-tone interferer.

The resulting exponential equation for the curve is,

$$\text{EVM}_{ST} = 38.33e^{0.171 \cdot P_{int}} \ (\%), \tag{5.3}$$

where P_{int} is the power of the interference signal from -15 to 0 dBm. The R^2 value for the fit is 0.99 with a root mean square error of 1.33%.

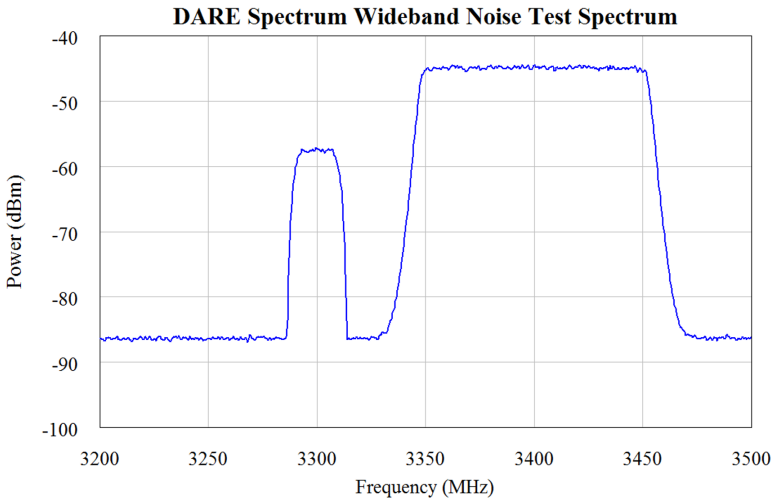

(a)

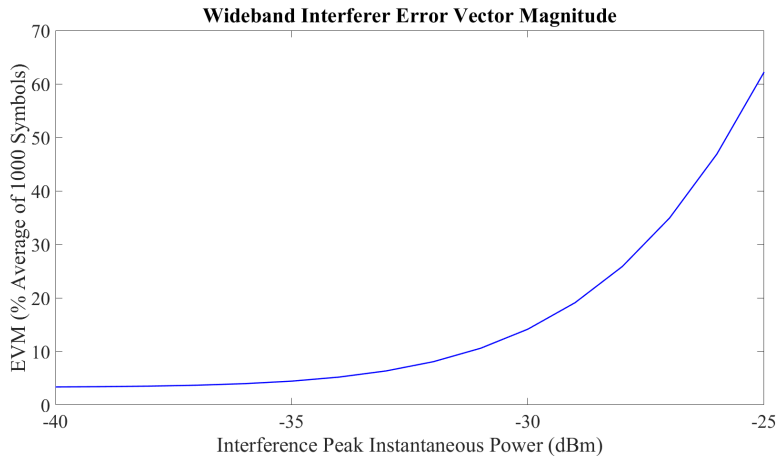

(b)

Figure 5.3: (a) Simulated power spectrum of the QPSK signal and wideband interferer. (b) EVM of the QPSK receiver v. instantaneous peak power level of the wideband interferer.

For the second test, a band-pass filtered Gaussian white noise source replaces the single-tone interferer. The center frequency for the band-pass filter is set to 3.4 GHz, with 3 dB bandwidth of 100 MHz. The power spectrum and the resulting EVM for the wide-band interfering signal are shown in Fig. 5.3.

The second set of EVM data is also an exponential function of P_{int} and can be

represented by the equation,

$$\text{EVM}_{WB} = 7.43 \times 10^4 e^{0.28 \cdot P_{int}} \ (\%), \tag{5.4}$$

where in this case the power P_{int} is the peak power spectral density of the wideband tone, between -40 and -25 dBm. For this plot the R^2 value is 0.99 and the root mean square error is 1.27%.

5.3 Balun Design and Fabrication

In order to interface with the DARE module two planar Marchand baluns were designed in NI AWR Microwave Office. The device design consists of a single open circuited feedline which is coupled to two high impedance short circuited quarter-wave transmission line sections. The phase difference between the signal coupled to the short circuited lines is 180°, transforming the unbalanced microstrip input signal into a balanced output [97]. Since high impedance lines are used to achieve maximum coupling to the balanced outputs, quarter-wave transformers are

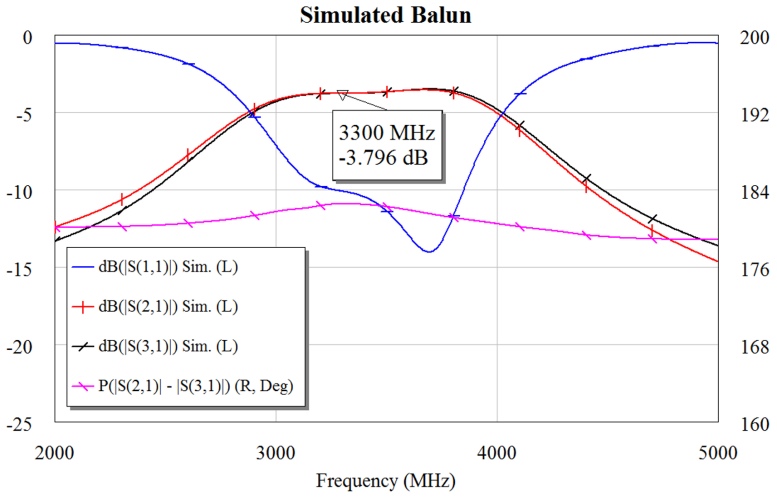

Figure 5.4: Simulated S-parameters of the Marchand balun.

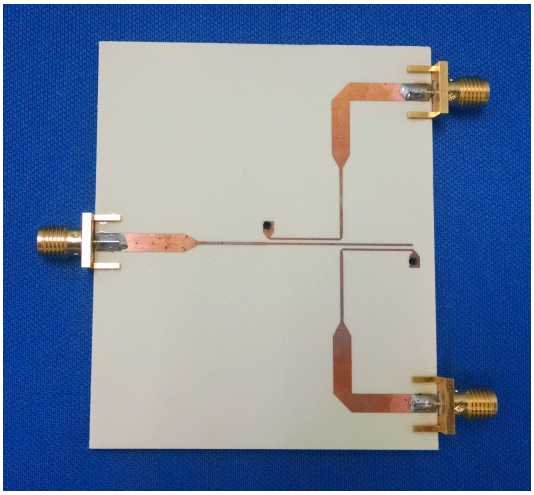

Figure 5.5: Photograph of the fabricated balun.

used to match the device ports to a characteristic impedance of 50 Ω [18].

The simulated unbalanced S-parameters and the differential phase between the balanced output ports is shown in Fig. 5.4. The simulated circuit shows a differential insertion loss of 0.8 dB, and a maximum magnitude imbalance between the differential ports of less than 0.1 dB. The differential phase between the two ports is less than 2.5°. The balun achieves the desired operating characteristics from 3–3.9 GHz.

Two baluns were fabricated in order to convert the unbalanced signals from the signal generators to the balanced LNA input of the DARE and to convert the balanced DARE output to an unbalanced signal for the input to the RTSA. The fabrication procedure used is the same process shown in chapter 3. The magnitude, and differential phase response of the fabricated baluns are shown in Fig. 5.6. The magnitude response for both baluns matches the simulated response over the desired band. The fabricated devices have a slight increase in insertion loss, 0.9 dB compared to 0.8 dB simulated. The measured differential phase between the balanced output ports is within 6° of 180° for the first balun, and 2.5° for the second.

On the first balun, the copper on one of the short circuit vias was etched during

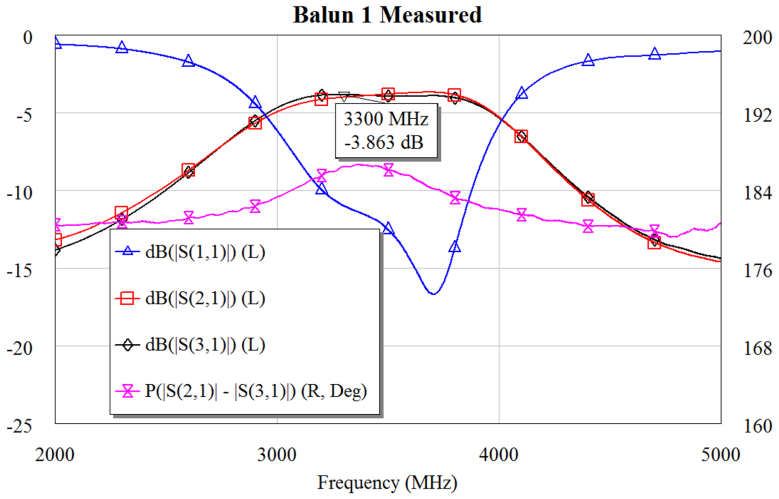

(a)

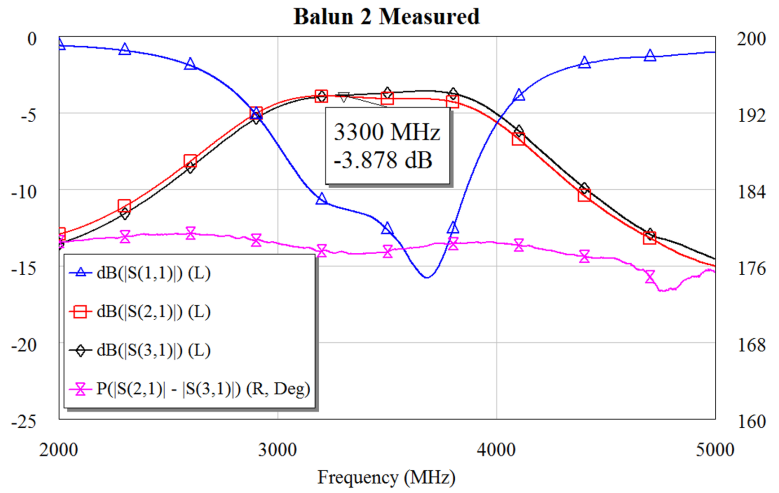

(b)

Figure 5.6: Measured responses of the Marchand-type microstrip baluns fabricated for DARE testing. (a) Balun-1. (b) Balun-2.

the lithography process. In order salvage the device the plating was replaced using 22 gauge wire and solder. The extra electrical length added by the solder is the source of the phase difference of 6° seen in the first balun.

5.4 QPSK Measurements

Two sets of measurements were conducted on the DARE in order to determine the effects of both single-tone and wideband interference. Both measurements were conducted using a Tektronix RSA6114A real-time spectrum analyzer, which also acts as a QPSK receiver. Three RF sources were used for the measurements. An Agilent E8276D vector signal generator was used to provide the QPSK modulated waveform. The QPSK center frequency is set to 3.3 GHz with a symbol rate of 20 Msps. A Vaunix Lab Brick LSG-602 signal generator was used to provide the single-tone interference. Finally, an Agilent E4428C analog signal generator was used to provide an 8 MHz frequency modulated (FM) interference source. Both interfering signals have a center frequency of 3.4 GHz.

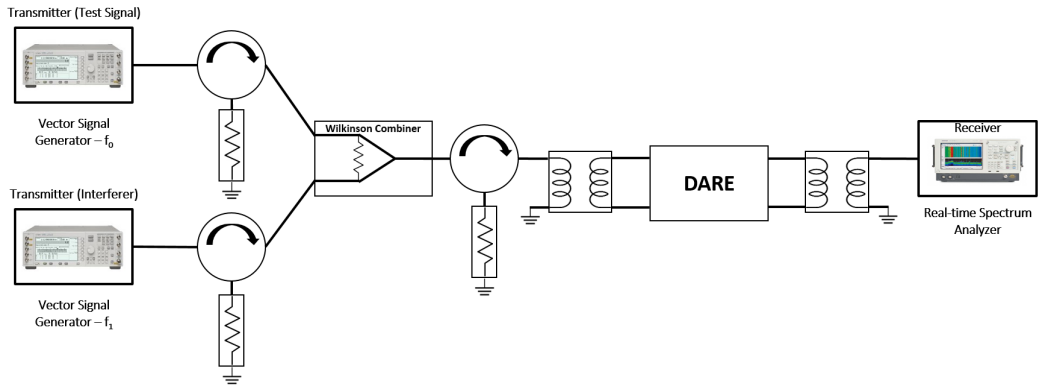

Figure 5.7: Block diagram of the proposed DARE test setup.

A block diagram of the test setup is shown in Fig. 5.7, and a photograph of the test setup is shown in Fig. 5.8. Other passive RF components required for the measurement include: one Wilkinson power combiner, four 2–5 GHz isolators, one 20 dB DC–6 GHz attenuator, and SMA cables. In order to obtain a 0 dBm interference signal at the DARE LNA the loss in the path between the generator and the DARE was characterized. This characterization was performed using an Agilent 5242A PNA-X network analyzer. The total differential path loss between the

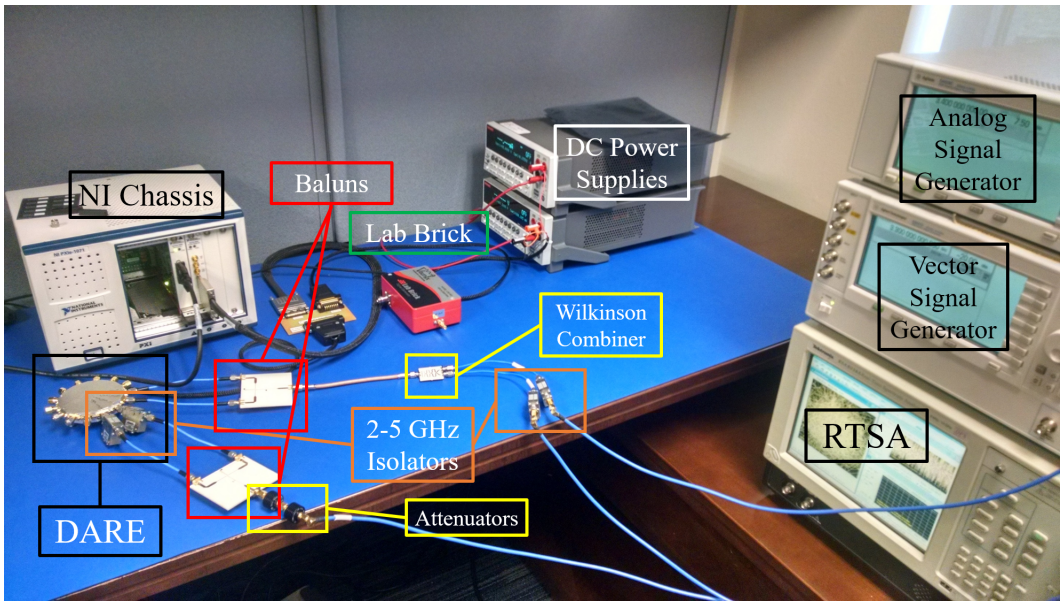

Figure 5.8: Laboratory test setup for the DARE QPSK testing.

generator and the DARE was calculated from the unbalanced S-parameters, shown in Fig. 5.9, and was found to be in the range of 6.2–6.5 dB for the QPSK waveform and the interference signal. The sources of loss are: 3.4 dB from the Wilkinson combiner, 0.1 dB from the RF isolators, 0.9 dB from the balun, and 2.1 dB from the SMA cables. Therefore, to inject a 0 dBm average power interference signal the generators are set to output 6.5 dBm.

In order to ensure that a safe power level is delivered to the RTSA, the components at the output of the DARE were also characterized for loss. It was found that the output signal path incurs 0.9 dB of loss from the balun, 0.1 dB from the isolators, 20 dB from the attenuator, and 0.5 dB from the SMA cables. The differential output attenuation is shown in Fig. 5.10, where additional attenuation is accounted for due to phase variations in the balun. After several test measurements were made it was found that the RTSA receiver would saturate when higher bias currents on the DARE module were used. The internal attenuator on the RTSA was then set to 10 dB which resolved the issue. The total attenuation from the output of LNA to the RTSA's

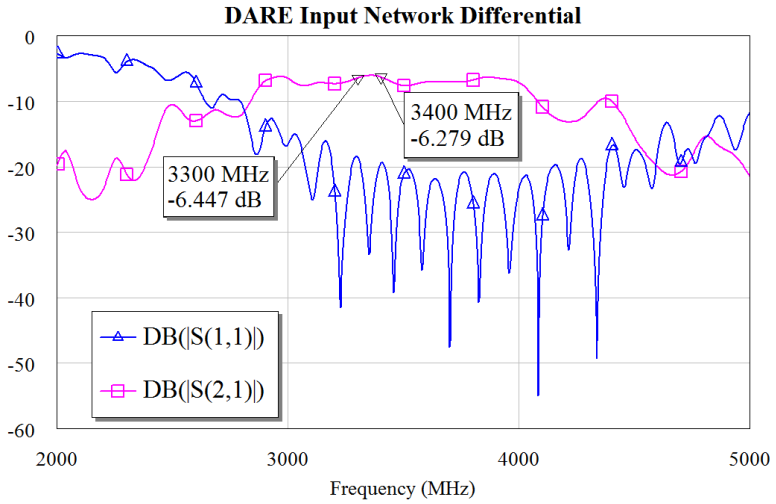

Figure 5.9: Characterization of the loss between the signal generators to the DARE module.

internal QPSK receiver is between 31.7 and 32.5 dB.

The average signal power for the QPSK waveform is set to -20 dBm, which translates to a peak power spectral density (PSD) of -64 dBm after passing through all RF stages between the transmitter and RTSA. This is a baseline measurement taken when the interference source is turned off. The baseline EVM at this bias setting is 8.8%. When the interfering tone is turned on the peak PSD drops to approximately -80 dBm, which is 5 dB above the noise-floor of the RTSA. This indicates that the DARE LNA is indeed in compression, and will produce a high EVM signal. This is an ideal setup for the subsequent measurements, since the effect of bias reconfiguration and the adaptive biasing mode will result in measurable EVM changes. Therefore, the -20 dBm QPSK signal provides a good baseline for determining the effects of the reconfigurable biasing and adaptive biasing capability of the DARE.

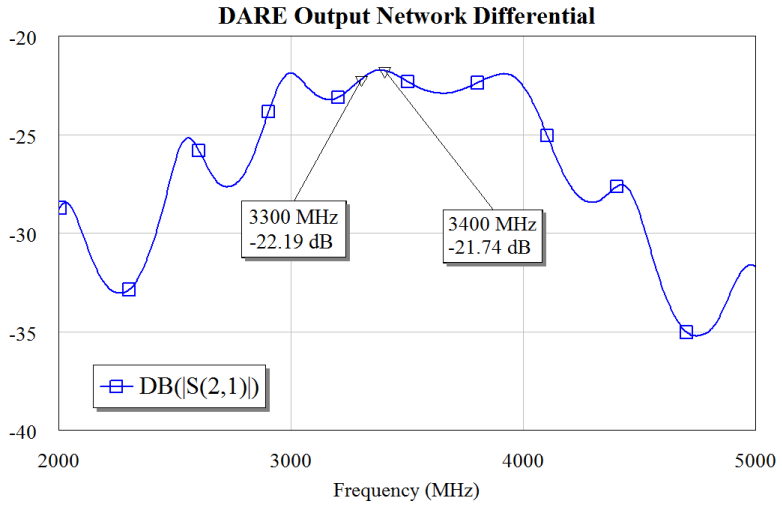

Figure 5.10: Characterization of the attenuation between the DARE output and the RTSA.

5.4.1 Single-tone Interference Test

For this test the DARE LNA is initially biased at 10 mA, the power level of the out-of-band interferer is set at 6.5 dBm so that the interference power input to the LNA is 0 dBm. At this bias point the LNA gain begins to compress and output power levels for both the QPSK waveform, and the interfering signal droop. The biasing on the LNA is then increased in steps of 10 mA, and measurements are taken with the adaptive biasing both disabled and enabled. These measurements include: EVM, peak QPSK PSD, SNR, and peak interferer PSD. The results from this test are shown in table 5.2. A plot of EVM as a function of the nominal bias current both with and without adaptive biasing enabled is shown in Fig. 5.11. Additional baseline measurements at all of the bias points without adaptive biasing or the interfering signal were also taken.

From the test results it is apparent that at the initial bias 10 mA bias the LNA gain is initially compressed leading to an EVM of 45.7%. As the LNA bias current is increased the EVM decreases. At bias currents above 60 mA there is no noticeable

Table 5.2: DARE QPSK receiver single tone interference test results for different LNA biasing conditions.

DARE QPSK Receiver Test w/ Single Tone Out of Band Interference				
Adaptive Biasing Disabled				
Bias (mA)	**EVM (RMS)**	**QPSK Peak (dBm)**	**SNR**	**ST Peak (dBm)**
10	45.70%	-80.3	4.7	-22.8
20	26.60%	-74.8	10.2	-17.4
30	18.50%	-71	14	-14.2
40	13.30%	-70	15	-12.2
50	7.50%	-66	19	-10.2
60	6.80%	-63.7	21.3	-10
70	6.60%	-62.6	22.4	-10
80	6.60%	-62	23	-10.1
Adaptive Biasing Enabled				
Bias (mA)	**EVM (RMS)**	**QPSK Peak (dBm)**	**SNR**	**ST Peak (dBm)**
10	32.50%	-77.60	7.40	-19.6
20	21.60%	-73.70	11.30	-15.6
30	15.60%	-71.80	13.20	-13
40	11.60%	-67.10	17.90	-11.4
50	7.00%	-64.70	20.30	-10.1
60	6.80%	-63.00	22.00	-10
70	6.80%	-63.40	21.60	-10
80	6.80%	-61.80	23.20	-10.1
Baseline Measurements				
Bias (mA)	**EVM Baseline (RMS)**	**QPSK Baseline (dBm)**		
10	8.80%	-64.1		
20	6.90%	-63.87		
30	6.30%	-63.6		
40	6.20%	-60.8		
50	6.00%	-59.8		
60	6.10%	-59.9		
70	5.80%	-59.3		
80	5.80%	-59.4		

improvement in the measured EVM.

The adaptive LNA biasing does not range between the minimum and maximum bias points of the LNA as originally expected. Instead, this feature biases the LNA at an intermediate state between the current bias point and the next set bias point. Additional current in the range of 0–5 mA is added in response to the detected power.

Measurements with this feature enabled show that in response to the out of band interferer, this feature does improve the EVM for each specific bias state. The adaptive biasing essentially achieves the same EVM with 5 mA less current required

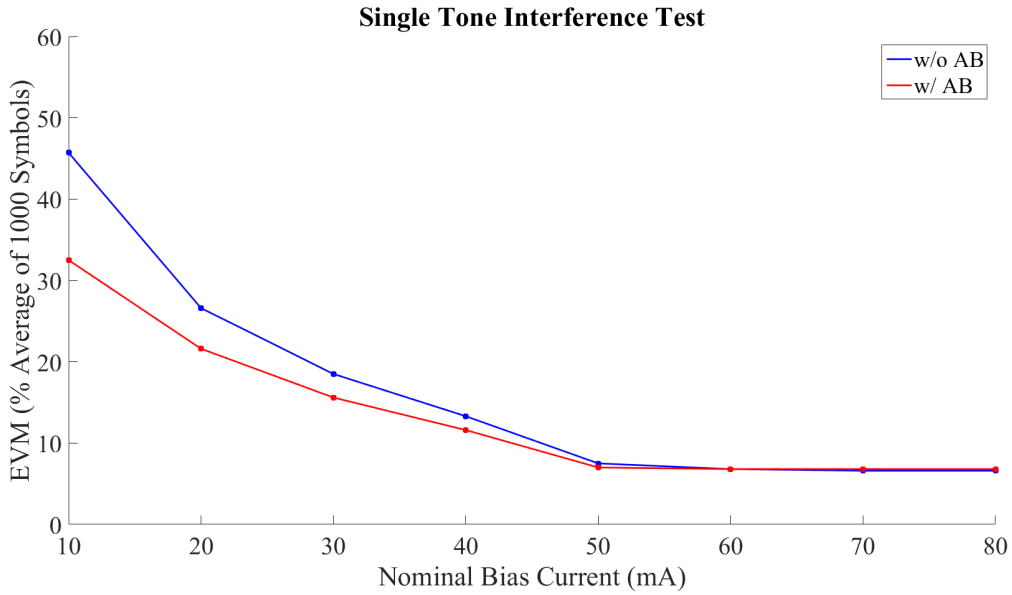

Figure 5.11: Measured EVM of the DARE module with and without adaptive biasing enabled for the single tone test.

by the next fixed setpoint. With 55 mA of current consumption, the adaptive biasing feature achieves the same EVM that the fixed biasing achieves at 60 mA. This feature is the most beneficial at the lowest bias settings, improving the EVM at 10 mA from 45.7% to 32.5% and at 20 mA bias from 26.6% to 21.6%.

5.4.2 Wideband Interference Test

For this test an FM waveform is generated using the Agilent E4428C analog signal generator. The maximum modulated bandwidth for this signal generator is 8 MHz centered at 3.4 GHz. The test procedure is the same as described for the single-tone interferer. The results from this test are shown in table 5.3 and a plot of EVM for the different nominal bias conditions is shown in Fig. 5.12.

Graphs of the spectrum measured using the RTSA for the single tone and wideband interference tests can be found at the back of this chapter. These graphs show spectra for 10, 40, and 80 mA biasing conditions both with and without adaptive

Table 5.3: DARE QPSK receiver wideband interference test results for different LNA biasing conditions.

DARE QPSK Receiver Test w/ FM Out of Band Interference				
Adaptive Biasing Disabled				
Bias (mA)	**EVM (RMS)**	**QPSK Peak (dBm)**	**SNR**	**FM Peak (dBm)**
10	53.54%	-80.67	4.33	-41
20	26.70%	-75.6	9.4	-35.6
30	18.10%	-72.5	12.5	-32.6
40	13.50%	-68.2	16.8	-30.5
50	7.80%	-65.07	19.93	-28.3
60	6.90%	-62.1	22.9	-28
70	6.90%	-60.3	24.7	-28.1
80	6.70%	-61.8	23.2	-28.1
Adaptive Biasing Enabled				
Bias (mA)	**EVM (RMS)**	**QPSK Peak (dBm)**	**SNR**	**FM Peak (dBm)**
10	33.10%	-76.80	8.20	-37.9
20	22.60%	-73.50	11.50	-34
30	16.00%	-71.80	13.20	-31.5
40	12.10%	-70.00	15.00	-29.7
50	7.40%	-64.70	20.30	-28.2
60	6.80%	-64.30	20.70	-28
70	6.70%	-64.10	20.90	-28.1
80	6.70%	-62.10	22.90	-28.2

biasing enabled. They are shown in Figs. 5.14 through 5.19. Constellation diagrams of the same measurements can be found in Figs. 5.20 and 5.21.

5.4.3 QPSK Conclusions

The testing of both single tone and FM interference reveals several beneficial aspects of the DARE. It also reveals the drawbacks of wideband devices that can pass large portions of spectrum. The results show that the DARE is able to compensate for the interfering signal, and effectively re-establish a favorable SNR in this test setup. It is able to do so by switching between fixed bias points, and to a lesser extent through the adaptive biasing feature.

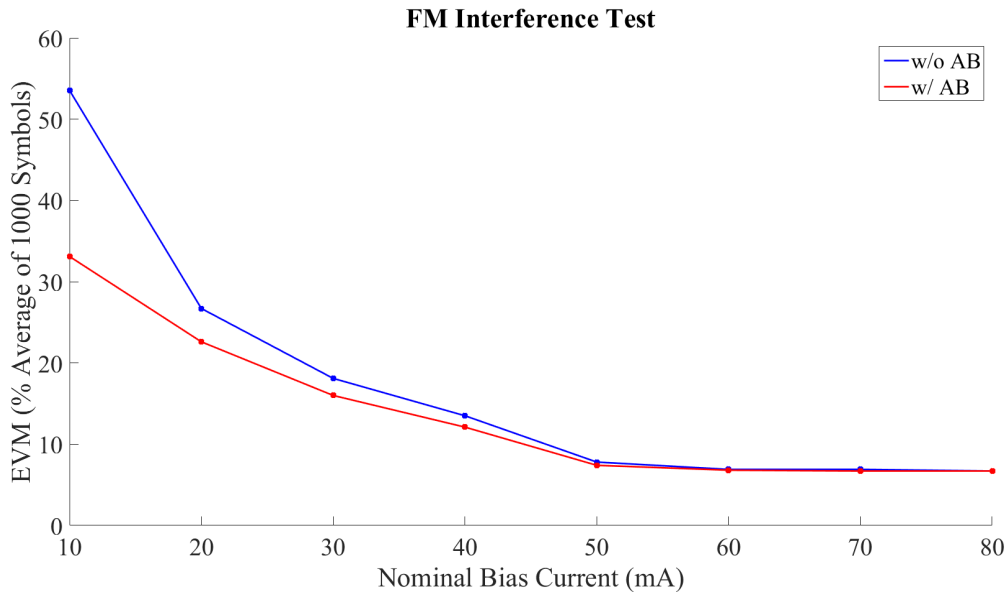

Figure 5.12: Measured EVM of the DARE module with and without adaptive biasing enabled for the wideband interference test.

In both simulation and measurement it was shown that the LNA will become compressed in the presence of interference. In the simulation this condition was created by increasing the average power of the interference signals. In measurement, the LNA is initially compressed, but is able to recover due to the increase in the LNA P1dB with increased bias current. Therefore, simulating an increase in the average interferer signal power with fixed P1dB results in a good approximation for the measured LNA behavior when the P1dB is varied and the interference signal power is fixed.

The test results for the single-tone interferer and the FM interference signal are very similar. This result implies that the DARE responds to the average signal power. This also means that the DARE can easily become saturated by the various signals crowding the electromagnetic spectrum. Fortunately, this can be compensated for by using tunable or reconfigurable filters, or a bank of fixed filters. A second solution would be to use a tunable or reconfigurable antenna element.

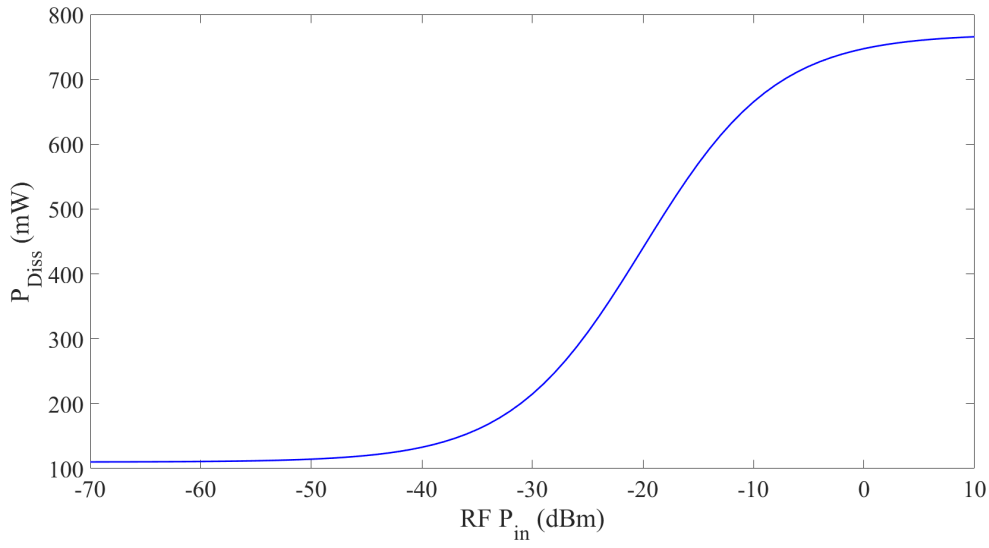

Figure 5.13: Dynamic power consumption of the DARE vs. RF input power with a fixed 5 V bias.

5.5 Radar System Impact

The largest improvement offered by the DARE module in a radar system would be its impact on dynamic array power consumption. Due to the large number of elements required to achieve desired beamwidths in phased array radar systems, even a small amount of power saving in the LNA can have a large system impact. This is especially true for arrays with dedicated transceiver modules at every element. For example, in a hypothetical 50x50 planar array, there are 2500 LNAs in the entire array. We can calculate the array level power savings for the number of elements supplied, relative to fixed-bias LNAs by,

$$\begin{aligned} P_{Fixed} &= V_{supply} I_{supply}, \\ P_{Adaptive} &= V_{supply} I_{adaptive}. \end{aligned} \tag{5.5}$$

For the DARE module the supply bias is a function of the RF input power.

The relative power consumption over a number of individual range bins can be determined therefore be determined. A general formula for the average power consumption over N equally spaced receive power levels is given by,

$$P_{avg} = \frac{1}{N}\sum_{n=1}^{N} V_{supply} I_{adaptive}\left(\left\{\frac{P_{min} - P_{max}}{N}\right\} n\right). \tag{5.6}$$

An approximation of the curve for the adaptive bias current versus the input power extracted from [96] is,

$$I_{adaptive} = 88 + 66\tanh\left(0.083 P_{in} + 1.67\right)\ (mA). \tag{5.7}$$

where P_{in} is in dBm. Power consumption of the LNA based on (5.7) with a 5 V fixed voltage bias is shown in Fig. 5.13.

The average power consumption of the adaptive LNA over eight receive windows from -70 dBm to 0 dBm is 317 mW. The same LNA operating with its bias fixed at the maximum current consumes 780 mW. The adaptive LNA biasing results in a DC power consumption reduction of 59.4 % over the fixed bias LNA. In the 2500 element array mentioned previously this would result in a total average power consumption of 792.5 W compared to 1950 W for the fixed bias LNAs. These results clearly show the benefit of the adaptive LNA in terms of average DC power consumption.

A possible negative impact of the DARE on radar operation is that the adaptive biasing could corrupt pulse-to-pulse receive information. Since the gain of the DARE is tied to its biasing state, and can also be adjusted by the adaptive biasing feature, clutter suppression could be severely impacted. One possible scenario in which this could occur is with a pulsed interferer, which could potentially cause the DARE's adaptive biasing to ramp up and down continuously. Future testing on the LNA will be designed to determine how detrimental this type of interference will be.

Spectral Graphs and Constellation Diagrams

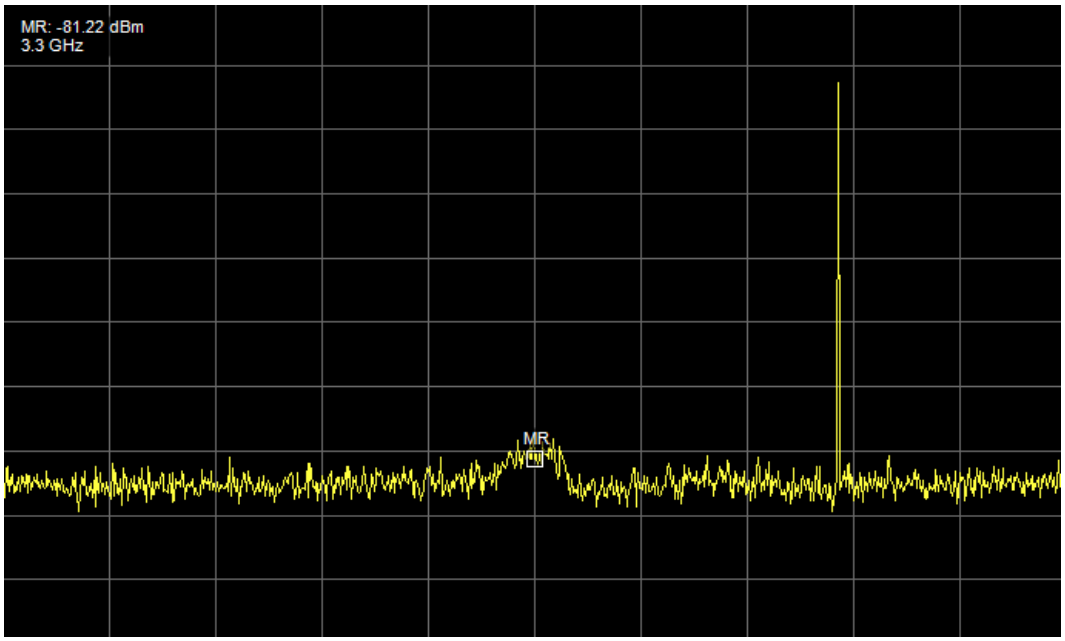

(a)

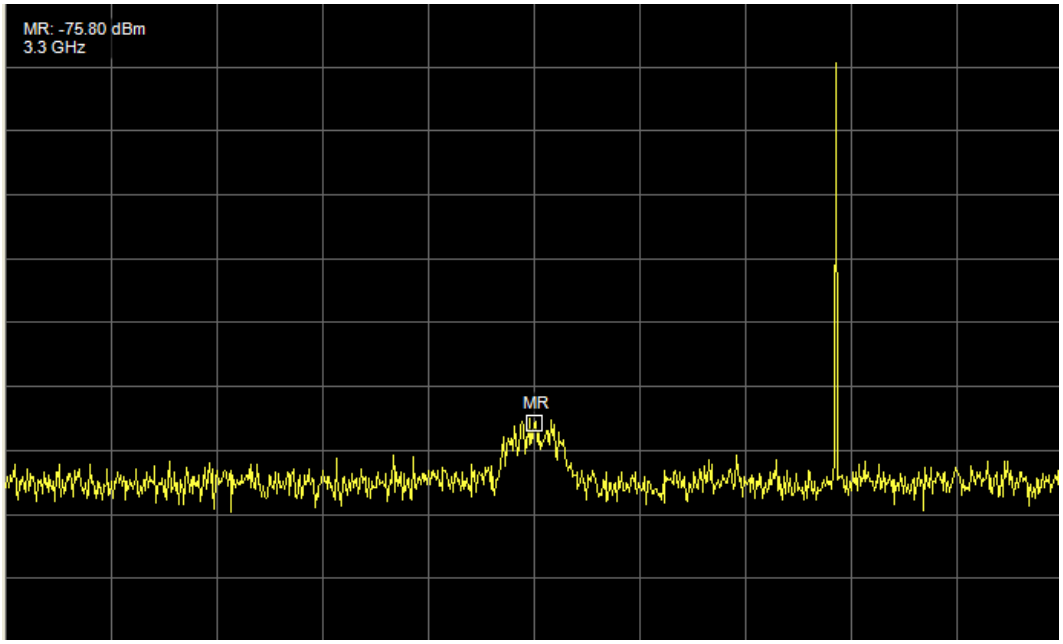

(b)

Figure 5.14: Spectra of the single-tone interference test at 10 mA nominal bias current. (a) No adaptive biasing – SNR = 4.7 dB, EVM = 45.7%. (b) With adaptive biasing – SNR = 7.4 dB, EVM = 32.5%.

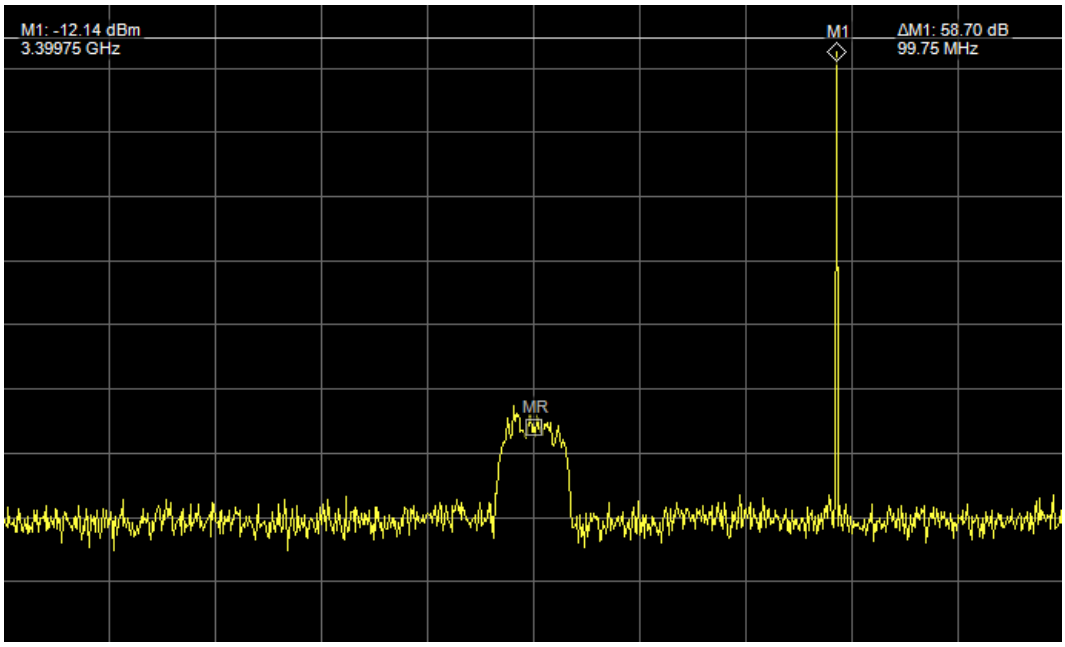

(a)

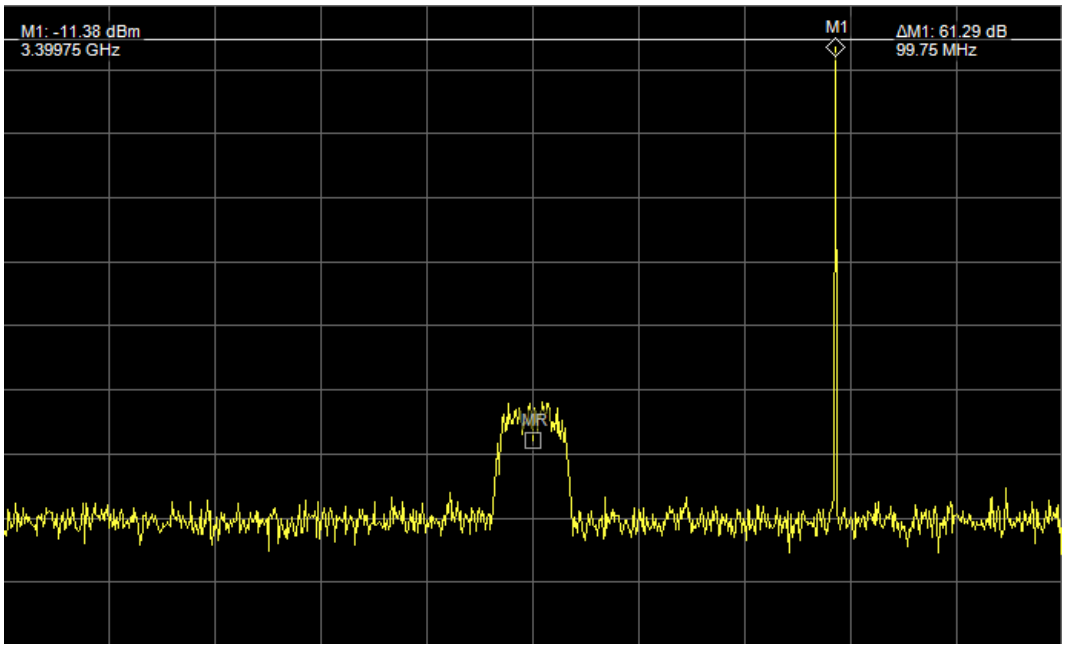

(b)

Figure 5.15: Spectra of the single-tone interference test at 40 mA nominal bias current. (a) No adaptive biasing – SNR = 15 dB, EVM = 13.3%. (b) With adaptive biasing – SNR = 17.9 dB, EVM = 11.6%.

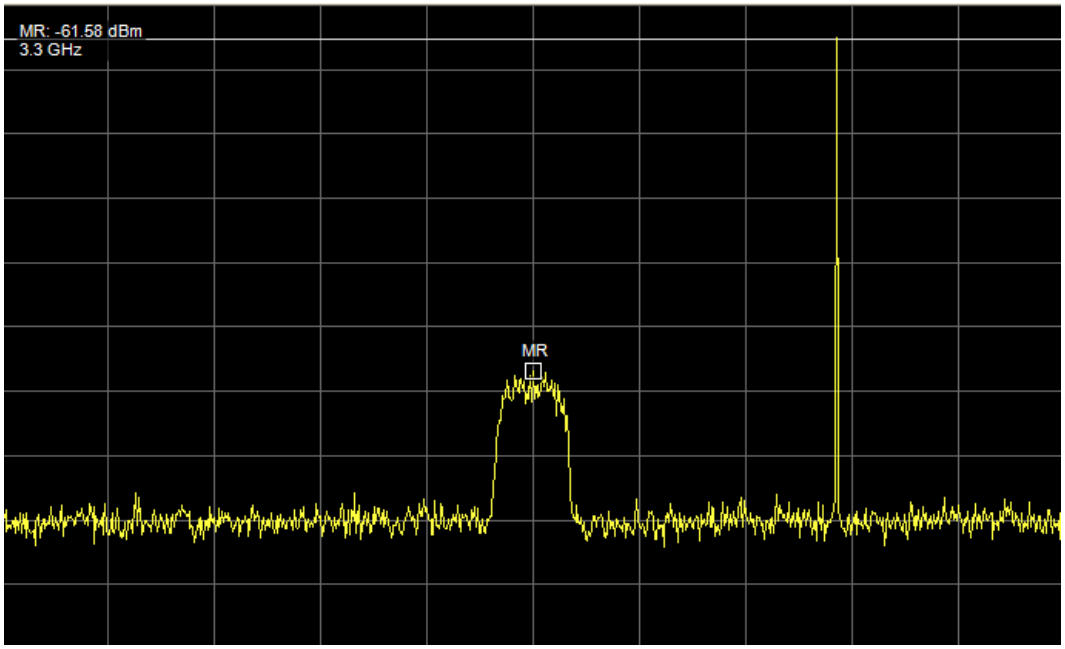

(a)

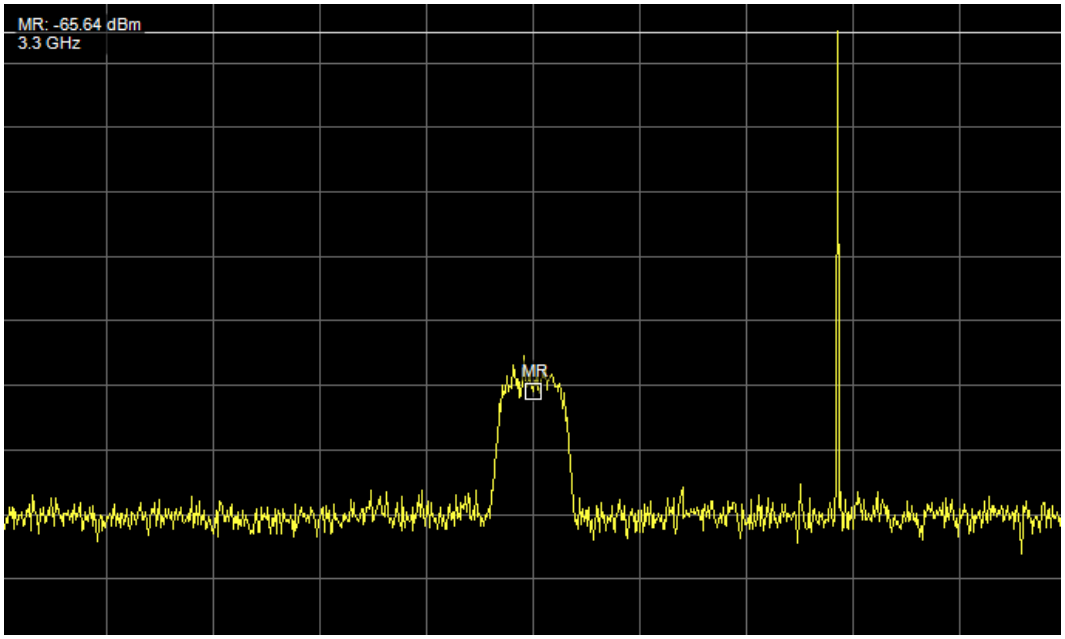

(b)

Figure 5.16: Spectra of the single-tone interference test at 80 mA nominal bias current. (a) No adaptive biasing – SNR = 23 dB, EVM = 6.6%. (b) With adaptive biasing – SNR = 23.2 dB, EVM = 6.8%.

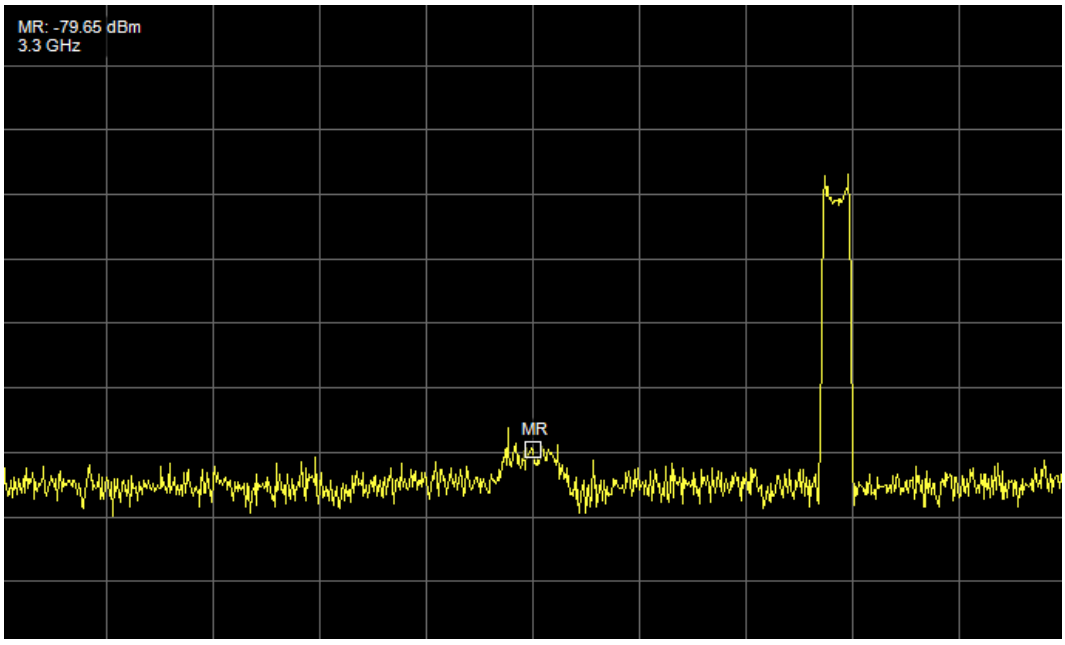

(a)

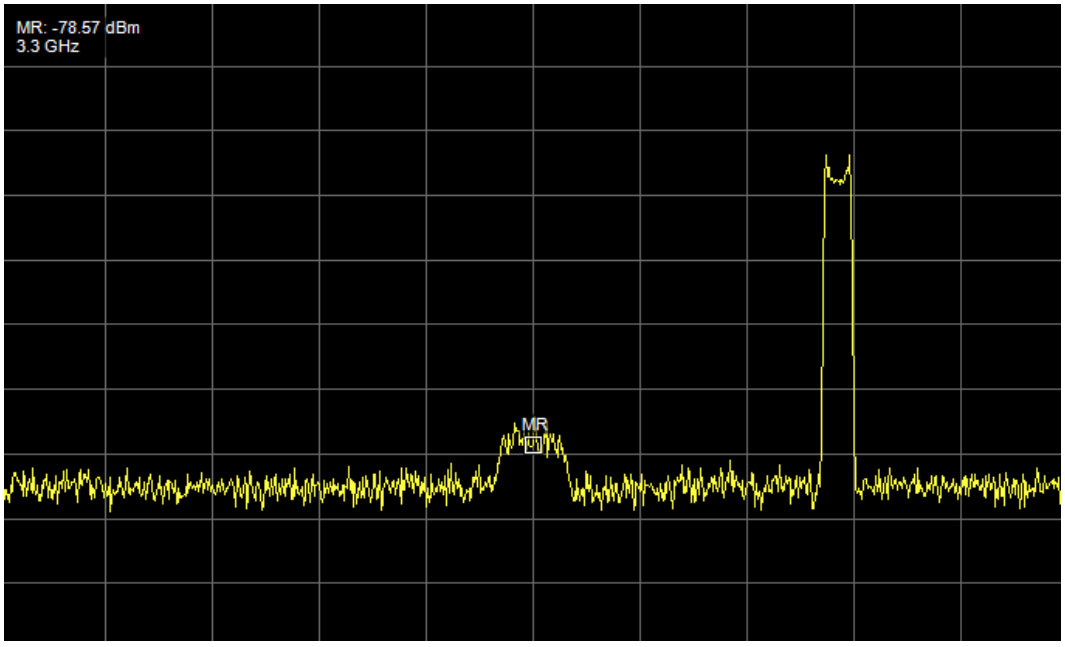

(b)

Figure 5.17: Spectra of the wideband interference test at 10 mA nominal bias current. (a) No adaptive biasing – SNR = 4.33 dB, EVM = 53.5%. (b) With adaptive biasing – SNR = 8.2 dB, EVM = 33.1%.

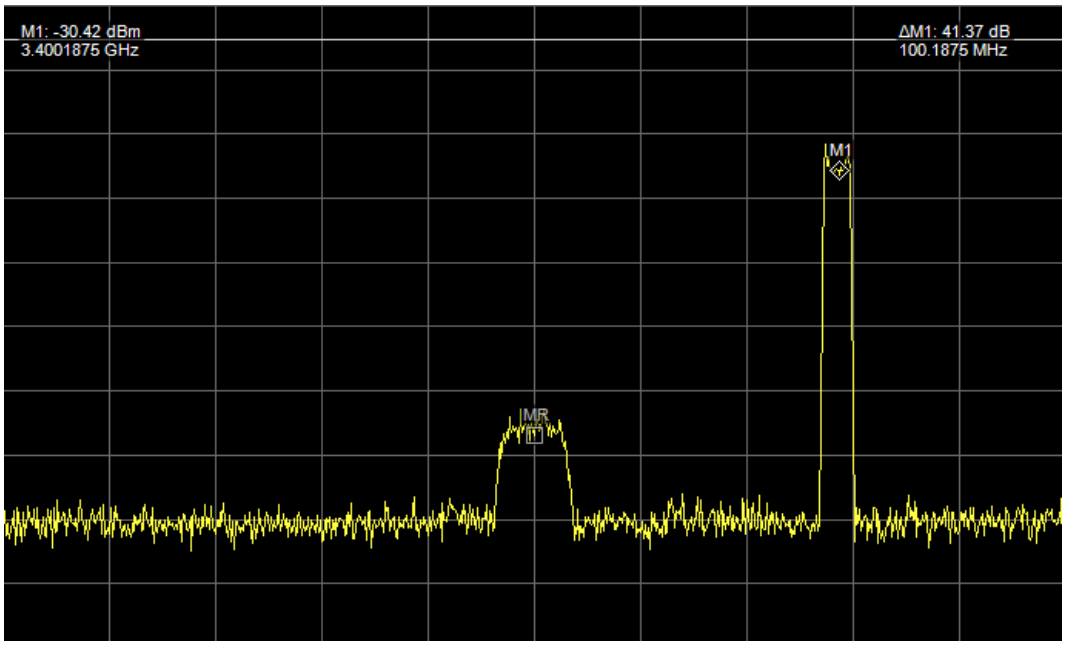

(a)

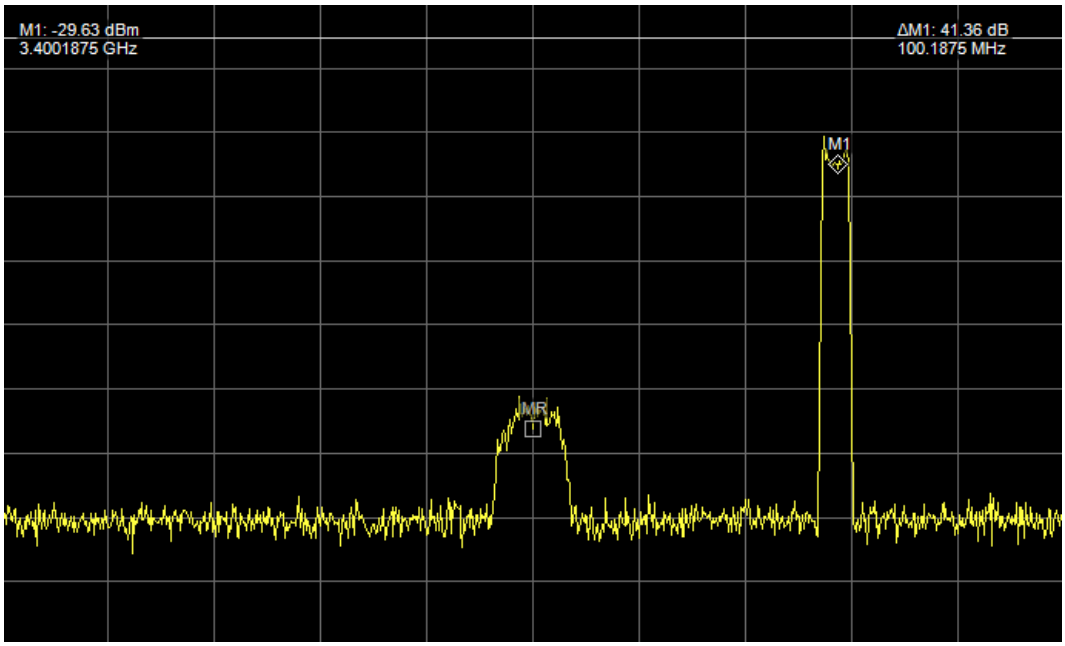

(b)

Figure 5.18: Spectra of the wideband interference test at 40 mA nominal bias current. (a) No adaptive biasing – SNR = 16.8 dB, EVM = 13.5%. (b) With adaptive biasing – SNR = 15 dB, EVM = 12.1%.

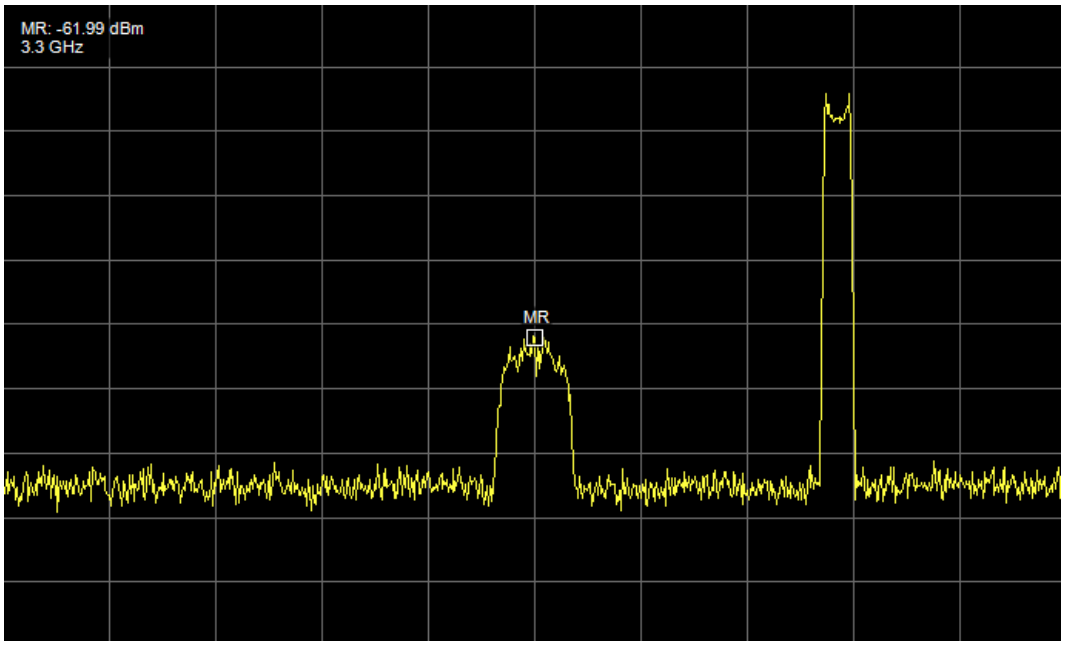

(a)

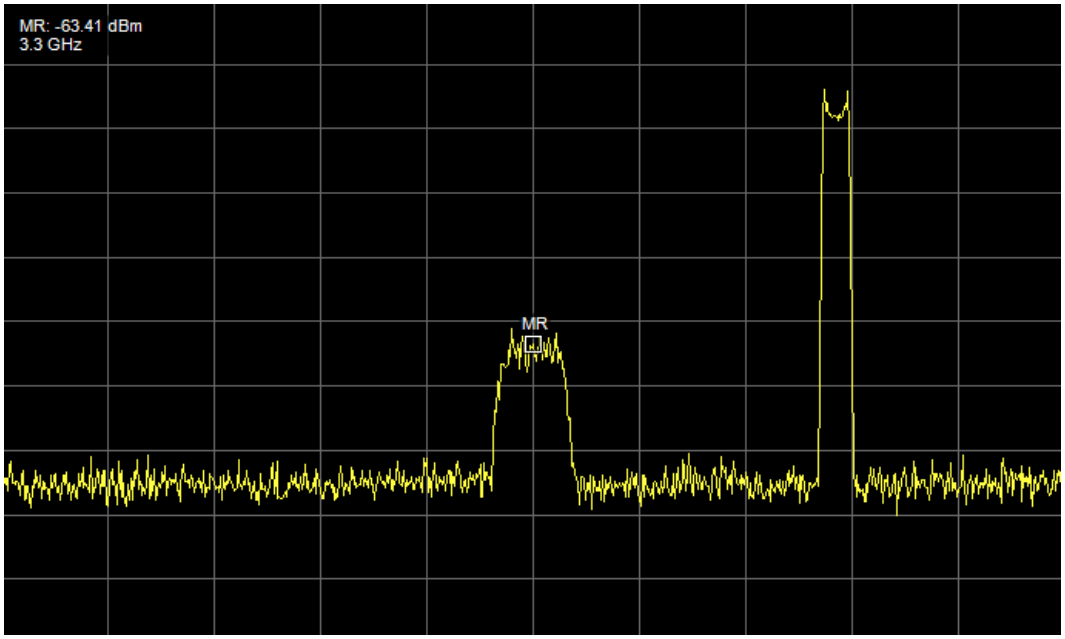

(b)

Figure 5.19: Spectra of the wideband interference test at 80 mA nominal bias current. (a) No adaptive biasing – SNR = 23.2 dB, EVM = 6.7%. (b) With adaptive biasing – SNR = 22.9 dB, EVM = 6.7%.

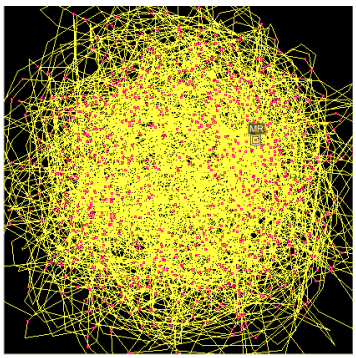

(a) 10 mA, no adaptive biasing. SNR = 4.7 dB, EVM = 45.7%.

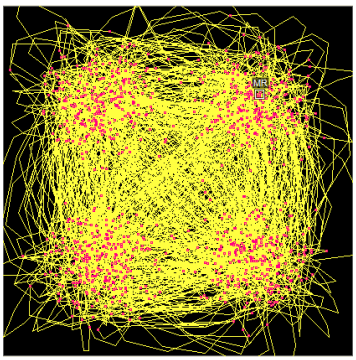

(b) 10 mA, with adaptive biasing. SNR = 7.4 dB, EVM = 32.5%.

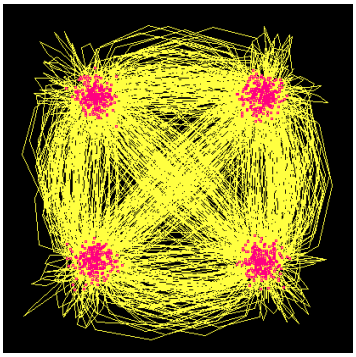

(c) 40 mA, no adaptive biasing. SNR = 15 dB, EVM = 13.3%.

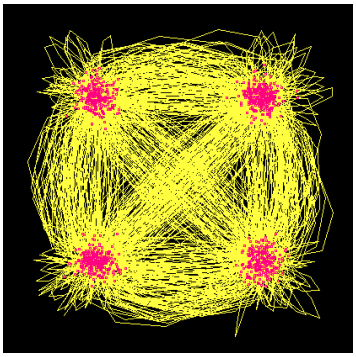

(d) 40 mA, with adaptive biasing. SNR = 17.9 dB, EVM = 11.6%.

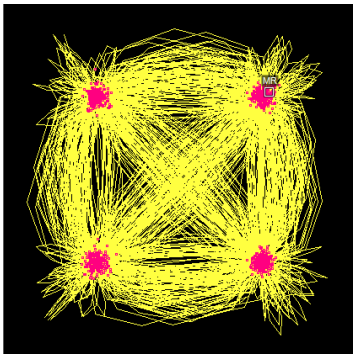

(e) 80 mA, no adaptive biasing. SNR = 23 dB, EVM = 6.6%.

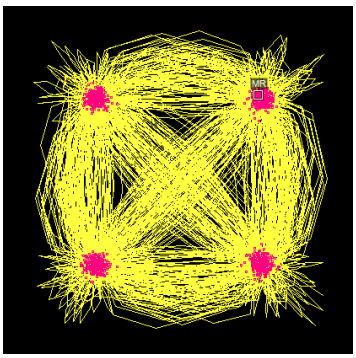

(f) 80 mA, with adaptive biasing. SNR = 23.2 dB, EVM = 6.8%.

Figure 5.20: QPSK receive constellations for the single tone test biased at 10, 40, and 80 mA, with and without adaptive biasing.

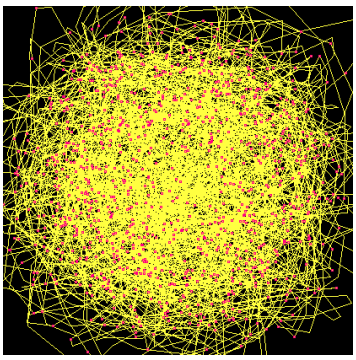

(a) 10 mA, no adaptive biasing.
SNR = 4.33 dB, EVM = 53.5%.

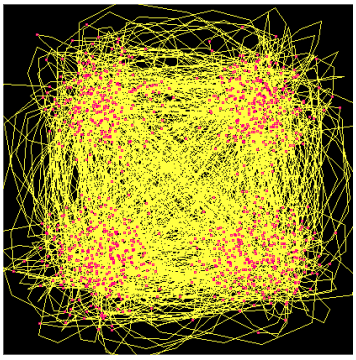

(b) 10 mA, with adaptive biasing.
SNR = 8.2 dB, EVM = 33.1%.

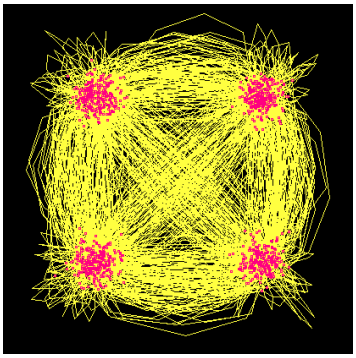

(c) 40 mA, no adaptive biasing.
SNR = 16.8 dB, EVM = 13.5%.

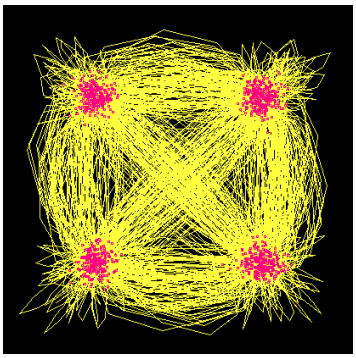

(d) 40 mA, with adaptive biasing.
SNR = 15 dB, EVM = 12.1%.

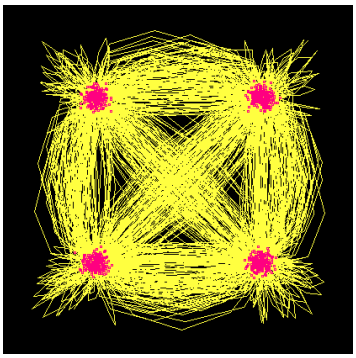

(e) 80 mA, no adaptive biasing.
SNR = 23.2 dB, EVM = 6.7%.

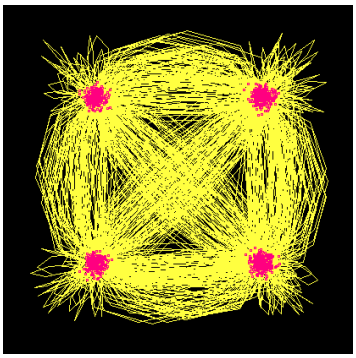

(f) 80 mA, with adaptive biasing.
SNR = 22.9 dB, EVM = 6.7%.

Figure 5.21: QPSK receive constellations for the wideband interference test biased at 10, 40, and 80 mA, with and without adaptive biasing.

6 Conclusion

This thesis demonstrates two passive circuit topologies that enable STAR over narrow bandwidths. In future communications and radar systems STAR technology will be an enabler for both increased functionality and higher data rates. Recent demonstrations of STAR for automotive radar have utilized techniques that dissipate 3 dB of Tx and Rx power in order to achieve STAR operation. However, for systems with higher power Tx signals this loss is undesirable. In order to address the power dissipation problem and increase the bandwidth for a single cancellation layer a new method for implementing a self-interference cancellation circuit was used.

From the basic principles of phase cancellation it was shown that such a circuit could be designed using directional couplers, and either a conventional delay-line or hairpin resonators. Simulated data from ANSYS Electronics Desktop was used to obtain the magnitude and phase characteristics of the antenna mutual coupling. Using this data the hypothesis that the antenna's mutual coupling phase could be more closely matched using a filter element was tested and verified. Both devices were fabricated and measured.

The measured results shown agree with simulation and allow for a direct comparison between the two methodologies for implementing STAR. Both fabricated devices achieve approximately the same result as obtained in simulation. The measured delay-line device has a -40 dB bandwidth of 4.2 MHz while the filter implementation has a -40 dB bandwidth of 11.2 MHz, an increase of 266.7%. The bandwidths over which 20 dB of cancellation is achieved are 5 MHz and 14 MHz for the delay-line and hairpin filer implementations, respectively. An analytic expression was derived that shows that this bandwidth is directly related to the phase and magnitude error between the mutual coupling response and the cancellation circuit. Using this metric, the hairpin resonator implementation is superior to the delay line.

In addition to the STAR devices developed for this work, the second portion of this thesis was dedicated to the analysis of a wideband, adaptive LNA. Due to the wideband frequency response of the LNA the effects of out-of-band interfering signals were tested. This was carried out by utilizing the LNA as part of a QPSK receiver. An additional out-of-band noise signal was injected and combined with the desired receive signal, resulting in degraded performance. This result clearly demonstrates the necessity of tunable or reconfigurable RF filters when systems are operating in locations with high spectrum utilization. The adaptive biasing current of the LNA is analyzed for dynamic power saving in a large array. This analysis provides a formula for calculating average power savings with this type of adaptive device. The analysis performed shows that for a range-gated system an average power savings of 59.4% can be achieved, when compared to a fixed bias LNA.

This thesis has demonstrated results contributing to the implementation of STAR circuits, microwave device theory, and the benefits of reconfigurable LNAs. To the author's best knowledge, this is the first demonstration of a passive STAR circuit using a resonating element. The theory presented on exponential T-junction power dividers also contributes a new design method for the device. The benefits of adaptive and reconfigurable LNA biasing were shown for a QPSK receiver system. Finally, these same features were shown to have a large benefit for receiver power savings in phased array radar systems. This thesis will contribute to the development of new self-interference cancellation circuits enabling same-frequency STAR and will impact the design of new transceivers using reconfigurable elements for dynamic power savings.

6.1 Future Work

This thesis presents the first step in the development of new self-interference cancellation circuits for same-frequency STAR. There are several directions additional work in this area can take. First, different resonator types should be investigated in order to improve the bandwidth of the mutual coupling phase matching. Second, a wider bandwidth antenna element should be characterized for the same purpose. The same methodology should then be applied to single resonance antennas using circulators. Finally, a method for tuning the cancellation frequency and bandwidth should be developed. After these steps have been completed antennas with multiple resonances must be characterized using the same procedure. Since these antennas, such as stacked patches, contain multiple resonances it is hypothesized that multi-pole filters can be used for phase matching.

In regard to the DARE, further testing in order to characterize the DARE for pulsed operation needs to be completed. First, using a CW signal as a receive tone, a pulsed interference source will be used. This test should be conducted with the adaptive biasing feature both enabled and disabled. By implementing a delay-line filter, subsequent pulses should be subtracted to determine the effect of the pulsed interference on clutter rejection and MTI processing for a radar system. Finally, the desired receive tone should be changed to a pulsed waveform and measured for the same effects.

References

[1] A. Sabharwal, P. Schniter, D. Guo, D. W. Bliss, S. Rangarajan, and R. Wichman, "In-band full-duplex wireless: Challenges and opportunities," *IEEE Journal on Selected Areas in Communications*, vol. 32, no. 9, pp. 1637–1652, Sep. 2014.

[2] M. Skolnik, *Introduction to Radar Systems, 3rd Edition*. McGraw-Hill, 2001.

[3] F. G. Stremler, *Introduction to Communication Systems*. Addison-Wesley, 1990.

[4] M. Rahnema, "Overview of the GSM system and protocol architecture," *IEEE Communications Magazine*, vol. 31, no. 4, pp. 92–100, Apr. 1993.

[5] 3GPP, "Radio transmission and reception," 3rd Generation Partnership Project (3GPP), TS 05.05, Nov. 2005. [Online]. Available: `http://www.3gpp.org/ftp/Specs/html-info/0505.htm`.

[6] P. E. Mogensen and J. Wigard, "On antenna and frequency diversity in gsm related systems (GSM-900, DCS-1800, and PCS1900)," in *Seventh IEEE International Symposium on Personal, Indoor and Mobile Radio Communications*, vol. 3, Oct. 1996, pp. 1272–1276.

[7] R. Lucero, W. Qutteneh, A. Pavio, D. Meyers, and J. Estes, "Design of an LTCC switch diplexer front-end module for GSM/DCS/PCS applications," in *2001 IEEE Radio Frequency Integrated Circuits Symposium Digest*, May 2001, pp. 213–216.

[8] A. Wegener, "Filter design methods applied to panelized antenna array integration for digital backends," PhD thesis, 2013, p. 138.

[9] T. Dinc and H. Krishnaswamy, "A T/R antenna pair with polarization-based reconfigurable wideband self-interference cancellation for simultaneous transmit and receive," in *2015 IEEE MTT-S International Microwave Symposium*, May 2015, pp. 1–4.

[10] K. L. Scherer, S. J. Watt, E. A. Alwan, A. A. Akhiyat, B. Dupaix, W. Khalil, and J. L. Volakis, "Simultaneous transmit and receive system architecture with four stages of cancellation," in *2015 IEEE International Symposium on Antennas and Propagation USNC/URSI National Radio Science Meeting*, Jul. 2015, pp. 520–521.

[11] M. A. Elmansouri, E. A. Etellisi, and D. S. Filipovic, "Ultra-wideband circularly-polarized simultaneous transmit and receive (STAR) antenna system," in *2015 IEEE International Symposium on Antennas and Propagation*, Jul. 2015, pp. 508–509.

[12] E. A. Etellisi, M. A. Elmansouri, and D. S. Filipovic, "Wideband monostatic simultaneous transmit and receive (star) antenna," *IEEE Transactions on Antennas and Propagation*, vol. 64, no. 1, pp. 6–15, Jan. 2016.

[13] E. G. Tianang and D. S. Filipovic, "A dipole antenna system for simultaneous transmit and receive," in *2015 IEEE International Symposium on Antennas and Propagation USNC/URSI National Radio Science Meeting*, Jul. 2015, pp. 428–429.

[14] A. T. Wegener and W. J. Chappell, "Coupled antenna scheme using filter design techniques and tunable resonators to show simultaneous transmit and receive," in *2013 IEEE MTT-S International Microwave Symposium Digest*, Jun. 2013, pp. 1–4.

[15] T. Snow, C. Fulton, and W. J. Chappell, "Multi-antenna near field cancellation duplexing for concurrent transmit and receive," in *2011 IEEE MTT-S International Microwave Symposium Digest*, Jun. 2011, pp. 1–4.

[16] ——, "Transmit receive duplexing using digital beamforming system to cancel self interference," *IEEE Transactions on Microwave Theory and Techniques*, vol. 59, no. 12, pp. 3494–3503, Dec. 2011.

[17] K. E. Kolodziej, P. T. Hurst, A. J. Fenn, and L. I. Parad, "Ring array antenna with optimized beamformer for simultaneous transmit and receive," in *IEEE Antennas and Propagation Society International Symposium*, Jul. 2012, pp. 1–2.

[18] D. Pozar, *Microwave Engineering, 4th Edition*. Wiley, 2011.

[19] S. Cheung, T. Halloran, W. Weedon, and C. Caldwell, "Active quasi-circulators using quadrature hybrids for simultaneous transmit and receive," in *IEEE MTT-S International Microwave Symposium*, Jun. 2009, pp. 381–384.

[20] S. K. Cheung, T. P. Halloran, W. H. Weedon, and C. P. Caldwell, "MMIC-based quadrature hybrid quasi-circulators for simultaneous transmit and receive," *IEEE Transactions on Microwave Theory and Techniques*, vol. 58, no. 3, pp. 489–497, Mar. 2010.

[21] S. K. Cheung, W. H. Weedon, and C. P. Caldwell, "High isolation lange-ferrite circulators with NF suppression for simultaneous transmit and receive," in *2010 IEEE MTT-S International Microwave Symposium Digest*, May 2010, pp. 1352–1355.

[22] C. H. Cox and E. I. Ackerman, "Photonics for simultaneous transmit and receive," in *2011 IEEE MTT-S International Microwave Symposium Digest*, Jun. 2011, pp. 1–4.

[23] J. Kim, S. Ko, S. Jeon, J. Park, and S. Hong, "Balanced topology to cancel Tx leakage in CW radar," *IEEE Microwave and Wireless Components Letters*, vol. 14, no. 9, pp. 443–445, Sep. 2004.

[24] C. Y. Kim, J. G. Kim, J. H. Oum, J. R. Yang, D. K. Kim, J. H. Choi, S. W. Kwon, S. H. Jeon, J. W. Park, and S. Hong, "Tx leakage cancellers for 24 GHz and 77 GHz vehicular radar applications," in *IEEE MTT-S International Microwave Symposium*, Jun. 2006, pp. 1402–1405.

[25] C. Y. Kim, J. G. Kim, and S. Hong, "A quadrature radar topology with Tx leakage canceller for 24-GHz radar applications," *IEEE Transactions on Microwave Theory and Techniques*, vol. 55, no. 7, pp. 1438–1444, Jul. 2007.

[26] K. Lin, Y. E. Wang, C. K. Pao, and Y. C. Shih, "A Ka-band FMCW radar front-end with adaptive leakage cancellation," *IEEE Transactions on Microwave Theory and Techniques*, vol. 54, no. 12, pp. 4041–4048, Dec. 2006.

[27] P. D. L. Beasley, A. G. Stove, B. J. Reits, and B. As, "Solving the problems of a single antenna frequency modulated CW radar," in *IEEE 1990 International Radar Conference*, May 1990, pp. 391–395.

[28] A. G. Stove, "Linear FMCW radar techniques," *IEEE Proceedings on Radar and Signal Processing*, vol. 139, no. 5, pp. 343–350, Oct. 1992.

[29] Q. Jiming, Q. Xinjian, and R. Zhijiu, "Development of a 3 cm band reflected power canceller," in *Proc. 2001 CIE International Conference on Radar*, 2001, pp. 1098–1102.

[30] J. W. Jung, H. H. Roh, J. C. Kim, H. G. Kwak, M. S. Jeong, and J. S. Park, "TX leakage cancellation via a micro controller and high TX-to-RX isolations covering an UHF RFID frequency band of 908 to 914 MHz," *IEEE Microwave and Wireless Components Letters*, vol. 18, no. 10, pp. 710–712, Oct. 2008.

[31] A. Raghavan, E. Gebara, E. M. Tentzeris, and J. Laskar, "Analysis and design of an interference canceller for collocated radios," *IEEE Transactions on Microwave Theory and Techniques*, vol. 53, no. 11, pp. 3498–3508, Nov. 2005.

[32] M. Jain, J. I. Choi, T. Kim, D. Bharadia, S. Seth, K. Srinivasan, P. Levis, S. Katti, and P. Sinha, "Practical, real-time, full duplex wireless," in *Proc. 17th Annual International Conference on Mobile computing and Networking*, 2011, pp. 301–312.

[33] J. G. McMichael and K. E. Kolodziej, "Optimal tuning of analog self interference cancellers for full-duplex wireless communication," in *2012 50th Annual Allerton Conference on Communication, Control, and Computing*, Oct. 2012, pp. 246–251.

[34] K. E. Kolodziej, J. G. McMichael, and B. T. Perry, "Adaptive RF canceller for transmit receive isolation improvement," in *2014 IEEE Radio and Wireless Symposium*, Jan. 2014, pp. 172–174.

[35] R. Malmqvist, A. Gustafsson, T. Nilsson, C. Samuelsson, B. Carlegrim, I. Ferrer, T. Vaha-Heikkila, A. Ouacha, and R. Erickson, "RF MEMS and GaAs based reconfigurable RF front-end components for wide-band multi-functional phased arrays," in *3rd European Radar Conference*, Sep. 2006, pp. 319–322.

[36] R. Malmqvist, A. Ouacha, and R. Erickson, "Multi-band and reconfigurable front-ends for flexible and multi-functional RF systems," in *2007 Asia-Pacific Microwave Conference*, Dec. 2007, pp. 1–4.

[37] C. K. Chu, H. K. Huang, H. Z. Liu, C. H. Lin, C. H. Chang, C. L. Wu, C. S. Chang, and Y. H. Wang, "An X-band high-power and high-PAE PHEMT MMIC power amplifier for pulse and CW operation," *IEEE Microwave and Wireless Components Letters*, vol. 18, no. 10, pp. 707–709, Oct. 2008.

[38] J. Staudinger, R. Hooper, M. Miller, and Y. Wei, "Wide bandwidth GSM / WCDMA / LTE base station LNA with ultra-low sub 0.5 dB noise figure," in *2012 IEEE Radio and Wireless Symposium*, Jan. 2012, pp. 223–226.

[39] M. R. B. Dunsmore and J. Clarke, "High power tunable YIG filters," in *11th European Microwave Conference*, Sep. 1981, pp. 405–411.

[40] R. R. Mansour, M. Bakri-Kassem, M. Daneshmand, and N. Messiha, "RF MEMS devices," in *Proc. 2003 International Conference on MEMS, NANO and Smart Systems*, Jul. 2003, pp. 103–107.

[41] Y. J. Chan, C. F. Huang, C. C. Wu, C. H. Chen, and C. P. Chao, "Performance consideration of MOS and junction diodes for varactor application," *IEEE Transactions on Electron Devices*, vol. 54, no. 9, pp. 2570–2573, Sep. 2007.

[42] L. Lolis, M. de Souza, L. B. Zambon, and A. Mariano, "Impact of a fully reconfigurable LNA on an RF front-end: A system level analysis," in *2014 21st IEEE International Conference on Electronics, Circuits and Systems*, Dec. 2014, pp. 662–665.

[43] A. Bevilacqua, C. Sandner, A. Gerosa, and A. Neviani, "A fully integrated differential CMOS LNA for 3-5 GHz ultrawideband wireless receivers," *IEEE Microwave and Wireless Components Letters*, vol. 16, no. 3, pp. 134–136, Mar. 2006.

[44] H. G. Dehrizi and J. Haddadnia, "A great ultra wideband 3.1-10.6 GHz LNA in 0.18-um CMOS for UWB pulse-radio systems applications," in *2012 9th International Multi-Conference on Systems, Signals and Devices*, Mar. 2012, pp. 1–4.

[45] M. Khurram and S. M. R. Hasan, "A 3-5 GHz current-reuse gm boosted CG LNA for ultrawideband in 130 nm CMOS," *IEEE Transactions on Very Large Scale Integration Systems*, vol. 20, no. 3, pp. 400–409, Mar. 2012.

[46] D. C. Howard, J. Poh, T. S. Mukerjee, and J. D. Cressler, "A 3–20 GHz SiGe HBT ultra-wideband LNA with gain and return loss control for multiband wireless applications," in *2010 53rd IEEE International Midwest Symposium on Circuits and Systems*, Aug. 2010, pp. 445–448.

[47] M. Micovic, A. Kurdoghlian, T. Lee, R. O. Hiramoto, P. Hashimoto, A. Schmitz, I. Milosavljevic, P. J. Willadsen, W. S. Wong, M. Antcliffe, M. Wetzel, M. Hu, M. J. Delaney, and D. H. Chow, "Robust broadband (4 GHz - 16 GHz) GaN MMIC LNA," in *2007 IEEE Compound Semiconductor Integrated Circuits Symposium*, Oct. 2007, pp. 1–4.

[48] U. Kim, S. Kang, J. Woo, Y. Kwon, and J. Kim, "A multiband reconfigurable power amplifier for UMTS handset applications," *IEEE Transactions on Microwave Theory and Techniques*, vol. 60, no. 8, pp. 2532–2542, Aug. 2012.

[49] J. H. Chen, S. R. Helmi, A. Y. S. Jou, and S. Mohammadi, "A wideband power amplifier in 45 nm CMOS SOI technology for X-band applications," *IEEE Microwave and Wireless Components Letters*, vol. 23, no. 11, pp. 587–589, Nov. 2013.

[50] X. Ding, S. He, F. You, S. Xie, and Z. Hu, "2-4 GHz wideband power amplifier with ultra-flat gain and high PAE," *Electronics Letters*, vol. 49, no. 5, pp. 326–327, Feb. 2013.

[51] C. Berrached, D. Bouw, M. Camiade, and D. Barataud, "Wideband high efficiency high power GaN amplifiers using MIC and quasi-MMIC technologies," in *2013 European Microwave Conference*, Oct. 2013, pp. 1395–1398.

[52] S. Cripps, *RF Power Amplifiers for Wireless Communications, 2nd Edition*. Artech House, 2006.

[53] A. Tuffery, N. Deltimple, E. Kerhervé, V. Knopik, and P. Cathelin, "CMOS fully integrated reconfigurable power amplifier with efficiency enhancement for LTE applications," *Electronics Letters*, vol. 51, no. 2, pp. 181–183, 2015.

[54] M. Tsuru, K. Kawakami, K. Tajima, K. Miyamoto, M. Nakane, K. Itoh, M. Miyazaki, and Y. Isota, "A triple-tuned ultra-wideband VCO," *IEEE Transactions on Microwave Theory and Techniques*, vol. 56, no. 2, pp. 346–354, Feb. 2008.

[55] C. H. Tseng and C. L. Chang, "Design of low phase-noise microwave oscillator and wideband VCO based on microstrip combline bandpass filters," *IEEE Transactions on Microwave Theory and Techniques*, vol. 60, no. 10, pp. 3151–3160, Oct. 2012.

[56] P. Z. Rao, T. Y. Chang, C. P. Liang, and S. J. Chung, "An ultra-wideband high-linearity CMOS mixer with new wideband active baluns," *IEEE Transactions on Microwave Theory and Techniques*, vol. 57, no. 9, pp. 2184–2192, Sep. 2009.

[57] S. K. Hampel, O. Schmitz, M. Tiebout, and I. Rolfes, "Inductorless low-voltage and low-power wideband mixer for multistandard receivers," *IEEE Transactions on Microwave Theory and Techniques*, vol. 58, no. 5, pp. 1384–1390, May 2010.

[58] J. S. Hong and M. J. Lancaster, *Microstrip Filters for RF/Microwave Applications*. John Wiley & Sons, 2004.

[59] J. Hong, "Reconfigurable planar filters," *IEEE Microwave Magazine*, vol. 10, no. 6, pp. 73–83, Oct. 2009.

[60] P. Blondy, C. Palego, M. Houssini, A. Pothier, and A. Crunteanu, "RF-MEMS reconfigurable filters on low loss substrates for flexible front ends," in *2007 Asia-Pacific Microwave Conference*, Dec. 2007, pp. 1–3.

[61] S. Saeedi, J. Lee, and H. H. Sigmarsson, "Tunable, high-Q, substrate integrated, evanescent-mode cavity bandpass-bandstop filter cascade," *IEEE Microwave and Wireless Components Letters*, vol. 26, no. 4, pp. 240–242, Apr. 2016.

[62] S. Saeedi, S. Atash-bahar, and H. H. Sigmarsson, "Active tunable substrate integrated evanescent-mode cavity resonator using negative resistance," in *2016 IEEE Radio and Wireless Symposium*, Jan. 2016, pp. 87–90.

[63] Y. Murakami, T. Ohgihara, and T. Okamoto, "A 0.5-4.0-GHz tunable bandpass filter using YIG film grown by LPE," *IEEE Transactions on Microwave Theory and Techniques*, vol. 35, no. 12, pp. 1192–1198, Dec. 1987.

[64] G. M. Yang, J. Wu, J. Lou, M. Liu, and N. X. Sun, "Low-loss magnetically tunable bandpass filters with YIG films," *IEEE Transactions on Magnetics*, vol. 49, no. 9, pp. 5063–5068, Sep. 2013.

[65] Z. Zhang, H. Lv, Z. Feng, and Y. Nie, "Study on the magnetically tunable filters based on Mnn and Al3 co-doped YIG ferrite," *IEEE Transactions on Magnetics*, vol. 51, no. 11, pp. 1–4, Nov. 2015.

[66] C. R. White and G. M. Rebeiz, "Single- and dual-polarized tunable slot-ring antennas," *IEEE Transactions on Antennas and Propagation*, vol. 57, no. 1, pp. 19–26, Jan. 2009.

[67] G. M. Yang, X. Xing, A. Daigle, M. Liu, O. Obi, S. Stoute, K. Naishadham, and N. X. Sun, "Tunable miniaturized patch antennas with self-biased multilayer magnetic films," *IEEE Transactions on Antennas and Propagation*, vol. 57, no. 7, pp. 2190–2193, Jul. 2009.

[68] Y. Yusuf and N. Behdad, "Miniaturization of a class of ultra-wideband antennas using dual-mode radiating structures," in *2012 IEEE International Conference on Wireless Information Technology and Systems*, Nov. 2012, pp. 1–4.

[69] W. Lin, H. Wong, and J. Xiang, "Emerging reconfigurable antenna elements for broadband wireless communication systems," in *TENCON 2015 IEEE Region 10 Conference*, Nov. 2015, pp. 1–6.

[70] A. Khidre, F. Yang, and A. Z. Elsherbeni, "Reconfigurable microstrip antenna with tunable radiation beamwidth," in *IEEE Antennas and Propagation Society International Symposium*, Jul. 2013, pp. 1444–1445.

[71] P. S. Hall, P. Gardner, J. Kelly, E. Ebrahimi, M. R. Hamid, F. Ghanem, F. J. Herraiz-Martinez, and D. Segovia-Vargas, "Reconfigurable antenna challenges for future radio systems," in *2009 3rd European Conference on Antennas and Propagation*, Mar. 2009, pp. 949–955.

[72] Y. J. Guo and P. Y. Qin, "Advances in reconfigurable antennas for wireless communications," in *2015 9th European Conference on Antennas and Propagation*, May 2015, pp. 1–4.

[73] J. E. Ruyle, C. Jung, and J. T. Bernhard, "Reconfigurable stacked patch antenna with beamsteering capabilities," in *2008 IEEE Antennas and Propagation Society International Symposium*, Jul. 2008, pp. 1–4.

[74] A. S. Al-Zayed, M. A. Kourah, and S. F. Mahmoud, "Frequency-reconfigurable single- and dual-band designs of a multi-mode microstrip antenna," *IET Microwaves, Antennas & Propagation*, vol. 8, no. 13, pp. 1105–1112, Oct. 2014.

[75] E. G. Farr, "Recent topics in ultra-wideband antennas," in *2012 IEEE International Conference on Ultra-Wideband*, Sep. 2012, pp. 222–226.

[76] Z. Chen, M. Ammann, X. Qing, X. Wu, T. See, and A. Cai, "Planar antennas," *IEEE Microwave Magazine*, vol. 7, no. 6, pp. 63–73, Dec. 2006.

[77] J. W. Brown, R. V. Churchill, and M. Lapidus, *Complex Variables and Applications*. McGraw-Hill New York, 1996, vol. 7.

[78] J. Nillson and S. Riedel, *Electric Circuits, 9th Edition*. Prentice Hall, 2011.

[79] C. Balanis, *Antenna Theory: Analysis and Design, 3rd Edition*. John Wiley & Sons, 2005.

[80] Y. Lo, D. Solomon, and W. Richards, "Theory and experiment on microstrip antennas," *IEEE Transactions on Antennas and Propagation*, vol. 27, no. 2, pp. 137–145, Mar. 1979.

[81] S. Akhtarzad, T. R. Rowbotham, and P. B. Johns, "The design of coupled microstrip lines," *IEEE Transactions on Microwave Theory and Techniques*, vol. 23, no. 6, pp. 486–492, Jun. 1975.

[82] J. Muller, M. N. Pham, and A. F. Jacob, "Directional coupler compensation with optimally positioned capacitances," *IEEE Transactions on Microwave Theory and Techniques*, vol. 59, no. 11, pp. 2824–2832, Nov. 2011.

[83] S. L. March, "Phase velocity compensation in parallel-coupled microstrip," in *1982 IEEE MTT-S International Microwave Symposium Digest*, Jun. 1982, pp. 410–412.

[84] A. Podell, "A high directivity microstrip coupler technique," in *G-MTT 1970 International Microwave Symposium*, May 1970, pp. 33–36.

[85] E. G. Cristal and S. Frankel, "Hairpin-line and hybrid hairpin-line/half-wave parallel-coupled-line filters," *IEEE Transactions on Microwave Theory and Techniques*, vol. 20, no. 11, pp. 719–728, Nov. 1972.

[86] D. G. Swanson, "Narrow-band microwave filter design," *IEEE Microwave Magazine*, vol. 8, no. 5, pp. 105–114, Oct. 2007.

[87] S. D. Targonski, R. B. Waterhouse, and D. M. Pozar, "Design of wide-band aperture-stacked patch microstrip antennas," *IEEE Transactions on Antennas and Propagation*, vol. 46, no. 9, pp. 1245–1251, Sep. 1998.

[88] C. J. R. Smith and H. H. Sigmarsson, "Dual-band second order microstrip filter using dual-mode perturbed meander loop resonators," in *2015 IEEE 16th Annual Wireless and Microwave Technology Conference*, Apr. 2015, pp. 1–3.

[89] B. P. Kumar and G. R. Branner, "Application of empirical models to design microstrip tee junctions with prespecified power-divider ratios," in *Proc. 40th Midwest Symposium on Circuits and Systems*, vol. 1, Aug. 1997, pp. 577–580.

[90] S. C. Wu, H. Y. Yang, N. G. Alexopoulos, and I. Wolff, "A rigorous dispersive characterization of microstrip cross and T junctions," *IEEE Transactions on Microwave Theory and Techniques*, vol. 38, no. 12, pp. 1837–1844, Dec. 1990.

[91] W. Menzel, "Design of microstrip power dividers with simple geometry," *Electronics Letters*, vol. 12, no. 24, pp. 639–641, Nov. 1976.

[92] J. Gong and Q. Chu, "Equivalent-circuit model of suspended microstrip T-junction," in *2005 Asia-Pacific Microwave Conference Proceedings*, vol. 5, Dec. 2005, 3 pp.

[93] W. Menzel, "Calculation of the S-parameters of an unsymmetric microstrip T-junction (computer program descriptions)," *IEEE Transactions on Microwave Theory and Techniques*, vol. 26, no. 3, pp. 217–217, Mar. 1978.

[94] J. Hong, B. Wang, S. Lai, and B. Zeng, "Neural network model with broadband prior knowledge neurons for microstrip T-junction structure," in *IEEE Antennas and Propagation Society International Symposium*, Jul. 2006, pp. 1453–1456.

[95] M. J. Ahmed, "Impedance transformation equations for exponential, cosine-sqaared, and parabolic tapered transmission lines," *IEEE Transactions on Microwave Theory and Techniques*, vol. 29, no. 1, pp. 67–68, Jan. 1981.

[96] R. Wyse and J. Lovseth, "A digitally-reconfigurable 10 GHz bandwidth receiver with dynamically adapting capability," in *GOMAC 2013*, Mar. 2013, pp. 1–3.

[97] I. Piekarz, J. Sorocki, I. Slomian, K. Wincza, and S. Gruszczynski, "Compact single-layer microstrip Marchand type balun," in *2015 IEEE 16th Annual Wireless and Microwave Technology Conference*, Apr. 2015, pp. 1–4.